
Low-Dimensional Architectures of Some Liquid-Crystalline Amphiphilic Molecules on HOPG

By

Loji K Thomas

in partial fulfillment of the requirements for the degree of
Doctor der Naturwissenschaften (Dr. rer. nat)

Submitted to

Department of Physics

University of Osnabrück
Germany



April 2011

First referee	Prof. Dr. Michael Reichling
Second referee	Prof. Dr. Uwe Beginn
Third referee	Prof. Dr. Philipp Maass
Fourth referee	Dr. Johann P. Klare

This PhD work has been carried out under the supervision of Michael Reichling, NanoScience Centre, Universität Osnabrück from March 2007 to April 2011.

Submitted on 11.04.2011

... and the last sentence of the book of Dirac I can still remember 'It seems that some essentially new physical ideas are here needed ''

-Richard Feynman quoting Paul Dirac in his Nobel lecture

Abstract

The development of nanotechnology using organic materials is one of the most exciting and challenging stories of our times. Materials with layered and fiber architectures at interfaces have an important role in technology as well as in fundamental research. Despite their ubiquitous examples, the physics and chemistry of such one- and two-dimensional systems remain rather difficult to fathom. This thesis is an attempt to elucidate the subtle details of self-assembled 1-D and 2-D organic nanostructures formed on highly oriented pyrolytic graphite (HOPG). Emphasis is given not just on studying the general trends of molecular ensembles on HOPG but also on their structural details down to atomic/sub-molecular level. Using scanning tunneling microscopy (STM) operated in air/liquids and contact-atomic force microscopy (AFM), two different classes of amphiphilic systems have been investigated - both bestowed with hydrogen bonding moieties (carboxyl and amide functionalities) and alkyl chains to aid supramolecular self-assembly on HOPG. The amide and carboxylic head groups can efficiently stabilize the self-assembled nanostructures through intra- and inter-molecular hydrogen bonds. The alkyl chains with their epitaxial match with the C-C bonds of graphite are known to enhance adsorption on HOPG as well as promote self-assembly through inter-chain van der Waals interactions.

In the first part, an attempt has been made to understand self-assembled physisorbed systems in general using a simple prototype- a monolayer of a long chain fatty acid on HOPG. The second and central part of the thesis deals with one-dimensional fibrous structures formed from a class of low molecular weight wedge-shaped liquid-crystalline amphiphilic derivatives of benzamide. These are a novel class of gel-based materials designed and synthesized by the work-group of Prof. Uwe Beginn, Institut für Chemie, Universität Osnabrück. Although STM has been widely used to study the morphology of planar adsorbate structures, its use in elucidating sub-molecular details of isolated 1-D organic entities has not shown the same level of efficacy owing to experimental difficulties. This thesis is one of the first attempts towards revealing the architectures and finer details at the atomic level of such single/isolated organic strands.

For the class of surface supported amphiphilic low-dimensional structures (chapter 4) dealing with the monolayer structure of a fatty acid, a precise determination of the O-O distance of the carboxylic dimer on HOPG is found from a moiré pattern analysis. Apart from this, monolayer characteristics such as chirality, molecular domains, moiré pattern and relative orientation of the molecules have been carefully probed. The discussion also involves a detailed account of the various interactions at play relevant to this molecule-graphite system.

The second class of self-assembled amphiphilic system is one-dimensional fibrous structures formed on HOPG from basically liquid-crystalline amphiphilic molecules. These

molecular fibers, for example, are promising candidates as charge transport channels in nanoelectronic devices as well as other 'lab on a chip' applications. One of the prerequisite for electronic and optoelectronic devices is the mobility of charge carriers. Organic molecules as components offer the advantage of increasing such mobilities by establishing supramolecular order within the charge transport channels. Wedge shaped amphiphilic molecules in general have a tendency to form a columnar mesophase in solution or melt phases. The primary interest is in understanding the true architecture of these fibers and how inter-molecular interactions and the geometry of the molecules affect the morphology of molecular aggregates on HOPG. Therefore, the molecules are modified in a systematic manner with regard to their functional groups, number and length of alkyl chains. This strategy gives valuable insight into the fiber structure and the crucial role played by weak non-covalent interactions such as hydrogen bonding, π - π interactions, CH- π forces and alkyl chain interdigitation in the self-assembly and supramolecular organization. Due to the presence of amide moieties in the molecules, hydrophobic HOPG is used as a substrate to avoid perturbative effects from the solid surface. However, the presence of alkyl chains can influence the fiber geometry on HOPG and structures distinctly different from the speculated models in their solution or gel state may be possible. Other factors such as the role of secondary hydrogen bonding, in maintaining order along the column axis are also of interest. These are some of the issues addressed in this thesis and are described in chapter 6.

A third issue that needs to be addressed is inherently connected with the low-dimensional structures on bare HOPG surface that mimic the adsorbate species (chapter 5). This is an often neglected part in the studies of fibrous adsorbates on HOPG despite the astonishing resemblance they show with those of the adsorbate structures. Both the fibrous and planar structures seen on the surface of a layered material like graphite originate from the weak van der Waals interaction between the graphene layers. The two-dimensional graphene sheet can be distorted in the third dimension with relatively low energy without changing the in-plane bond lengths. Therefore some methods to distinguish adsorbates from innate low-dimensional graphitic structures become inevitable.

Contents

Abstract	i
Contents	iii
List of Abbreviations	v
1. Introduction	1
2. Experimental Techniques	4
2.1. Scanning Tunneling Microscopy	4
2.1.1. STM Theory.....	6
2.1.2. STM Imaging of Surfaces and Adsorbates.....	8
2.2. Atomic Force Microscope.....	11
3. Materials	12
3.1. Substrate	12
3.2. Solvent, Molecules and Sample Preparation	14
3.3. Interactions in Supramolecular Systems	15
3.4. Physisorption Theory.....	18
3.5. Thermodynamics of Adsorption	21
3.6. Fourier Transform and Image Processing	22
3.7. Prelude to Soft Matter and Supramolecular Chemistry	24
3.8. Other Resources	28
4. Monolayer structure of Arachidic acid on HOPG	29
4.1. Introduction.....	29
4.2. Arachidic Acid on HOPG.....	30
4.3. Fast Fourier Transform Analysis	33
4.4. Pro-chirality of Arachidic Acid Monolayer	34
4.5. Energetics at Arachidic Acid-HOPG Interface.....	35
4.6. Monolayer Structure of Arachidic Acid on HOPG	38
4.6. 1. Determination of Intermolecular Distance from Moiré Pattern.....	38
4.6. 2. Disposition of Molecules and Plausible Models.....	38
4.7. Conclusion.....	39
5. Differentiating Low-Dimensional Organic Structures from Innate Graphene Manifolds	41
5.1. HOPG as a Substrate for STM Studies	41
5.2. Innate Graphite Low-Dimensional Structures	42
5.2.1. Planar (2-D) Graphite Structures.....	43
5.2.2. Fibrous (1-D) Graphite Structures.....	48
5.3. Differentiating Adsorbates from Innate Graphene Manifold.....	52
5.3.1. Differentiating Adsorbate Layers from Graphite Planar Structures.....	52
5.3.2. Differentiating Adsorbate Fibers from Fibrous Graphene Structures ..	53

5.4. Mechanism of Innate HOPG Fiber Formation.....	61
5.5. Conclusion	63
6. Liquid-crystalline Amphiphilic Molecules on HOPG	64
6.1. Motivation.....	64
6.2. Objective.....	65
6.3. Substrate, Solvent and Experimental Conditions	67
6.4. (Alkoxy)benzamides	69
6.4.1. 3,4,5-Tris(decyloxy)benzamide (3CB-8).....	69
6.4.2. 3,4,5-Tris(decyloxy)benzamide (3CB-10).....	81
6.4.3. Compare 3CB-8 and 3CB-10 Structures.....	84
6.4.4. Model for 3CB-n Fibers.....	85
6.5. (Alkoxy)benzoylhydrazines	90
6.5.1. 3,4,5-Tris(dodecyloxy)benzoylhydrazine (3CH-12).....	90
6.5.2. 4-(decyloxy)benzoylhydrazine (1CH-10)	96
6.5.3. 3,4-bis(decyloxy)benzoylhydrazine (2CH-10)	98
6.5.4. N,N'-Bis[3,4-bis(decyloxy)benzoyl]hydrazide (2CB'-10).....	99
7. Conclusion	102
Bibliography	105
Acknowledgements	117
Erklärung	118

List of Abbreviations

AFM	Atomic Force Microscopy
CNT	Carbon Nano Tube
ESP	Electrostatic potential
FFT	Fast Fourier Transform
HOMO	Highest Occupied Molecular Orbital
HOPG	Highly Oriented Pyrolytic Graphite
LC	Liquid Crystal/crystalline
LDOS	Local Density of States
LMW	Low Molecular Weight
LUMO	Lowest Unoccupied Molecular Orbital
ML	Monolayer
OM	Optical Microscopy
SA	Self Assembly
SAM	Self-assembled Monolayer
STM	Scanning Tunneling Microscope
TCB	1,2,4-Tri Chloro Benzene
2CH	Two-chain Hydrazine
3CB	Three-chain Benzamide

Chapter 1

Introduction

The long-term goal of nanotechnology is to design materials with specific properties by controlling processes at the ultimate limit of molecules. Organic molecules can form the functional basis for numerous existing and envisaged nanotechnology applications such as molecular light emitting/light harvesting devices, molecular electronics and nano-mechanical biosensors. The use of small organic molecules shows an inherent advantage over small inorganic clusters in the nanometer regime as they show discrete quantum energy levels. Inorganic clusters made by self-assembly (SA) or lithography will differ slightly in the number of atoms they consist of, and this scatter will be reflected in their quantum energy levels. Organic molecules of a given compound are absolutely identical and therefore nanoelectronic functions based on a given type of molecule shows exactly the same characteristics.

For practical applications, inexpensive high quality organic films need to be deposited on solid substrates. The properties of organic electronic materials in the solid-state are determined not only by those of individual molecules but also by their ensembles. Therefore the control of lateral assembly and spatial arrangement of nanostructures at interfaces is a prerequisite for potential applications. Supramolecular self-assembly have often been considered as the key to future nanoscale engineering via the 'bottom-up' approach [1]. The functional building units of nanoscale systems involve clusters (0-D), wires/tubes (1-D), sheets (2-D) and colloids/complex shapes (3-D). They are assembled from organic molecules using their self-assembling ability and their flexibility for fine-tuning the structural, chiral, electronic and chemical properties, and the many functions they can perform [2-4].

Supramolecular chemistry, is a very different axis directed to the notion that chemists could control non-covalent bonds in all structures with the same precision achieved by synthetic chemistry [5]. The self-assembling ability of organic molecules plays a crucial role in supramolecular organization. Self-assembly is a natural and spontaneous process resulting in some order from disordered components occurring mainly through non-covalent interactions such as van der Waals, hydrogen bonding, hydrophilic/hydrophobic, π - π , electrostatic and metal-ligand coordination bonding. Self-assembly is ubiquitous in nature; for instance, while reading these pages, you are actually using the self assembled

membranes that encapsulate the cells in your brain and eyes. Self-assembly, despite its seemingly simple nature, is difficult to define mathematically.

Self-assembly on surfaces is one of the major practical routes towards molecular structure formation [6-8] and used for the realization of electronic and opto-electronic devices [9-11]. The supramolecular structures formed on solid surfaces are a result of delicate balance between competing molecule-surface and molecule-molecule interactions. The interest in the area of organic adsorbates self-assembled on solid surfaces is motivated not only by the possibility of building molecular nanostructures but also for the fundamental understanding of processes such as self-assembly and molecular recognition down to the single-molecule level. As devices based on single molecules are still challenging, systems involving molecular thin films or ensembles of molecules appear to be most promising for the near future [12, 13]. Molecular electronics is concerned with using single molecules as building blocks for molecular wires, molecular switches or molecular diodes for the purpose of signal processing. Apart from functionalized thin films, suitable inter-connects are vital for the realization of 'bottom-up' device fabrication.

Self-assembly of small organic molecules and/or ions into different nanostructures such as fibers, rods, tubes, spheres and thin films offer a promising path towards fabricating novel materials with desired physical and chemical properties via the control of their composition, size and shape. Self-assembly is a spontaneous process but the production of desired structures can be deliberately achieved by proper designing of the basic building units at the molecular level.

Nanoscience emerged mostly from physics and material science with the notion that physical properties at the nanoscale would undergo unique transitions. Advances in microscopy make it easier to see objects at nanoscales and advances in chemical synthesis to construct molecular systems more easily than ever before. The study of nanoscale architectures is a fundamental part of nanotechnology, as both materials and their applications will depend on the new structures which chemists can generate. The visualization of molecular structures in real space at the atomic scale is most helpful for the understanding of the self-assembly process and the liquid-solid interface is an excellent environment to probe them [14-18]. The main experimental technique used is STM operated in the ambient/solution environment.

In general, all molecules examined in the thesis are of amphiphilic nature but vary in their structural as well as functional aspects. In the first part of the thesis, the focus falls on a 2-D self-assembled system on highly oriented pyrolytic graphite (HOPG) namely arachidic acid monolayer. In order to understand the influence of long alkyl chains and hydrogen bonding moieties in the adsorption and SA of organic molecules on HOPG, this system acts as a simple prototype model.

The major theme of this thesis is about the fibrous structures formed from some liquid-crystalline, wedge shaped amphiphilic molecules. Given the one-dimensional fibrillar nature of gel-phase materials, attention has begun to focus on the ability of self-assembled gels to facilitate energy transfer processes [19]. Although much has been revealed about the columnar mesophases in solution, the low-dimensional architectures of such fibers remain to be elucidated in their true detail. Some of the gel-based molecules studied here are known to form hexagonal/rectangular disordered mesophases in solution such as 3,4,5,-Tris(alkoxy)benzamidates-n (3CB-n); 'n' stands for the number of methylene units in the alkyl chains. The molecules are designed in a systematic manner to study the influence of molecular geometry and inter-molecular interactions in column formation. This leads to molecules with different geometries such as 3,4,5,-Tris(alkoxy)benzoylhydrazine (3CH-12), 4-Alkoxybenzoylhydrazine (1CH-10), 3,4-Bis(alkoxy)benzoylhydrazine (2CH-10) and N,N'-Bis[3,4-bis(alkoxy)benzoyl]hydrazide (2CB'-10). Molecular mechanics simulation using *Macromodel 8.0* has been done in some cases to understand the graphite-molecule interactions. Graphite with its very weak inter-lamellar binding can form various structures by itself [20-24] and bare HOPG(0001) surface manifolds can mimic adsorbate structures. In order to unambiguously establish the capability of the molecules to form fibrous structures, they are deposited also on a gold(111) surface and, AFM and optical microscopy has been used to obtain their large scale morphology.

Chapter 2

Experimental Methods

2.1. Scanning Tunneling Microscopy

The scanning tunneling microscope (STM) invented in 1981 by Gerd Binnig and Heinrich Rohrer [25-28] has revolutionized the field of surface science by opening up a whole new class of investigations that were previously limited to the reciprocal space. Out of all scanning probe methods, STM possess the highest spatial resolution with a lateral and vertical resolution of ~ 0.1 nm and 0.01 nm respectively. STM can be used not only to probe conducting and semiconducting surfaces at the atomic scale, but in its versatility, extends to the realm of manipulating individual atoms and molecules on surfaces as well as other applications [29-33]. It can also be used to image generally non-conducting organic molecules when deposited on a conducting substrate. STM has the capability not only to investigate the atom-by-atom geometry but in some cases, also the electronic structure of surfaces. Apart from vacuum, it can also be operated in air or in solution. Although, conducting organic molecular crystals can be imaged directly by STM without the need for a substrate surface [34], organic molecules, in general being insulators, can be imaged with a scanning tunneling microscope only when deposited on a conducting substrate like graphite.

The scanning tunneling microscope relies on localized electron tunneling between a sharp tip of single atom termination and a conducting sample. When the tip is brought within about 1 nm of the sample, even though an energy barrier exists, quantum mechanics predicts a finite probability for electron tunneling. With an applied voltage between the sample and the tip, a net current can be obtained with the direction of the current depending on the polarity of the bias. The amount of current depends on different parameters such as the applied voltage, material of the tip and surface and the tip shape. But in general the current has an inverse exponential dependence on the tunnel gap. There are two basic modes in which the STM can operate: constant current (CI) and constant height (CH). In both cases, the image is a mixture of both electronic and geometric information. The CI mode yields higher resolution but at the expense of lower scan speeds. It involves a fast feedback and therefore can respond to any perturbation on the surface. In CH mode, a faster scan rate and slower feedback is used. Here the average separation of the tip and sample is kept constant and the tip does not follow every contour of the surface only the general slope of the surface. The tunneling current changes as a

result of every contour and therefore this information can be used to represent the surface topography.

As most of the distances involving tip movement are in the Angstrom range, a piezoelectric actuation system is required for its precision movement as well as positioning the tip within picometer range. In the piezoelectric material, all dipoles are lined up in one direction; external electric fields interact with these dipoles causing stresses which result in mechanical displacement. The linearity of these materials is ideal for STM applications. While the piezoelectric scanner can provide sub-angstrom resolution, it can only move over a very limited range of distance say several thousand angstroms. To place the sample within the vicinity of the tip, a coarse approach mechanism using a piezoelectric step motor is used.

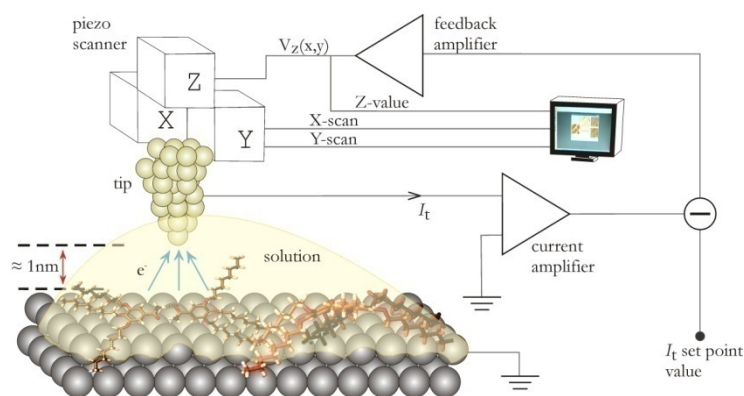


Fig. 2.1 Schematic diagram showing the operation of STM in solution-solid interface. The experiments are also done after complete evaporation of solvent from the surface

Since the current is of the order of 1-10 nA, a current-to-voltage conversion is necessary. The voltage signal is compared to a reference voltage that is the set point value for the tunneling current. The error signal determined by P-I (proportional-integration) feedback amplifier, which sends a voltage signal to the z-piezo. The feedback loop keeps the tunneling current at a constant value by adjusting the piezo-voltage and this piezo-voltage can be used to obtain a two-dimensional function $Z(x,y)$ which embodies the information about the electronic and geometric properties of the surface. In the constant-height mode, this becomes $I_t(x,y)$. The two-dimensional functions can be processed mathematically by a computer to provide three-dimensional images by converting the voltages on the piezoelectric manipulators into distances using the known piezoelectric coefficients. For a calibration of the piezo manipulator, structures of known spatial dimensions can be used like the unit cell distance of 0.246 nm of HOPG [35].

For any STM, the characteristic noise is composed by the $1/f$ noise created by the current preamplifier, typical integrator-like form of the feedback circuitry, fluctuation in the bias voltage, the ripple noise in the high voltage amplifier which actuates the piezoactuator and mechanical vibrations [36-38]. Those which possibly fluctuate to contribute the current noise are the tunneling barrier height Φ and the tip-sample distance d . Under ambient

conditions, the noise level can be high due to the dynamic nature of the system-desorption and adsorption of molecules coexist on the surfaces of sample and tip. Another crucial factor affecting the image quality in ambient environment is the thermal drift, which can usually be very large, as variations of $1/10^\circ\text{C}$ can cause significant variations in the length of the steel sample holder.

2.1.1. STM Theory

The condition of tunneling involving two metals under a positive bias of the tip is shown in Fig. 2.2. For zero bias, the Fermi levels of the electrodes are at the same energetic level; for simplicity, both electrodes are assumed to have the same work function Φ . With an applied bias V , the energy levels of the sample are shifted by an amount eV .

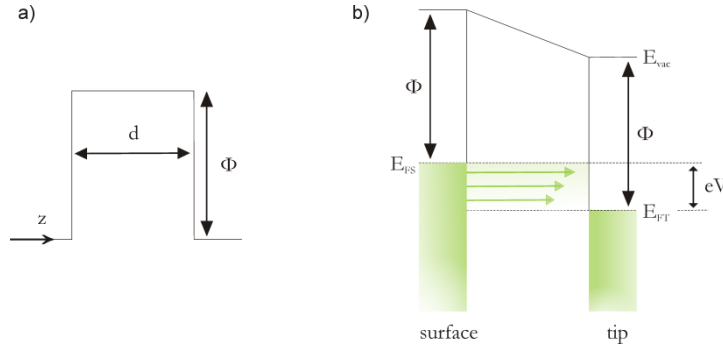


Fig. 2.2(a) Rectangular potential barrier of height Φ and width d . (b) Two similar metals under a positive tip bias

An exact treatment of the tunneling process is difficult due to the lack of detailed information about the quantum mechanical tip and sample states. A simplified picture of the tunneling process is given by the one-dimensional tunneling. Consider a potential barrier of width d and height Φ . For an electron with mass m and energy E , the solution for the Schrödinger equation in the classically forbidden region is

$$\psi(\xi) = \psi(0)e^{-\kappa\xi} \quad (2.1)$$

where

$$\kappa = \frac{\sqrt{2m(U - E)}}{\hbar} \quad (2.2)$$

Here the probability ω for observing an electron at the end of the barrier at $\xi = d$ is

$$\omega \propto |\psi(d)|^2 = |\psi(0)|^2 \exp(-2\kappa d) \quad (2.3)$$

Here, $U = \Phi$ is the work function of the metal. The electron can tunnel from one metal to the other in both directions but there is no net tunneling current. With a bias voltage V , and assuming $eV \ll \Phi$, the probability ω for an electron in the n^{th} sample state Ψ_n with the energy E_n to be present at the tip surface in the allowed energy window ($E_F, E_F + eV$) is

$$\omega \propto |\psi_n(d)|^2 = |\psi_n(0)|^2 \exp(-2\sqrt{2m\Phi}d / \hbar) \quad (2.4)$$

The tunneling current is a contribution of all sample states within E_F to $E_F + eV$

$$I \propto \sum_{E_n=E_F-eV}^{E_F} |\psi_n(d)|^2 \quad (2.5)$$

For small eV , this sum can be replaced with the *local density of states* (LDOS) of the sample at the Fermi level E_F

$$I \propto V \rho_s = V \rho_s \exp(-2\sqrt{2m\Phi}d / \hbar) \quad (2.6)$$

Thus at low bias, a constant-current STM image is a contour map of the sample LDOS at E_F . The exponential decay of the tunneling current I with tip-sample distance d , is the reason behind the atomic resolution of STM. Typical work functions are of the order of 3 to 5 eV and typical gap spacing for STM operation are of the order of 0.4 to 0.6 nm. Changes in gap spacing of 0.1 nm can result in the tunneling current by an order of magnitude.

Bardeen in 1961 extended the one-dimensional tunneling to the three-dimensional case and introduced a method to calculate the tunneling current between two metal plates [39]. He considered the metal plates as two weakly coupled electrodes and obtained the wave functions for the stationary Schrödinger equations separately, and then calculated the rate of electron transfer between the two by using first order time-dependent perturbation theory. Just as the Fermi-Golden rule gives the probability ω of an electron to tunnel between states Ψ_μ and Ψ_ν ,

$$\omega = \frac{2\pi}{\hbar} |M|^2 \delta(E_{\Psi_\mu} - E_{\Psi_\nu}) \quad (2.7)$$

Bardeen, in a similar manner calculated the probability of tunneling from the amplitude of electron transfer, or the tunneling matrix element M

$$M = \frac{\hbar^2}{2m} \int_S d\mathbf{S} \cdot (\psi_\mu^* \nabla \psi_\nu - \psi_\nu \nabla \psi_\mu^*) \quad (2.8)$$

Here the integral has to be evaluated over the surface S enclosing the entire vacuum region separating the two electrodes. The net current is obtained by summing over all the states on both sides of the barrier

$$I = \left(\frac{2\pi e}{\hbar} \right) \sum_{\mu\nu} (f(E_\mu)[1 - f(E_\nu + eV)] - f(E_\nu + eV)[1 - f(E_\mu)]) |M_{\mu\nu}|^2 \delta(E_\mu - E_\nu) \quad (2.9)$$

Where $f(E)$ is the Fermi function for the thermally excited electrons at absolute temperature T , and the delta function δ describes the conservation of energy for elastic tunneling.

Tersoff and Hamann [40, 41] extended this concept to the tip-sample geometry of STM, assuming the so called *s-wave approximation*. This model has been successfully used for some systems but it is not generally applicable due to the many simplified assumptions about the experimental conditions. They considered the limit of small voltage and low temperature where only the energy levels near the Fermi energy E_F are involved in the tunneling process. For small thermal energies $k_B T$, the Fermi function can be approximated by a step function. Thus the equation simplifies to

$$I = \left(\frac{2\pi e^2}{\hbar}\right) V \sum_{is} |M_{is}|^2 \delta(E_s - E_F) \delta(E_t - E_F) \quad (2.10)$$

Using *s-wave* wavefunction model for the tip, it is possible to obtain

$$\rho(\mathbf{r}_0, E_F) \equiv \sum_s |\psi_s(\mathbf{r}_0)|^2 \delta(E_s - E_F) \quad (2.11)$$

In short, at low voltages, the tip follows a contour of constant LDOS of the sample at E_F . At higher bias voltages, if $|M|$ does not change appreciably in the interval of interest, the tunnel current is represented by a weighted integral over a range of energies

$$I_t(V) \propto \int_{E_F}^{E_F + eV} -\rho_s(E) \rho_t(E + eV) T(E, eV) dE \quad (2.12)$$

That is, the tunnel current is proportional to the convolution of the DOS of the tip and the sample. Here T is the transmission coefficient. Although these results provide a strong foundation to understand STM imaging, they are based on much simplified assumptions of the real experimental conditions. For instance, if the barrier height is of the order of the thermal energy, thermal excitations leading to transport across the barrier must be taken into account. For the case of a bias voltage modifying the barrier height, the tunneling obeys the Fowler-Nordheim approximation. Also, most of the standard models are based on single molecule measurements where in reality an ensemble of molecules is measured.

2.1.2. STM imaging of surfaces and adsorbates

Fig. 2.3 illustrates the case when the tunneling process also involves a molecule adsorbed on the surface. The alignments of the occupied and unoccupied molecular orbitals in the diagram are shown symmetric with respect to the Fermi level.

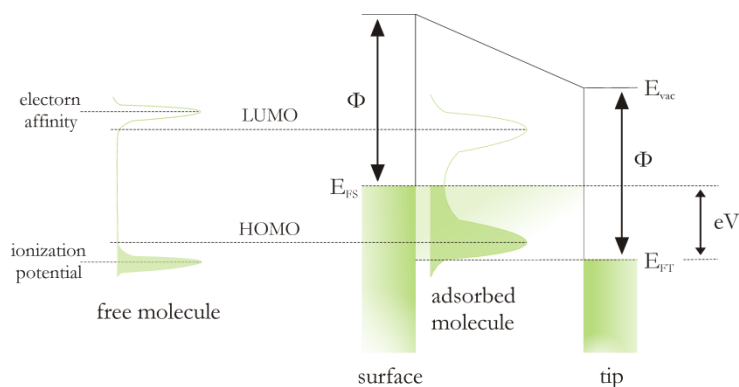


Fig. 2.3 Tunneling involving an organic molecule adsorbed on the surface. As a consequence of adsorption, there is a shift in the frontier orbitals of the molecule [42].

In general this may not be the case particularly with regard to the position of highest occupied molecular orbital (HOMO) and lowest unoccupied molecular orbital (LUMO) levels. Their approximate position is estimated by pinning the vacuum level of the isolated molecule to that of the substrate. When a molecule or atom is weakly physisorbed on the surface, a shift occurs in the energy levels of the frontier molecular orbitals as well as in

electronic energies of the surface. It was shown for the benzene-graphite physisorbed system that the gap between frontier orbital energies is considerably reduced by electron correlation effects resulting from surface polarization [42]. Another example is the Newns-Anderson model of adsorption on a jellium surface [43] predicting a broadening of energy levels based on the uncertainty principle. As the adsorbate approaches the surface, there is a finite probability for an electron from the surface to jump to the adsorbate and a different electron to jump from the adsorbate to the surface. Therefore, if the electron has a finite lifetime on the adsorbate, the adsorbate levels will be broadened by an amount given by $(\Delta E)(\Delta t) \geq 2\pi\hbar$.

As described in the previous section, an STM image is not directly related to the atomic structure or topography of the sample but to the local density of states (LDOS) distribution near the Fermi energy E_F [42]. STM imaging of bare surfaces [37, 44-46] is a fairly understood mechanism. But when it comes to molecules adsorbed on surfaces, many complexities arise. In general, the origin of STM image contrast involving adsorbates can be broadly classified into topographic/geometric and electronic factors. The topographic effect is easy to understand and is linked to the exponential decay of tunneling current with distance [47]. This means that large atoms or molecular groups, which will be protruding farther from the surface, provide a large ‘antenna effect’ and are imaged as protrusions. Theoretical calculations showed that topographic effects will dominate the STM images of alkanes and substituted alkanes on HOPG [48].

An observation of molecules adsorbed on a substrate by STM is possible if the molecule sufficiently modifies the tunneling current. This can happen either by a modification of the tunneling barrier or by a local modulation of the density of states due to molecule-substrate interaction. An alternative model is the resonant tunneling as illustrated in Fig. 2.3. Here the interaction with the surface broadens and shifts the molecular electronic levels, which results in a contribution to the LDOS at energies close to E_F . This type of behavior is observed for the case of molecules possessing aromatic moieties. The workfunctions of the electrodes are usually around 4 eV, and typical bias voltages for imaging a molecule-substrate system are around 1 V.

The HOMO-LUMO gap of organic molecules is large; for example alkanes have a 8-10 eV gap due to the σ -bonds constituting the molecules. Therefore an alignment of the HOMO or the LUMO with the Fermi energy E_F of the contacting metals cannot be expected. For a weak electronic coupling, the broadening of molecular states is small. For a large HOMO-LUMO gap compared to the applied bias, the energy of the molecular states is far from the Fermi energy. However experiments show that tunneling current reflects distinctly different contrast for alkyl and aromatic parts [49]. This cannot simply be a topographic effect but can be attributed to resonant tunneling due to the broadening of molecular levels. At sufficiently large applied voltages, the energy of these molecular resonances falls in the energy window. Then tunneling is allowed and the topography may show sub-molecular resolution. The geometry or the shape of the adsorbate being

reflected in the STM image is determined by the degree of electronic coupling between the frontier orbitals of the adsorbate and the substrate. Fig. 2.3 illustrates the broadening of the thin Dirac-like resonances on deposition on a surface [42]

In general, the interpretation of STM imaging involving organics is not straightforward [50, 51] and many factors have to be taken into account, depending on the specific system under study. Generally non-conducting organic molecules can be imaged by STM when deposited on a conducting substrate like HOPG. Literature provides some of the proposed mechanisms for STM image contrast, predominant of them being interaction between molecules and substrate [52, 53] and resonant tunneling dominated by frontier molecular orbitals [54-56]. Molecular orbitals contain electrons and if the tunneling electron has the same energy as a molecular orbital, the tunneling probability increases drastically due to the resonant tunneling effect. Therefore at the position of molecular orbitals, the tunneling current is larger and the shape of the molecular orbital can be imaged.

With regard to resonant tunneling mechanisms, some clarification is required on the image contrast dependence on bias polarity. The STM image contrast has a dependence on both magnitude and polarity of the bias [57]. For metal surfaces, the LDOS distribution of the occupied and unoccupied states is very uniform, so the resulting images are similar under different bias polarities. But the electronic structure and LDOS distribution of molecules are usually more complicated. In some cases, STM can have been successfully used to image the frontier molecular orbitals by changing the bias polarity [58] like for the case of chrysene on HOPG [57]. But this is by no means a general feature of organics imaging by STM, as it cannot be expected in all cases to have a symmetric alignment of frontier molecular orbitals with respect to the Fermi level of the substrate. In fact there are reports showing that the LUMO lies closer to the Fermi level than the HOMO, giving a predominant contribution from the LUMO both in the positive and negative bias voltages [54]. The unfilled orbitals being more spatially dispersed and nearer to the Fermi energy, tunneling from LUMO dominates than from HOMO [56, 59]. This explains why in most cases involving adsorbates, there is no change in the image observed when the polarity is reversed. In some cases, neither the HOMO nor the LUMO alone could explain the observed image contrast as in the case of a liquid crystal molecule on HOPG [60].

Other theories behind STM image contrast include the influence of the applied electric field [61] and the molecule polarizability influencing the LDOS near the Fermi energy or the substrate's work function [62]. There is a vast literature shedding light on the influence of different aspects in organic molecular imaging by STM such as the influence of the scanning angle [63], scanning in air [64], tip influence [65, 66], bias magnitude and polarity [55, 57, 58, 67, 68], topography as well as electronic effects [69], physisorbed systems [55], systems involving alkyl/alkyl derivatives [70, 71],[48, 72], adsorbed species on HOPG [73] [74] [75] [72] and others [69]. At the liquid-solid interface, even with the monolayer present,

the underlying substrate can be imaged by applying low voltages which might be due to the mechanical removal of molecules by the tip [75] [76] or due to the transparency of the molecular layer at low voltages. It should be mentioned that for molecules with orbital electrons like carbon-carbon double/triple bond or delocalized π orbitals adsorbed on a surface like graphite, which also has electron π orbitals, interpretation may require electronic structure calculations.

2.2. Atomic Force Microscope

The atomic force microscope (AFM) is another versatile scanning probe technique, although in general the resolution is smaller than that of the STM. To obtain information about the sample, AFM uses force instead of tunneling current [77], and therefore is not limited to conducting specimens. The tunneling current is a monotonic function of distance but force is not.

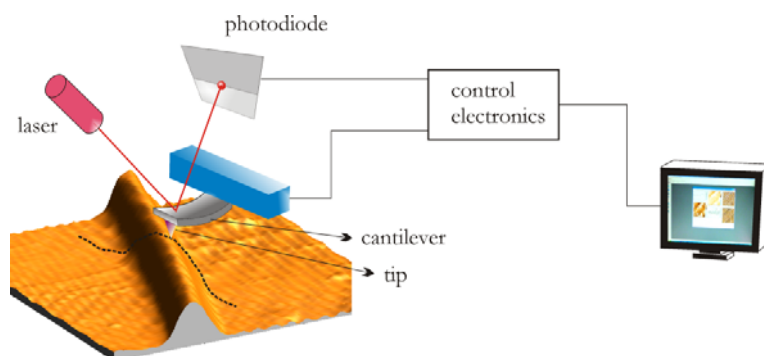


Fig. 2.4. Schematic of AFM in contact-mode operation

The contact-AFM operates in the repulsive regime of the force-distance curve. In the contact-AFM mode, the tip attached to a cantilever makes soft physical contact with the sample, a repulsive force acts on it which increases with decreasing distance. The force translates into a deflection $q = F_{ts}/k$ of the cantilever, where k is the spring constant and F_{ts} is the force between tip and sample. In the static or contact-mode, the cantilever should be much softer than the bonds between the bulk atoms in the tip and sample. Thus typical values for k are in the range 0.01 to 5 N/m. The cantilever bending due to this force can be measured with a laser beam deflection system. As the slope of the van der Waals curve is very steep in the repulsive regime, there is a bending of the cantilever rather than forcing the tip atoms closer to the sample atoms. In ambient conditions, a capillary force exerted by a thin layer of water can be present. In static atomic force microscopy, the imaging signal is given by the d.c deflection of the cantilever which is subject to $1/f$ noise.

Chapter 3

Materials

This chapter serves as a prelude to the forthcoming chapters and gives an overview of the materials used, followed by a brief introduction into the physical/chemical background. This includes introduction of all organic molecules and solvents used, substrates, preparation methods and a brief discussion of various interactions involved in supramolecular assembly as well as theoretical aspects of physisorption.

3.1. Substrate

Suitable substrates are to be chosen for STM studies so that the molecule-molecule interactions are not completely masked by molecule-substrate interactions. For graphite being chemically inert, the substrate-induced perturbations are minimal. The main substrate used for this thesis work is highly oriented pyrolytic graphite (HOPG)¹. The only other substrate used is Gold, used for some supplementary AFM measurements.

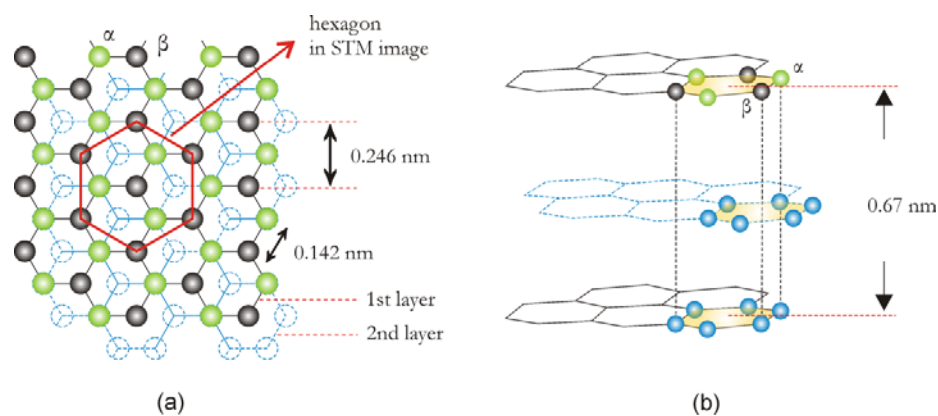


Fig. 3.1 (a) In-plane and (b) inter-plane structure of graphite

Pyrolytic graphite is a unique form of graphite manufactured by decomposition of hydrocarbon gas at very high temperature in a vacuum furnace resulting in an ultra-pure product with near theoretical density and high anisotropy. The 'highly oriented' refers to the high degree of mutual orientation in the c-direction. Graphite is chosen also due to its electrical conductance, atomic flatness and ease of surface preparation. HOPG, as

¹ 12*12*1 mm, ZYB grade, SPI supplies, West Chester, PA, USA

obtained from the manufacturer is cut into a dimension to match that of the aluminium disk of the sample holder and glued using a conducting silver epoxy.

Graphite is a semimetal with a layered structure in which atoms are organized in a hexagonal pattern within each layer and with an ABAB stacking perpendicular to the layers. The individual layers are called graphene sheets. Graphite has sp^2 hybridization which results from $2s$, $2p_x$ and $2p_y$ orbital electrons combining to form three hybridized orbitals lying at 120° to each other within a plane. Thus each carbon is covalently bonded to three neighboring carbon atoms (σ bond). The carbon-carbon covalent bond is one of the strongest chemical bonds. The $2p_z$ electron forms an out-of-plane weak bond with a delocalized orbital of π symmetry. This delocalization stabilizes the in-plane carbon bonding so that the bond strength is higher than that of a single covalent C-C bond [78]. The graphene sheets are held together in the c -direction mainly by weak van der Waals forces. Thus fresh atomically flat graphite surfaces can easily be prepared by cleaving the HOPG sample.

The high in-plane conductivity of HOPG originates from the overlap of the extended π – electron systems of the graphene sheets. The electronic properties of graphite near the Fermi energy are determined by delocalized states. The electronic band structure consists of four occupied valence bands (one σ and three π bands) and the corresponding antibonding bands forming the empty states above E_F . The bonding and antibonding σ bands are separated by a large energy gap but the potential arising from the sp^2 -bonded hexagonal sheets cannot distinguish between the bonding and antibonding π states at the Fermi level [79]. These two bands formed from the π states touch each other at E_F ($E_F = 4.7$ eV). The graphite monolayer is a zero-gap semiconductor in which a single state at the corner of the surface Brillouin zone determines the Fermi energy. The metallic character of graphite results from the non-vanishing density of states near the K and H - point [80].

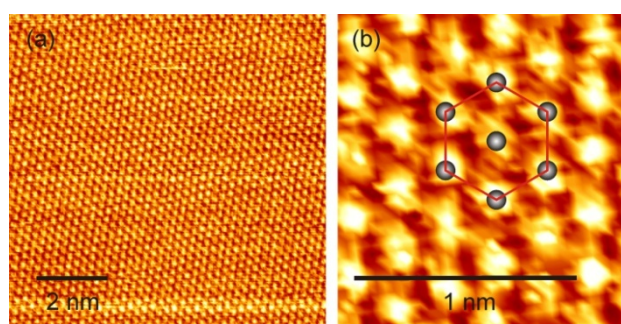


Fig. 3.2 STM image of (a) bare HOPG(0001) surface (image size $9.1 \text{ nm} \times 9.1 \text{ nm}$) and (b) The hexagon shown in Fig. 3.1.(a)

The AB stacking of graphene planes results in an asymmetry of adjacent carbon atoms referred to as α and β carbon atoms of graphite (0001) surface. The β carbon has no neighbor in its immediate layer underneath, as shown in the arrangement in Fig. 3.1(b). This asymmetry in turn, results in an asymmetry in their tunneling response. Therefore,

STM can usually image only every second carbon atom of the (0001) graphite basal plane [81]. Fig. 3.2(a) shows an STM image of HOPG showing only the β carbon atoms with a surface unit cell distance of 0.246 nm. The weak van der Waals interaction between adjacent planes leads to a suppression of the charge density at the Fermi level at α sites [81] what is the reason that only the β carbon atoms can be imaged.

3.2. Solvent, Molecules and Sample preparation

For STM studies at liquid-solid interfaces, choice of the proper solvent is crucial. It is important to have solvents with low dielectric constant and high boiling point/low vapor pressure.

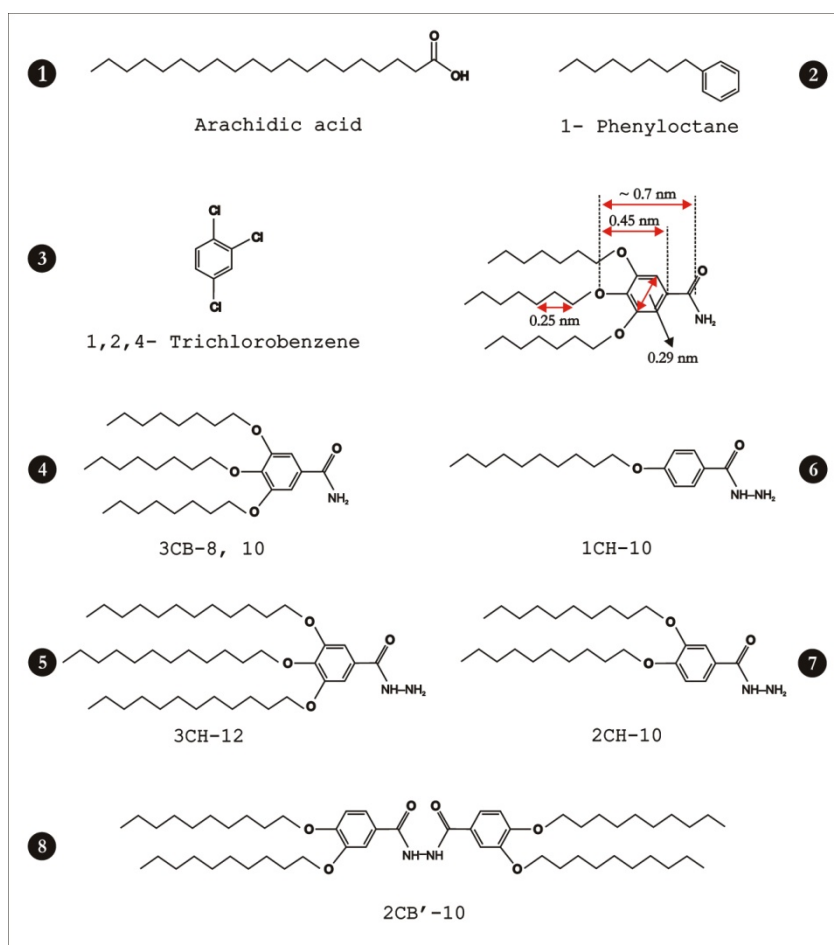


Fig. 3.3. Overview of molecules and solvents used in the thesis: (1) Arachidic acid ($C_{19}H_{39}COOH$), (2) 1-Phenyl octane ($C_{14}H_{22}$), (3) 1,2,4-Trichlorobenzene ($C_6H_3Cl_3$), (4) 3,4,5,-Tris(alkoxy)benzamide-n (3CB-n); n=8,10. (5) 3,4,5,-Tris(alkoxy)benzoylhydrazine (3CH-12), (6) 4-Alkoxybenzoylhydrazine (1CH-10), (7) 3,4-Bis(alkoxy)benzoylhydrazine (2CH-10) and (8) N,N'-Bis[3,4-bis(alkoxy)benzoyl]hydrazide (2CB'-10).

The solvent used is 1-phenyl octane ($C_{14}H_{22}$) (boiling point= 261-263 °C, dielectric constant $\epsilon = 2.5$) for arachidic acid and 1,2,4-trichlorobenzene ($C_6H_3Cl_3$)(boiling point = 214.4 °C, dielectric constant $\epsilon = 2.24$ (at 25°C)) for liquid-crystalline amphiphilic molecules. Although other solvents like tetrahydrofuran (THF) were tried for the latter, they were not

particularly suitable for these molecules. The chart shown below summarizes the molecules and solvents used in this work.

Just before the deposition of molecules, HOPG is cleaved using an adhesive tape. Upon cleavage, the surface comprises of atomically flat terraces ranging in size from a few hundred nanometers to tens of micrometers. This bare HOPG is first imaged at atomic resolution by STM to check the tip quality.

The solution is prepared by a dilution-series method in steps of 1/10. Serial-dilutions are made by using the previous dilution as the input to the next dilution in each step. Four or five concentrations of solution are prepared for each molecule. For example, one starts with weighing approximately 10 mg of the molecule and add 100 mg of solvent. This is the mother solution, with a known concentration. In order to make dilution in a 1/10 series, take 10 mg of the solution from the mother solution and add 90 mg of solvent. This now gives a concentration which is 1/10 of the mother solution. For the next step, i.e., to make a 1/100 solution, 10 mg of the solution is taken from the 1/10 solution. This process continues until the required concentration level is reached.

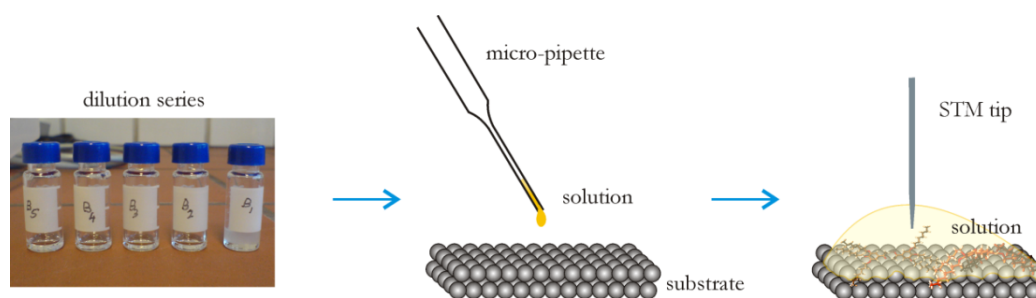


Fig. 3.4. Sample preparation for STM studies at liquid-solid interface. Solvent may or may not be present depending on the particular experimental conditions.

Before depositing the molecule on HOPG, usually it is sonicated for 10 to 15 minutes at 45 to 55 °C. A drop of the solution is deposited on the HOPG basal plane using a micro-pipette (Fig. 3.4). When the STM tip approaches the sample, the solution may or may not make a meniscus with the tip depending on the specific molecule and the concentration. The STM tips used are mostly mechanically sharpened Pt/Ir 80/20% wires². In the experiments, Pt/Ir tips gave better resolution than electro-chemically etched Tungsten tips. The tip quality can be improved by applying a high voltage pulse which may remove contaminants.

3.3. Interactions in Supramolecular Systems

Supramolecular chemistry is the chemistry beyond covalent bond. Non-covalent interactions play an important role in both biological systems as well as synthetic molecular

² Goodfellow Cambridge limited, Huntingdon, UK

and supramolecular structures. Some predominant interactions involved in supramolecularly assembled systems are discussed below.

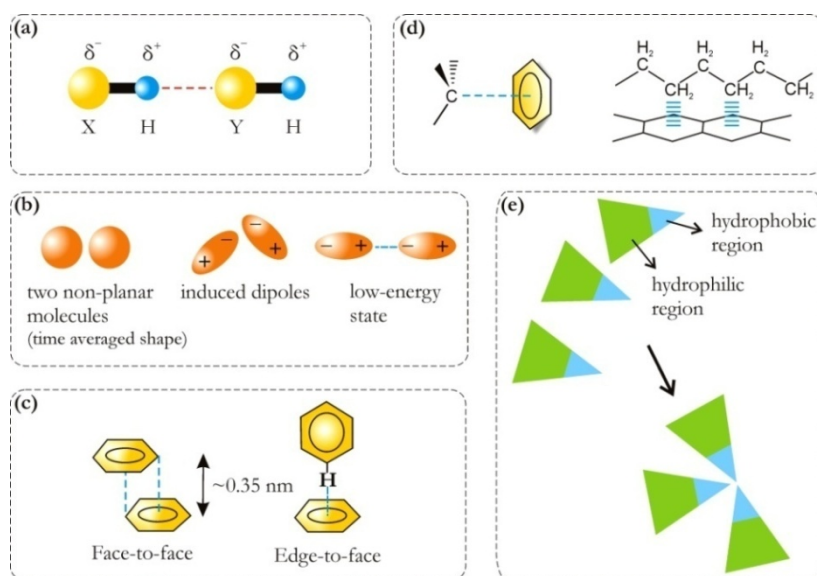


Fig. 3.5 Various non-covalent interactions involved in supramolecular self-assembly.

1. Hydrogen bonding

This is the most commonly observed interaction in supramolecular self-assembled systems. This is a donor-acceptor interaction specifically involving hydrogen atoms and can be regarded as a particular kind of dipole-dipole interaction (Fig. 3.5(a)). This attractive force predominantly involves electrostatic interaction between a slightly positive charge on a hydrogen atom and a slightly negative charge on a nearby atom such as N, O or F. Very strong hydrogen bonds are similar to covalent bonds, while very weak hydrogen bonds are close to van der Waals forces. Unlike for covalent, ionic or van der Waals forces, hydrogen bond energies extend over a wide range from about 15-40 kcal/mol for strong bonds, to 4-15 kcal/mol for moderate bonds, and 1-4 kcal/mol for weak bonds [82]. Compare this with the average thermal (vibrational) energy at room temperature, which is ~ 5 kcal/mol, and with the energy needed to break a covalent bond which is ~ 80 kcal/mol. Although the hydrogen bond is relatively a weak bond, mostly multiple hydrogen bonds are involved and they add up. Strong hydrogen bonds are formed when there is a deficiency of electron density in the donor group, i.e., O^+-H , or an excess of electron density in the acceptor group like in F^- , O^---H etc. A deficiency of electrons of the donor group further deshields the proton thereby increasing the positive charge, while an excess of electrons on the acceptor group increases its negative charge. For this reason, sometimes they are referred to as ionic hydrogen bonds. Moderate hydrogen bonds are formed generally by neutral donor and acceptor groups like O-H, N-H etc. in which donor X atoms are electronegative to hydrogen and the acceptor Y atoms have lone-pair unshared electrons. These are the two *normal* hydrogen bonds found in nature and chemistry. The weak

hydrogen bonds are formed when the hydrogen atom is covalently bonded to a slightly more electroneutral atom relative to hydrogen, as in C-H, Si-H or when the acceptor group has no lone-pairs but has π electrons, such as $C\equiv C$ or an aromatic ring [82].

2. Van der Waals Interaction

This is an attractive force occurring by means of fluctuations in the electric dipole moment of atoms and their mutual polarization, when any two atoms come into close proximity to each other (Fig. 3.5(b)). A transient polarity is induced which results in an attractive force of the order of ~ 1 kcal/mol. This kind of bonding is abundant in gases and organic liquids/solids. In the case of adenine on graphite or other nucleobases on graphene, weakly attractive dispersive forces have been shown to be the governing interaction [83, 84]. It is also the main force behind the physisorption of aliphatic molecules on surfaces. There are three different sources of van der Waals forces between molecules and surfaces: (1) the center of negative charge of the electrons and the center of positive charge of the atomic nuclei do not coincide at surfaces, an electrostatic dipole layer is thereby created that may interact with a polar molecule, (2) polar molecules temporarily induce image dipoles in the surface charge distribution which causes an attractive interaction and (3) even for molecules without a permanent dipole moment, centers of positive and negative charges are not likely to coincide, the fluctuation of electrons thus make molecules time-varying dipoles. Such time-varying dipoles induce image dipoles in the substrate, resulting in attractive forces known as London forces. At close distances, short-range repulsive interactions also contribute, giving an expression for overall van der Waals interaction energy,

$$E_{vdW} = -\frac{c_1}{R^6} + \frac{c_2}{R^{12}} \quad (3.1)$$

3. π - π Interaction

The π - π interaction is another common interaction in supramolecular architectures, which is the best known interaction between aromatic rings [49, 85]. This can generally be classified into either face-to-face or edge-to-face stacking (Fig. 3.5(c)) although a wide variety of intermediate geometries are known. The electrostatic component of the π - π interaction has its origin in the quadrupole moment of aromatic rings. The main attractive interactions between aromatic molecules are London dispersion forces; to maximize these interactions, the surfaces of both aromatic molecules must overlap. Typical interaction energy is about 2-3 kcal/mol. Aromatic rings can also form hydrogen bonds and interact with cations.

4. CH- π Interaction

The CH- π interaction in supramolecular assemblies is a lesser understood phenomenon pertinent to alkyl chain-graphite interaction. The alkyl chain- graphite adsorption is

analogous to the CH- π interaction between benzene-methane systems. This is the attractive interaction between a C-H bond and an electron system (Fig. 3.5(d)). The interaction strength lies between the weakest class of hydrogen bonds and the van der Waals force. The physical origin of this interaction has not been fully understood but believed to be of dispersive origin [86].

5. Hydrophobic Interaction

The Hydrophobic effect (Fig. 3.5(e)) plays an important role in many phenomena such as protein-folding and lipid aggregation. When it comes to supramolecular structures, mostly entities with a hydrophobic part are involved, which contribute to the hydrophobic interactions. Hydrophobic interactions involve uncharged and non-polar molecules that do not interact with water. It is for this reason that hydrocarbons are so sparingly soluble in water. But the interaction between a hydrophobic molecule and water is actually attractive, due to dispersion forces. In general, the strong tendency of water molecules to form hydrogen bonds with each other influences their interaction with non-polar molecules that are incapable of forming hydrogen bonds (e.g., alkanes, hydrocarbons, inert atoms)[87]. The equivalent of hydrophobicity in non-aqueous media is called solvophobicity.

In addition to the interactions discussed above, other interactions such as solvent-molecule and solvent-substrate are present at the liquid-solid interface. During STM operation in air, capillary forces are also present between tip and sample [64].

3.4. Physisorption Theory

The adsorption of the reactants is usually the first step in a reaction on a surface. Adsorption is a process where molecules from the gas phase or solution bind in a condensed layer on a solid or liquid surface [43]. The molecules that bind to the surface are called the adsorbates. Generally one gets multilayer adsorption when the adsorbate-adsorbate interactions are large compared to kT . On the other hand, monolayer adsorption is usually dominated by the direct interaction between adsorbate and the substrate and can be achieved at higher temperatures. There are two different types of adsorption: chemisorption and physisorption, although it is not possible to discriminate between them in every case. An adsorbing molecule is usually assumed to be chemisorbed when the adsorbate's bond energy to the surface is more than 10 kcal/mol, and physisorbed if it is less than 10 kcal/mol [88]. However a precise distinction is somewhat arbitrary. In chemisorption, there is a chemical bond between the adsorbate and the surface and in physisorption, there is no direct bond and only physical (van der Waals) forces are involved. In chemisorption, due to the sharing of electrons, the adsorbate's electronic structure is significantly perturbed. In contrast, physisorption is governed by polarization forces and therefore the adsorbate's electronic structure is perturbed only to a much lesser extent. For simple molecules, typical energies are 15 to 100 kcal/mol for chemisorption and 2 to 10 kcal/mol for physisorption [43]. In most cases, physisorption

takes place first, followed by chemisorption. Alkanes on graphite and several noble metal surfaces are classified as physisorbed systems. For longer alkyne chains, the adsorption energy per molecule exceeds 9 kcal/mol [89].

There are only two major interactions contributing to physisorption process: long-range van der Waals attractive forces and short-range repulsive forces. The attractive van der Waals interactions are caused by the quantum mechanical fluctuations of instantaneous dipoles, originating from the mutual interaction of electrons in the adsorbate and the surface. At intermolecular distances smaller than equilibrium distances, molecular orbitals start to overlap. This leads to repulsion due to the Pauli principle, as well as increased Coulomb repulsion due to lesser screening of the nuclei. A physisorbed state is a balance between these attractive and repulsive potentials. A brief look in to the theoretical aspects of physisorption follows.

London [90] provided the first quantitative model of adsorption resulting from physical (van der Waals) forces. He assumed a pair-wise additive potential between adsorbate and atoms of the surface. When a non-polar gas interacts with a non-polar, nonmetallic substrate, the molecule interaction with a surface atom can be represented by a Lennard-Jones 6-12 potential

$$E_{Ma} = C_{Lond} \left(\frac{0.5(r_{eqb})^6}{|\vec{r}_M - \vec{r}_s|^{12}} - \frac{1}{|\vec{r}_M - \vec{r}_s|^6} \right) \quad (3.2)$$

where r_{eqb} is the equilibrium distance when an adsorbate molecule interacts with an isolated surface atom. C_{Lond} is given by the so called London Eqn.,

$$C_{Lond} = 1.5\alpha_M\alpha_s \frac{I_M I_s}{I_M + I_s} \quad (3.3)$$

here α_M , α_s are the polarizabilities and I_M and I_s are their ionization potentials. Now, the total potential energy of the approaching molecule will be sum of all pair-wise potentials. This is because the dispersion interaction results from small perturbations of electronic states, so that many such perturbations can add without much mutual interactions.

$$E_M(\vec{r}_M) = \sum_s E_{Ma}(\vec{r}_M - \vec{r}_s) \quad (3.4)$$

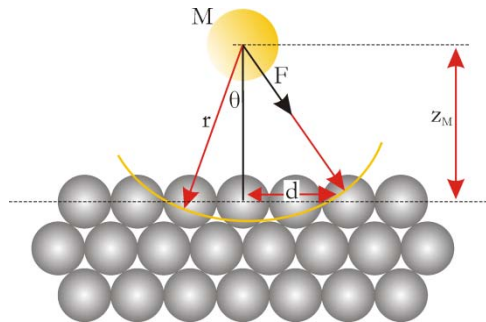


Fig. 3.5. A molecule M placed at a distance of z_M from the surface

London simplified the sum in Eqn.(3.4) by using the geometric construction shown in Fig. 3.5. He neglected the fact that each surface atom will be pulling the molecule in different directions and also assumed that all atoms are identical and uniformly distributed over the solid, the sum can thus be replaced by an integral of the form

$$E_M(\tilde{x}_M) = \rho_{surf} \int_{\tilde{x}_M}^{\infty} \int_0^{\arctan(d/r)} \int_0^{2\pi} E_{Ma}(r) r^2 \sin\theta d\phi d\theta dr \quad (3.5)$$

Where ρ_{surf} is density of atoms of the surface. Substituting Eqn.(3.4) into Eqn.(3.5) and integrating yields

$$E_M(Z) = \rho_{surf} \pi C_{Lond} \left(\frac{0.2(r_{eqb})^6}{\tilde{x}_M^9} - \frac{1}{\tilde{x}_M^3} \right) \quad (3.6)$$

The above Eqn. for non-metallic surfaces agree reasonably well with measurements, but less so for metal surfaces. Lennard-Jones showed that one can derive an approximation for the physisorption of a gas on a metal surface, which is quite similar to the above Eqn. The plot of Eqn.(3.6) for an argon atom adsorbed on graphite surface showed a potential minimum of 2 Å away from the surface with an energy of 2.2. kcal/mol [43].

The interaction of a single atom with a surface has been considered thus far. The macroscopic approach involves considering the objects as continuous media, say interaction between two slabs of infinite extent and depth. The interaction energy is given by

$$E(Z)_{slab-slab} = -\frac{A}{12\pi Z^2} \quad (3.7)$$

Where A is known as the *Hamaker constant* and is equal to $\pi^2 n^2 C_1$ with $C_1 = 3\pi \hbar \nu_0 \alpha^2 / 2$; α , n being the polarizability and the number density of atoms. $\hbar \nu_0$ is approximately the ionization energy. For a sphere-slab or two crossed cylinders geometry, the interaction energy at small surface-to-surface separations is

$$E(Z)_{sphere-slab} = E(Z)_{crossed-cylinders} = -\frac{aA}{6Z} \quad (3.8)$$

In this case, $E(Z)$ has a simple inverse dependence on Z , indicating that the attraction is, indeed, long-range. When the two surfaces are interacting across a liquid, the Hamaker constant A takes more complicated forms. The dispersion interaction strength is reduced by the presence of an intervening fluid if the dielectric constant of the medium is larger than unity. An experimental analogy of the sphere-slab geometry is the weak interaction between a colloidal particle and a planar surface in a liquid.

Theoretical studies show that alkyl chains adsorb parallel to the graphite surface and show a tendency to self-organize, due to strong lateral interactions [91, 92]. For long-chain alkanes physisorbed on graphite, electrostatic interaction is small, and the adsorbate-substrate interaction is dominated by van der Waals forces. AS early as 1970, Groszek proposed a commensurate arrangement for n-alkanes on graphite from adsorption isotherm experiments [93]. Also adsorption stability increases proportionally with increase

in chain length [94]. The ration of adsorption to alkane-alkane crystallization energy in this case varies from 2.5 to 3.5 depending on the chain-length.

3.5. Thermodynamics of Adsorption

The self-assembly in solution is a thermodynamically controlled reversible equilibrium process. The most fundamental quantity in thermodynamics is the Gibbs free energy G . Any system will relax to the state of lowest *Gibbs energy*, G as long as no dynamical or kinetic constraints exist. Therefore, a spontaneous change is always accompanied by a decrease in Gibbs energy, i.e. $\Delta G < 0$ for all spontaneous processes. Adsorption reduces the imbalance of attractive forces which exist at the surface and hence the free energy of the system. Free energy G is related to enthalpy H and entropy S , through the relation

$$\Delta G = \Delta H - T\Delta S \quad (3.9)$$

Adsorption confines a gas to a surface, which means that $\Delta S < 0$ for the adsorbate. Therefore, in order for ΔG to be negative, i.e. for spontaneous adsorption, ΔH must be negative (exothermic). The degree of adsorption increases with decreasing temperature [95]. The surface molecules are practically fixed in position, and cannot move. As a result, solid surfaces cannot spontaneously contract to minimize their surface area and a non-equilibrium surface structure forms. This situation is quite different in the case of a liquid surface, which attains equilibrium as soon as it is formed because of the mobility of surface molecules. The physisorbed molecules are free to move and rotate and can diffuse laterally along the surface of the adsorbent. Physisorption is reversible as molecules are only weakly bound. Also due to the much weaker adsorbate-surface interaction, which may become comparable to the adsorbate-adsorbate interaction, the condition will generally not be confined to the first monolayer but may also include the formation of multilayers and finally a complete condensation [88]. An important observation of organic molecules having long aliphatic chains is the linear increase in the adsorption energy with the chain-length [96]

$$-\Delta G^0 = -\Delta G^{0,b} + N_c W \quad (3.10)$$

Where ΔG^0 is the free energy of adsorption at infinite dilution, $\Delta G^{0,b}$ is the contribution from the head group, N_c is the carbon number and W is the energetic contribution per methylene unit. In general, the tendency to form ordered monolayers increases with increased chain length as shown for alkanolic acid monolayers on aluminium [97]. The reason for this is either an increased van der Waals interaction between the aliphatic chains among themselves, or to the substrate

In spite of using thermodynamic quantities like the free energy G , the usual method employed is to determine the *adsorption isotherm function* θ , by measuring the adsorbed amount as a function of concentration at a given temperature. In dilute solutions, the treatment is similar to that for the gas adsorption. So, in general, a Langmuir isotherm is applicable to monolayer adsorption as well although very little kinetic data have been reported for these systems. It is the simplest model for the adsorption of molecules onto a solid surface [97]. Under simplified assumptions such as equivalent adsorbent sites and

non-interacting adsorbates, the bulk solute concentration can be related to the fractional surface coverage at an equilibrium state between condensation and evaporation as

$$\theta = \frac{bP}{1 + bP} \quad (3.11)$$

In contrast to Langmuir-Blodgett (LB) films, self-assembled monolayers (SAM's) have more stability due to strong physical or chemical bonds with the surface.

3.6. Fourier Transform and Image Processing

The frequency domain offers some advantages for image processing as the information in the frequency domain is effectively an averaged one, hence measuring the spot location and direction are easier. The fast Fourier transform (FFT) is one of the most powerful and efficient algorithm to calculate image transforms. It is possible to represent any space or time varying function $f(x)$ as a summation of sine and cosine terms, with a weighting factor corresponding to their respective contribution. The greater the number of terms included, the better the representation of the original function. The Fourier transform of the function $f(x)$ is written as $F(u)$ given by

$$F(u) = \int_{-\infty}^{+\infty} f(x)e^{-2\pi iux} dx \quad (3.12)$$

where $i = \sqrt{-1}$. Now, $f(x)$ can be recovered by an inverse transform

$$f(x) = \int_{-\infty}^{+\infty} F(u)e^{2\pi iux} du \quad (3.13)$$

The function $f(x)$ is a continuous function. In digitized images, the values of x are not continuous but discrete, such as quantized brightness values and pixel spacing. In general, $f(x)$ is a real function such as time-varying voltage or spatially-varying image brightness. But the transform function $F(u)$ is usually complex and the frequency spectrum can be displayed as the real and imaginary parts (Cartesian form) or as the magnitude and phase (polar form). In polar form, $F(u)$ can be expressed as

$$F(u) = |F(u)|e^{i\phi(u)} \quad (3.14)$$

$|F(u)|^2$ is usually referred to as the power spectrum or spectral density of $f(x)$. In practice the integrals from minus to plus infinity can be reduced to a summation of terms of increasing frequency, limited by the finite spacing of the sample points in the image. The discrete Fourier transform is

$$F(u) = \frac{1}{N} \sum_{x=0}^{N-1} f(x)e^{-i2\pi ux/N} \quad (3.15)$$

where N is the number of sample points along the function $f(x)$. The corresponding reverse transform is

$$f(x) = \sum_{u=0}^{N-1} F(u)e^{i2\pi ux/N} \quad (3.16)$$

The values of u from 0 to $N-1$ represent the discrete frequency components added to construct the function $f(x)$. The summation is normally performed over terms up to one-half the dimension of the image (in pixels), since to define the highest frequency requires

at least a minimum of two pixels brightness values. But each term has a real and imaginary part; therefore, the total number of values produced by the FFT is same as the number of pixels in the original image.

A direct extension from one-dimension to two-dimension can be made by substituting $f(x)$ and $F(u)$ by $f(x,y)$ and $F(u,v)$ and performing summation over two variables. Due to orthogonality of x,y and u,v dimensions, the summation can be performed separately in each direction. The resulting transform of the original image into the frequency space has complex values at each pixel. In most cases, the display is based only on the magnitude, ignoring the phase. Usually only the power spectrum $|F(u)|^2$ is used, and the spectrum is shifted to place zero frequency at the center. This organization is simpler to understand and to work with. The power at each location shows how much of a particular frequency is present in the image at that orientation is. In order to restore the original image, the phase information is also required, although it is rarely displayed and is usually difficult to interpret visually.

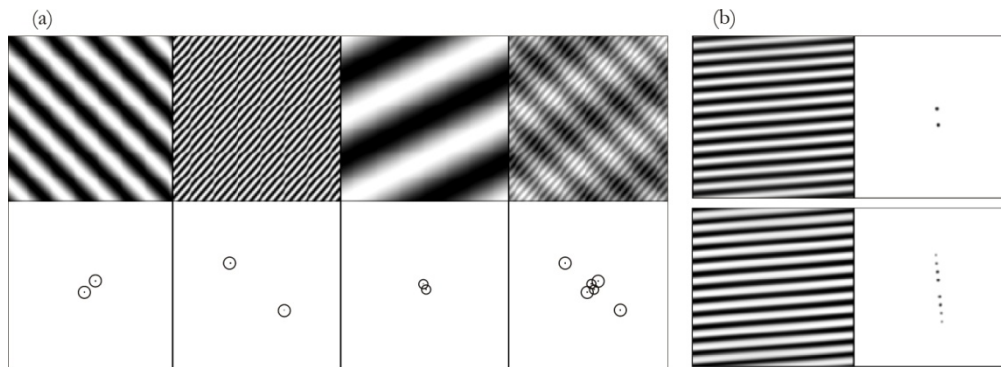


Fig. 3.6. (a) (Top) spatial domain and the corresponding (bottom) frequency spectrum. The fourth image is the sum of the first three (b) (top) Set of sinusoidal lines and the frequency transform, (bottom) same lines as on top with non-sinusoidal brightness profile (image courtesy of reference [98]).

For demonstration, some of the idealized cases are shown in Fig. 3.6, where peaks can be directly related to the real space data. The pair of points corresponds to two-dimensional sinusoids. The frequency and direction of each sinusoid is determined by the location of the pair of points in the frequency domain. If the spatial domain is continuous, the frequency domain is aperiodic with zero frequency at the center and the frequencies becoming higher out to infinity in all directions. In real images like in STM data, which also include non-periodic information, the peaks will be superimposed on a broad and sometimes noisy background.

Fig. 3.7 is a simple example of a lattice and its FFT showing the symmetry of the graphite (0001) surface. If the surface unit cell vectors in real space \mathbf{a}_1 and \mathbf{a}_2 are known (here 0.246 nm), corresponding Fourier vectors $\mathbf{A}_1, \mathbf{A}_2$ can be found out from the transformation Eqns.

$$\mathbf{A}_j = (\mathbf{a}_2 \times \mathbf{n}) / (\mathbf{a}_1 \cdot \mathbf{a}_2 \times \mathbf{n}) \quad (3.17)$$

$$\mathbf{A}_2 = (\mathbf{n} \times \mathbf{a}_1) / (\mathbf{a}_1 \cdot \mathbf{a}_2 \times \mathbf{n})$$

$$\mathbf{n} = (\mathbf{a}_1 \times \mathbf{a}_2) / |\mathbf{a}_1 \times \mathbf{a}_2| \quad (3.18)$$

where

and $\mathbf{A}_i \cdot \mathbf{a}_j = \delta_{ij}$; δ_{ij} being the Kronecker delta function.

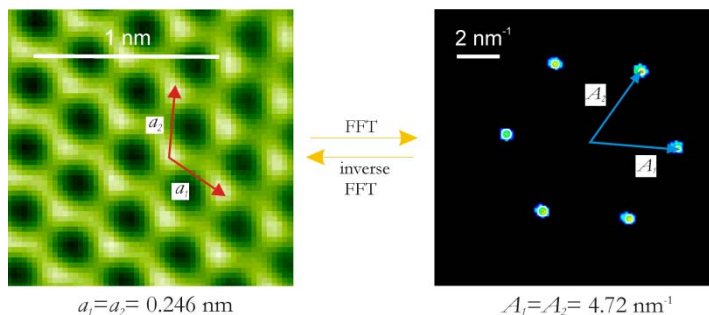


Fig. 3.7 A cut-out portion of STM image of HOPG and the fast Fourier transform power spectrum (FFT). The vectors in the images are graphite unit cell vectors of (0001) surface. The principal graphite directions in the FFT are rotated by 30° with respect to the direction in the real space as expected for any hexagonal lattice.

Normally, the location and direction of spots from the center in FFT represent the magnitude and direction of periodicity of the real space image. For hexagonal symmetry; however, there will be a rotation of 30° between the real and Fourier space vectors, as in the case of graphite in Fig. 3.6. For small-drift images, the spots of known lattice constants can be used to calibrate STM images using image-analysis programs like SPIP [99].

3.7. Prelude to Soft Matter and Supramolecular Chemistry

Molecular arrangement is crucial for molecular devices. The need to understand the solution-solid interface and bottom-up approach have fueled the 2-D supramolecular chemistry. Supramolecular chemistry uses molecules rather than atoms as building blocks. In contrast to the mature branch of covalent molecular species, the field of supramolecular chemistry is still in its infancy [100]. The main limitation for achieving designated supramolecular architectures is the relative weakness of intermolecular interactions such as hydrogen bonding, electrostatic, van der Waals, π - π stacking and hydrophobic effect. Hydrogen bonding has been explored in solution as a means to designing liquid crystalline materials from LMW complexes, and control their molecular architectures [101]. The most important type of interactions in organogels is hydrogen bonding [102] and hydrogen bonding sites are the functional units that lead to fibrous structures in organogelators [103]. The controlled formation of supramolecular structures in the solid state, in the mesophase and in solution, using the self-assembly strategy has been an active area of research.

Soft condensed matter comprises physical states such as liquids, gels, colloids, polymers and biological materials whose basic units consist of many atoms or molecules. They are easily deformed by thermal fluctuations at energy scales comparable with room

temperature. Soft matter can self-organize into mesoscopic physical structures that are much larger than microscopic scale and the properties and interactions at mesoscopic level determine the macroscopic behavior of the material. Aggregation processes are essential for life on this planet and membranes of all living cells are bilayered aggregates, consisting of lipid molecules, proteins and steroids. Amphiphilic molecules in solution can form a variety of molecularly assembled structures like gels, micelles, vesicles, tubes, and lamellas in different shapes and sizes. Langmuir, in 1917 showed that amphiphilic molecules composed of a hydrophobic tail and hydrophilic head group accumulate at the air-water interface [229]. Many of the molecules studied here exhibit columnar liquid crystal phase and therefore a brief discussion about basic liquid crystalline nature is inevitable. The attention here is not in pure liquid crystal research but their use in nanoengineering.

A liquid crystal (LC) state also called mesophase, is both a fluid as well as a crystal. The LC phases that occur only in a certain temperature range are called thermotropic phases and those that occur only in certain concentration ranges are called lyotropic phases. Some LC phases only exist in a super cooled state below the melting point and are termed *monotropic*; these phases are kinetically stable but will eventually crystallize. LC phases observable above the melting point are termed *enantiotropic* and are thermodynamically stable. In thermotropic liquid crystals, the phases of the liquid crystals may change with temperature. In lyotropic liquid crystals, the ordered crystalline state is disrupted more by the concentration of the solution than by temperature. Thermotropic organic molecules do not need a solvent to form a LC phase, while the lyotropic LC are formed by amphiphilic molecules in solution. Generally, the liquid crystal state (mesophase) exists within a certain temperature range, $T_m < T < T_c$, where T_m is the temperature of melting from the solid state into a mesophase, and T_c is the clearing temperature when the liquid crystal transforms into an isotropic liquid.

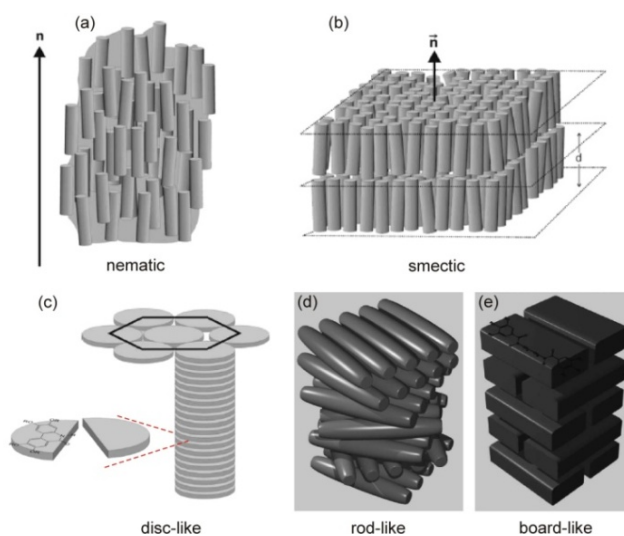


Fig. 3.8 (courtesy of [101]) (a) Nematic mesophase. (b) Smectic mesophase. (c), (d) and (e) Columnar mesophase formation from disc-like, rod-like and board-like mesogens.

LC molecules are also called mesogens. The simplest kind of liquid crystals consists of a single mesogenic core attached to one or two terminal groups usually of long alkyl, acyl, or alkoxy chains. The mesophase structures are not static and possess a considerable amount of mobility. The shapes of mesogens can be classified into three types: rod-like, disc-like and board-like (Fig. 3.8). Two important classes of thermotropic LC's are the nematic and smectic mesophases. The nematic phase only possesses an orientational order, with the mesogens aligned in one preferred direction but their centers of gravity randomly distributed. In smectic phase, centers of gravity of mesogens are in a plane in addition to some orientational order. The three different shapes (rod, disc, board) and two different mesophases (nematic, smectic) give rise to six different kinds of crystals.

The discotic smectic mesophase often forms columns and is hence called columnar mesophase. Rod-like mesogens have an elongated geometry which allows for preferential alignment along one spatial direction. Not only rod-like molecules, many compounds with disc-shaped molecules also exhibit stable thermotropic liquid crystalline phases [104], so now a days, the term 'columnar' is recommended rather than 'discotic'. Polymers may exhibit LC order either in the melt (thermotropic LC) or in the solution (lyotropic LC).

The synthesis of a liquid crystal in the form of supramolecular columns imparts certain properties on these materials that can be utilized for applications. One such property is the transport of charge along the molecular column. Apart from amide functionalities considered in this thesis, columnar mesophases have been known to form from dendrimer type building blocks [105] or other type of functionalities attached to an aromatic core [106-111]. The interest in stacked columns is due to their potential application as conducting wires. These columns with their π -stack exhibit high electron and hole mobility. The alkyl chains can act as an insulating layer, yielding, in principle, single cables that can be used as supramolecular conducting wires.

In inorganic semiconducting materials, charge transport occurs through wave-like propagation of carriers in well-established conduction or valence bands while in organic semiconductors, constituting molecules are only weakly bound and a traditional view of band formation cannot be expected. Therefore, the mechanism of charge transport cannot be the same as that of crystalline materials. In fact, thermally assisted *hopping* has been identified as the dominant mechanism of transport in organic semiconducting materials. The charge carrier mobility in amorphous organic solids is based on hopping transport within a spatially regular but energetically disperse system [112-119]. The energy disorder arises from small variations of molecular geometry due to packing constraints, or fluctuations in the polarization energy, or dipolar interactions. The density of states (DOS) profile of the hopping state distribution is Gaussian

$$\rho(\varepsilon) = (2\pi\sigma^2)^{-1/2} \exp\left(-\frac{\varepsilon^2}{2\sigma^2}\right) \quad (3.19)$$

And the carrier mobility has non-Arrhenius type temperature dependence

$$\mu = \mu_0 \exp\left[-(T_0 / T)^2\right] \quad (3.20)$$

Besides from lyotropic phases, well-defined columnar superstructures are found in supramolecular organogels. Several low-molecular-weight molecules can form organogels which contain self-assembled fiber networks. These fibers as one-dimensional conductors in gel materials have captured much interest in the field of nanoelectronics.

While LC's are ordered fluids, gels are multicomponent materials consisting of a solvent and at least one component that form an elastic three-dimensional network and concentration plays an important role in their appearance [120]. Physical gels comprise 3-D fibrous aggregates of low-molecular weight compounds, while; chemical gels consist of covalently-bonded 3-D networks. Unlike their chemical counterpart, gels formed by physical forces like weak intermolecular interactions are reversible (e.g. polyacrylate, polymethacrylate). A physical gel is formed when a hot solution of small molecular mass organic compound is cooled to a certain temperature namely T_g (gel point). The solute molecules at a concentration in excess of the equilibrium concentration at T_g self-organize by juxtaposing and interwinding into a 3-D fibrous network although the individual units still exist as monomers, dimers, trimers or other small entities.

Gels formed from LMW molecules are supramolecular in the strictest sense that they are formed through self-aggregation of small gelator molecules to form entangled self-assembled fibrillar networks through the combination of non-covalent interactions like hydrogen bonding, π - π stacking [121, 122], donor-acceptor interactions, metal coordination, solvophobic forces (hydrophobic forces for gels in water) and van der Waals interactions. Due to the weak interaction within these networks, they can be readily transformed in to a fluid (sol) by heating and are generally thermally reversible [123].

Gels of a LMW compound are usually prepared by heating the gelator in an appropriate solvent and cooling the resulting isotropic supersaturated solution to room temperature. When the hot solution is cooled, the molecules start to condense and three situations can arise (a) a highly ordered aggregation giving rise to crystals i.e. crystallization, (b) a random aggregation resulting in an amorphous precipitate, (c) an aggregation process intermediate between these two, yielding a gel [123]. Gelation occurs when a delicate balance between solubility and precipitation of the gelator is maintained, i.e. a balance between hydrophilicity and hydrophobicity of the gelator molecule is required. Like in the 2-D supramolecular assembly, alkyl chains [33] and hydrogen bonding [102] play a major role in gel formation; the presence of amide groups enforce fiber growth through hydrogen bonds [122, 124]. With regard to supramolecular assembly, alkyl chains play an important role and hydrophobic interactions seem to be the dominant force for gelation of amphiphilic molecules [125]. This does not imply that increasing the alkyl chain length over an optimum value enhance gelation, as longer alkyl chains could also produce 'crystallization' among themselves.

3.8. Other Resources

Also some of the resources used for this work include the molecular mechanics simulation program-*Macromodel 8.0*, molecule-building and molecular orbital (MO) plotting software-*Arguslab*, and image analysis tools such as WsXM [126], Gwyddion³ or SPIP [99]. Some of these will be discussed in more detail as and when it is encountered in the thesis. *Macromodel 8.0* is a commercial program, and has been used to understand the graphene-molecule interactions. For image analysis, mostly WsXM is used and all images presented are raw data unless otherwise specified. But often large-scale images have been flattened [126].

³ <http://gwyddion.net/features.php>

Chapter 4

Monolayer structure of Arachidic acid on HOPG

In this chapter, the adsorption of arachidic acid and its 2-D crystallization on HOPG is discussed with due emphasis on its monolayer structure, energetics, chirality and moiré effects. For brevity, the discussion on the energetics involved in the self-assembly process pertinent to arachidic-HOPG system is omitted in the respective publication [127] but shown here.

4.1. Introduction

Devices based on molecular films are more promising for the near future than those relying on technically challenging single molecule configurations [128]. Nanoscale patterning and functionalized surfaces are basic requirements for device applications. In fact, nature uses this strategy for the construction of nanocomposites through growth of inorganics at self-assembled organic templates in aqueous solutions. For example, biologically produced inorganic-organic composites such as bone, teeth, sea shells etc. are formed through template-assisted self-assembly in which self-assembled organic materials (such as proteins, lipids) acts as a scaffold for the deposition of inorganic material [129].

A monolayer is a layer of one molecule thickness assembled at an interface. The three general states of monolayers include gaseous, liquid and solid films. The possibility of forming clusters of molecules or micelles in monolayer films was first proposed by Langmuir [97]. The head/tail group interactions of amphiphilic molecules with substrates are known to be a major factor in film deposition in the Langmuir-Blodgett process. Adsorbates solvated in hydrophilic, polar solvents adsorb onto a hydrophobic adsorbent, such that the hydrophobic part of the adsorbate attach to the surface. Arachidic acid comes under the category of solid thin films, which are films exhibiting long-range translational order. In general fatty acids and alcohols exhibit this type of films. Before the advent of scanning probe techniques, studies of monolayer systems at liquid-air interface were depended on X-ray diffraction and fluorescence techniques [130]. However organic molecular species are usually fragile and electron or X-ray doses can fragment them during measurements. Moreover such techniques average over large areas and thus cannot provide information on individual atoms and molecules. STM has emerged as an ideal tool to study the 2-D crystallization process. The liquid-solid interface is a dynamical system

with constant adsorption and desorption taking place. Weak forces at the interface between an organic solution and a chemically inert substrate cause substantial molecular dynamics at the solid-liquid interface, which allow for the fabrication of virtually flawless large-area molecular layers.

Before the atoms and molecules can be engineered into devices, a number of questions have to be addressed such as the type of interactions involved, the stability and structure of assembled arrays etc. In light of this, the study of self-assembled monolayers is at the forefront of current materials research. It is also interesting and of paramount importance to know how the molecules are influenced by their interaction with the substrate. For the case of fatty acids, this is the only factor that can affect the O-O dimer distance as will be shown in the section on energetics. HOPG is used as a substrate and the affinity of alkyl chains for HOPG is well known. Does the graphite surface influence the molecule-molecule interactions? Does the dimer structure of these molecules possess the same structure as in their gas phase? These issues have not been properly addressed yet. So, instead of concentrating on series/derivatives of a particular species of molecule, the study is limited to just one simple prototype molecule, which enables a full understanding of the interplay between substrate-molecule and molecule-molecule interactions. Arachidic acid, with its hydrogen-bonding moiety and long alkyl chain, serves this purpose in the most desired fashion. Elucidating the true monolayer structure of arachidic acid, which is a physisorbed system self-assembled through hydrogen bonding functionalities and van der Waals interactions, can provide some important insights into these intriguing questions.

4.2. Arachidic Acid on HOPG

The self-assembly of arachidic acid ($C_{19}H_{39}COOH$) on highly oriented pyrolytic graphite (HOPG) is studied by scanning tunneling microscopy (STM) to identify the structure of the monomolecular film. Arachidic acid ($C_{19}H_{39}COOH$) as commercially available is dissolved in 1-phenyloctane ($C_{14}H_{22}$) to obtain a nearly saturated solution. The solution is sonicated and kept at room temperature before applying it to a freshly cleaved sample of highly oriented pyrolytic graphite.

Fig. 4.1(a) shows a typical STM image of the perfectly ordered film exhibiting sub-molecular resolution. Molecules appear flat lying and densely packed in rows (lamellae) on the surface and each molecule appears as two adjacent strands with a total of nineteen bright spots representing the protruding hydrogen atoms of the alkyl chains lying parallel to the graphite basal plane [73]. The zigzag arrangement of these spots is the result of a flat orientation of the molecules caused by a series of CH- π interactions between the C-H bond of the alkyl chain and the π electron system of the graphite carbon surface [131]. An enhanced brightness can be observed at the end of each molecule protruding into the inter-lamellar region that we attribute to hydrogen atoms of the methyl end group (see Fig. 4.2).

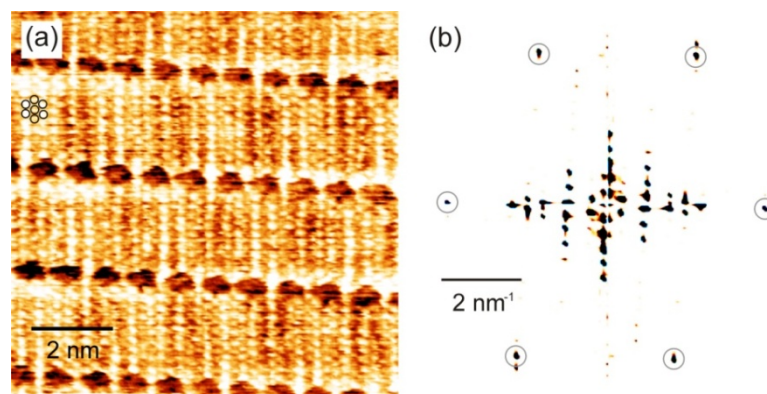


Fig. 4.1 (a) High resolution STM image of an arachidic acid monolayer on HOPG (imaging parameters $V_b = 1.3$ V and $I_t = 0.6$ nA). Bright features represent the protruding hydrogen atoms of the all-trans alkyl chains lying parallel in lamellae on the substrate. Dark regions represent carboxyl groups joined by H-bonds. The brightness modulation in the lamellae is apparent. The small circles in the upper left highlight a hexagonal arrangement of alkyl chain hydrogen atoms resulting from the assembly of two neighboring chains. (b) Fourier power spectrum of the image from frame (a). The spots of the outer hexagon marked by circles originate from the hexagonal arrangement of hydrogen atoms highlighted in frame (a).

There is an asymmetry within every molecule with one of the strands appearing brighter than the other as illustrated by the symbols introduced in Fig. 4.2. The dark regions in between the rows are interpreted as the carboxyl parts of molecules forming dimers which appear darker [132], an interpretation supported by theoretical modeling [48, 70]. Fig. 4.1(b) is the power spectrum of a Fourier transform of the image from Fig. 4.1(a). Interestingly, one observes a hexagonal arrangement of spots originating from the protruding hydrogen atoms of the molecules (see hexagon marked by small circles in Fig.4.1(a)) that closely but not perfectly resembles the periodic structure of the underlying substrate.

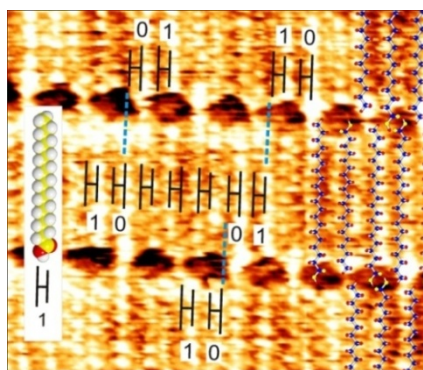


Fig. 4.2 (a) Pattern of molecular ordering in the monolayer of arachidic acid on HOPG with a superimposed prong and ball model of the molecule. The longer of the two prongs denotes the side of the molecule terminated by an O-H group.

It has been reported earlier for carboxylic acids on graphite that there is an apparent periodicity of brightness in the STM image of four or five molecules along the lamellar direction [132-135]. In Fig. 4.1(a), an increased brightness appears at every fourth and fifth molecule, however; note that the true periodicity along the lamella is ten molecules. As

highlighted in Fig. 4.2, the molecules marked “0” and “1” flip at every position of enhanced brightness, resulting in an equivalent brightness pattern only at every 10th molecule. In addition, the periodicity in brightness shifts by two molecular positions in adjacent rows, indicative of the nature of inter-lamellar hydrogen bonding present. More precisely, the left strand of the 0th molecule on the top lamella is in line with the right strand of the 0th molecule in the bottom lamella (see dashed blue line in Fig. 4.2).

As observed in the fast Fourier transform (FFT) in Fig. 4.1, there is an appearance of hexagonal symmetry in the Fourier space with no immediate hexagonal lattice visible in the real space image. To elucidate this in detail, split images obtained by changing the tunneling parameters during imaging like the one shown in Fig. 4.3(a) were taken, where both the graphite and the adsorbate monolayer appear in the same frame.

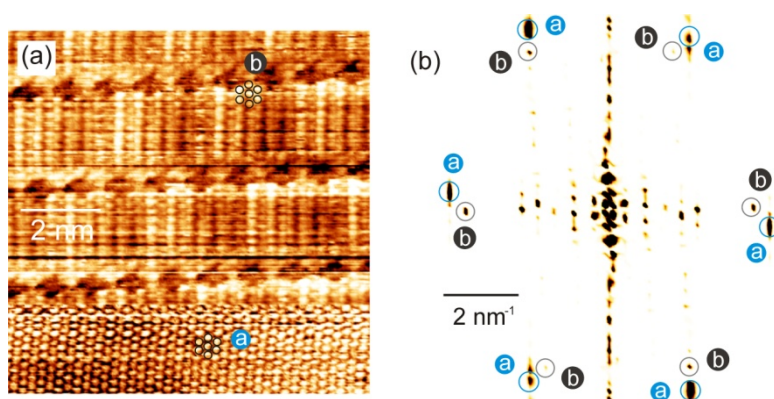


Fig. 4.3 (a) Split image showing both, the arachidic acid monolayer (upper part, $V_b = 1.01$ V and $I_t = 0.73$ nA) and the underlying substrate imaged through the molecules (lower part, $V_b = 0.05$ V and $I_t = 1.0$ nA). (b) Fourier power spectrum of the image from frame (a). The spectrum reveals two hexagonal lattices, one marked as ‘a’ arising from the graphite and the other one marked as ‘b’ from the protruding hydrogen atoms of the adsorbate layer. The apparent distortion of the hexagons is due to thermal drift.

In the corresponding Fourier spectrum, one can see two sets of spots with hexagonal symmetry, one arising from the graphite (marked ‘a’) and the other from the hydrogen atoms of the molecules (marked ‘b’). The analysis of the Fourier spots of such split images would principally allow a calibration of spots corresponding to the molecular structure against the graphite lattice but is practically difficult due to thermal drift present in the images.

The image shown in Fig. 4.4(a) is a low drift split image allowing a simple determination of the direction of the molecule with respect to the substrate. The bright spots in the graphite part represent the β carbon atoms of the graphite (0001) crystal plane as imaged by an STM [81]. The molecules are found to be aligned along the $\langle 11\bar{2}0 \rangle$ directions of graphite.

Fig. 4.4(b) is a large frame scan demonstrating that self-assembly occurs in domains oriented at 120° relative to each other with molecules following the three equivalent crystallographic directions on the graphite surface. In this image, individual molecules are hardly to be resolved but three rows of molecules are highlighted by black stripes. Blurred

contrast hiding molecular details at the domain boundaries and bright stripes in the fast scan direction points to irregular tip-molecule interaction at the domain boundaries.

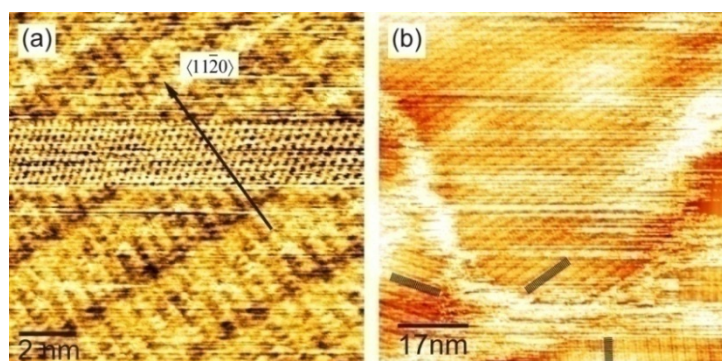


Fig. 4.4 (a) The image shows both, the molecular layer (top and bottom parts, $V_b = 1$ V, $I_t = 0.64$ nA) and the underlying substrate (middle part, $V_b = 0.05$ V, $I_t = 1$ nA). The bright spots in the graphite part represent the β carbon atoms of the graphite (0001) surface. The molecules are found to be aligned along the $\langle 11\bar{2}0 \rangle$ graphite direction. (b) Large scale image of a molecular layer exhibiting directional domains oriented at 120° relative to each other according to the three equivalent crystallographic directions on the graphite surface. Black lines drawn in stripes schematically represent molecules ordered in lamellae.

4.3. Fast Fourier Transform Analysis

In an attempt to obtain precise values for unit cell dimensions as well as intrigued by some evident symmetry features that are not immediately discernable from real-space image of Fig. 4.1(a), fourteen of the spots in the power spectrum were analyzed in detail and speculative interpretations for their origin were developed.

Spot	Fourier space angle	Distance (nm)
1	-6	0.4492
2	-6	0.9416
3	-26	0.8532
4	-26	2.120
5	0	0.3763
6	4	0.4514
7	9	0.5488
8	13	0.8354
9	27	2.070
10	75	2.277
11	83	1.342
12	86	0.6321
13	86	0.858
14	88	0.633

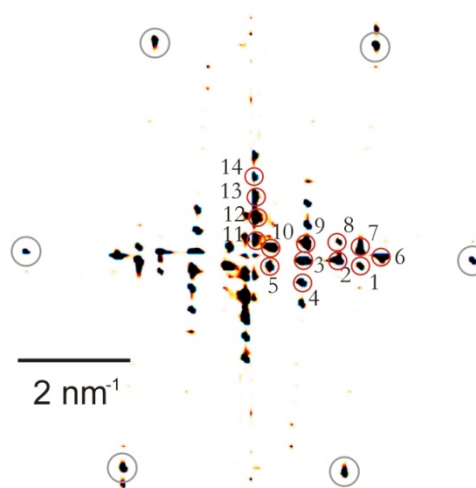


Fig. 4.5 (left) Table showing the predominant spots in the FFT power spectrum of image in Fig.4.1(a), (right) Power spectrum of the STM image in Fig.4.1(a).

However, due to the complicated internal structure of the molecular layer and the moiré effects, an unambiguous interpretation of many spots in the power spectrum is not possible. The hexagonal symmetry pattern represented by the outer spots circled in grey was unexpected as there was no graphite lattice imaged in the original image of Fig. 4.1(a). This ambiguity arises from the near-perfect lattice matching of the graphite lattice and the alkyl zig-zag chain of the molecule as shown in Fig. 4.6(a). From the discussion in the previous sections, it is clear that both the graphite and molecule lattices lie in the same direction, which is 85° with respect to the horizontal. This is illustrated in Fig. 4.6.

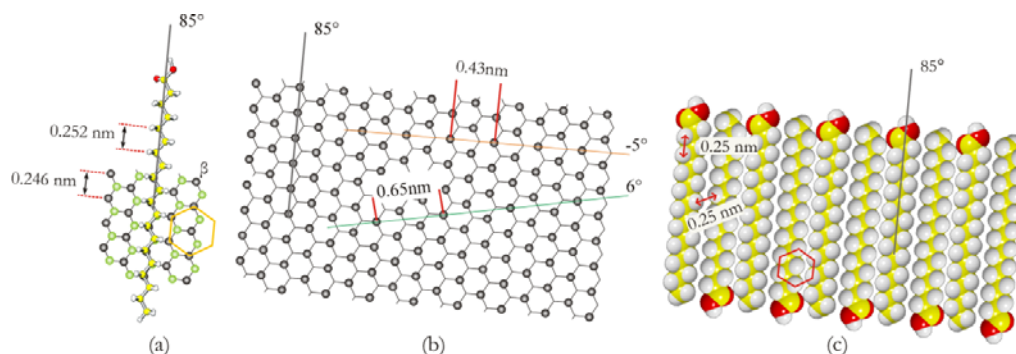


Fig. 4.6 (a) The alkyl-chain zig-zag and graphite lattice differ only by 2%. This close resemblance leads to similar symmetries (b) For the graphite lattice and (c) The lattice formed by the protruding hydrogen atoms of arachidic acid layer.

As shown in Fig. 4.6(c), the monolayer produces a near-hexagonal symmetry for its protruding hydrogen atoms. When both the monolayer and underlying graphite substrate are imaged in the same frame, one can see two sets of hexagonal spots as shown in Fig. 4.3. There are other spots in the power spectrum which can be attributed to various periodicities in the STM image; nonetheless they do not provide any unambiguous information. For example, spot 2 represents a value of 0.94 nm which is the unit cell parameter in the a direction, spot 6 has a value close to the intermolecular distance, but in both cases the directions slightly deviate from the real space measurements.

4.4. Pro-chirality of the Arachidic Acid Monolayer

The lateral interactions like hydrogen bonding between functional groups can lead to well-ordered nanopatterns with interesting chiral properties. The criterion of chirality requires sufficient complexity in a system to destroy the inverse symmetry elements. The possible packing arrangements of molecules in a 2-D plane are considerably less than in the 3-D case. The basal plane of graphite imposes restrictions on the symmetry operations of molecules which pack on it. Chirality can be induced by both the adsorption of inherently chiral molecules or achiral molecules. The latter molecules are called pro-chiral.

It is known that the fatty acids with an even number of carbon atoms are pro-chiral and exhibit different surface arrangements in contrast to those possessing an odd number of carbon atoms. The even-odd effect arises from steric hindrance caused by the

commensurate arrangement of alkyl chains on the surface. Even-numbered molecules exhibit enantiomeric separation while layers formed of odd-numbered molecules do not exhibit any chirality effect [136-138]. Unlike for 3-D crystals, physisorbed monolayers only show one orientation within a domain. STM is an ideal tool to study symmetries and chirality at the molecular level [14, 136, 137, 139, 140].

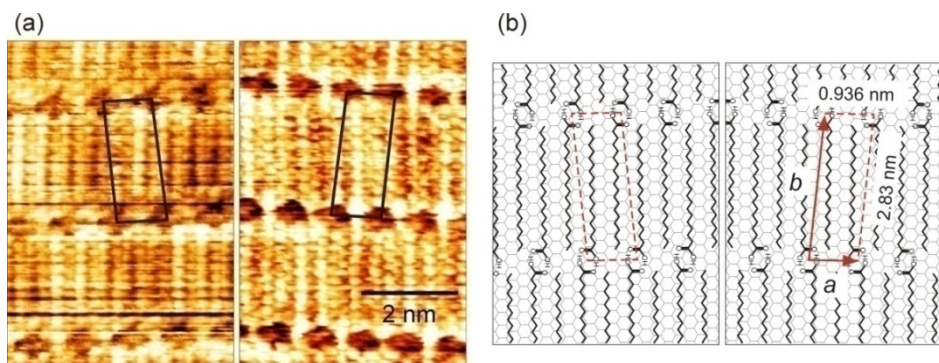


Fig. 4.7 (a) STM images demonstrating the spontaneous separation of enantiomers upon physisorption of arachidic acid on HOPG (imaging parameters for image on the left and right STM images in (a) are $V_b = 1.01$ V, $I_t = 0.73$ nA and $V_b = 1.3$ V, $I_t = 0.6$ nA respectively). Although the molecule directions are the same in both images, the oblique unit cells are the mirror images of each other. The \mathbf{b} vectors of the unit cells are tilted by an angle of 10° with respect to each other.

Arachidic acid is a pro-chiral molecule with its twenty carbon atoms, and upon physisorption, arachidic acid molecules tend to arrange in enantiomeric separated domains as shown in Fig. 4.7. The chirality in the monolayer is evident from the mirror symmetric oblique unit cells that will be discussed in detail later in this chapter. Although, the direction of the molecules is the same in both images, the unit cells are mirror images of each other and cannot be superimposed on each other by any 2D translational or rotational symmetry operation. The long sides of the unit cells are tilted by $\pm 5^\circ$ with respect to the molecular axis and, hence, enclose an angle of 10° with respect to each other.

4.5. Energetics at Arachidic Acid-HOPG Interface

Physisorbed systems are suitable model systems for investigating the properties and various interactions at play in self-assembled architectures on surfaces. In the literature, theoretical studies on physisorbed systems on solid surfaces are often scattered and do not refer to all interactions at once. Also, one can find different values for adsorption energies depending on the method used such as the *ab initio* or molecular mechanics calculations. Here, a literature survey of the predominant interactions pertinent to arachidic acid adsorption on HOPG is considered (see Fig. 4.8.). This include CH- π interaction between the alkyl chains and graphite, van der Waals interaction among alkyl chains themselves and hydrogen bonding caused by dimer formation between molecules.

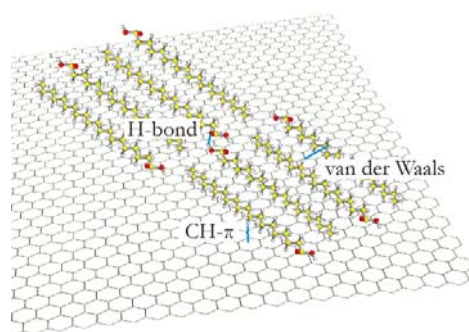


Fig. 4.8 Schematic of molecule alignment and prominent interactions at play in a physisorbed monolayer of fatty acids on HOPG

Carboxylic acid dimers are useful model systems for understanding the self-assembly process with regard to the interplay of hydrogen bonding and hydrophobic interactions in aqueous solutions [141]. Apart from these interactions, when adsorbed on solid substrates, geometric factors such as the lattice constant of the substrate can affect the molecular packing as monolayers are formed in a way to maximize the commensuration. All these forces ultimately contribute to minimize the free energy of the supramolecular arrangement.

Before proposing a model for the true molecular assembly, it is necessary to identify the energetically most favorable model from what is so far known about the relevant molecule-substrate, carboxyl-carboxyl and intra-lamellar binding energies. Here the relevant interactions are the molecule-substrate, molecule-molecule intra-lamellar and carboxyl-carboxyl inter-lamellar binding

The molecule-substrate interaction has both van der Waals and electrostatic contributions, but the electrostatic energy has been shown to be much smaller than van der Waals energy [94]. Molecular mechanics calculations for the van der Waals contribution of adsorption of long chain alkanes on graphite yield a value of $-12.1 \text{ kJ mol}^{-1}$ per CH_2 [94]. *Ab-initio* calculations for isolated polyethylene chains adsorbed on graphite yield an adsorption energy of $-11.55 \text{ kJ mol}^{-1}$ for each C_2H_4 unit [70] which is approximately half of the value from molecular mechanics calculations. The alkyl chain- graphite interaction is analogous to the so called $\text{CH}-\pi$ interaction between benzene-methane system [86] with a strength in between the weakest class of hydrogen bonds and van der Waals, here each $\text{CH}-\pi$ interaction contributes about $-4.18 \text{ kJ mol}^{-1}$ to the adsorption energy[86]. Values from the last two are comparable, so it is reasonable to take the value of $-5.77 \text{ kJ mol}^{-1}$ per CH_2 ($=11.55/2$) for adsorption on graphite. So, for a dimer with 38 CH_2 groups, this amounts to 220 kJ mol^{-1} . For all models in table 4.1, this adsorption energy remains the same, i.e.; around -220 kJ mol^{-1} per dimer.

The molecule-molecule intra-lamellar interaction is governed by van der Waals forces. This lateral molecule-molecule interaction is the basic driving force for 2-D crystallization at the

surface. The molecular mechanics calculation [94] yields a value of -5 kJ mol^{-1} per CH_2 unit which is in reasonable agreement with the *ab-initio* calculation yielding $-9.63 \text{ kJ mol}^{-1}$ for each ethylene (C_2H_4) unit [70]. Therefore, inter-chain interaction energy amounts to $-4.81 \text{ kJ mol}^{-1}$ ($= 9.63/2$) for each CH_2 . Thus, for a dimer with 38 CH_2 groups, this is equal to 183 kJ mol^{-1} . Note that these calculations assume the Groszek model [93] for the molecular positions on the graphite. Also, it has been shown that the substrate does not perturb the molecule-molecule intra-lamellar interaction noticeably and the equilibrium inter-chain distance remains nearly the same as in vacuum [70] implying that self-assembly is largely a result of inter-chain interaction.

It is known that carboxylic acids can form dimers in media of low dielectric constant. However, despite many studies on carboxylic acid monolayers on HOPG, there have not been any reports on the accurate O-O distance for a carboxylic dimer on graphite. This leaves some uncertainty when constructing molecular arrangement models like, for example, the one reported for cis-unsaturated carboxylic acids [138]. Long before the advent of scanning probe techniques, it has been suggested purely from geometric considerations that the O-O distance for the carboxylic cyclic dimer on graphite could take a value less than 0.20 nm or greater than 0.35 nm provided both molecules on adjacent lamellae are in a 'lattice fit' arrangement as for alkanes [93] and 0.275 nm when only one of them occupies the 'lattice fit' arrangement [142]. But when molecules are embedded on graphite like in a monolayer, there can be sites where molecules in adjacent lamellae that form a dimer, are possibly out of any "lattice fit" arrangement.

Another issue here is that here measurements are done in solution environment and in general, polarity of a solvent can affect the hydrogen bond strength due to the electrostatic and charge-transferring nature of the hydrogen bond [143]. As phenyloctane is a non-polar solvent, this possibility can be neglected in our case. The only influence in the O-O distance can arise from the molecule's affinity for the substrate due to their geometric similarity. This distance can be obtained only after a suitable model is constructed pertaining to the unit cell parameters and the scenario of molecules' dispositions as seen in Fig.4.2 (a). For our estimate of the so obtained bond energy, we will compare it with the gas phase values. Both, theoretical [144] and experimental [145] gas phase values for the enthalpy of dimerization have been determined to be -60 kJ mol^{-1} and the O-O distance for optimum binding has been found to be 0.28 nm [144].

In conclusion, for a dimer with 38 CH_2 groups, the adsorption and crystallization energies are -220 kJ mol^{-1} and -183 kJ mol^{-1} respectively. For the hydrogen bonds in the monolayer, no estimate of dimerization energy is available. One cannot expect the O-O distance to be the same as in gas phase due to the substrate influence evident in the form of the commensurate packing of molecules on HOPG, and an estimate of this O-O distance becomes necessary.

4.6. Monolayer Structure of Arachidic Acid on HOPG

4.6. 1. Determination of the Intermolecular Distance from a Moiré Pattern

In order to make an accurate model of monolayer structure, the O-O distance is a prerequisite. To obtain this distance, one method is to calibrate the STM image with some known lattice constants, and then measure the distance directly from the image. This however, is not practical due to thermal drift present, and for carboxylic parts being ‘dark’ in the STM images. Another method, that is used here, is to combine an intrinsic form of calibration for the STM image to find the inter-molecular distance, and then use it to dispose molecules according to Fig. 4.2.

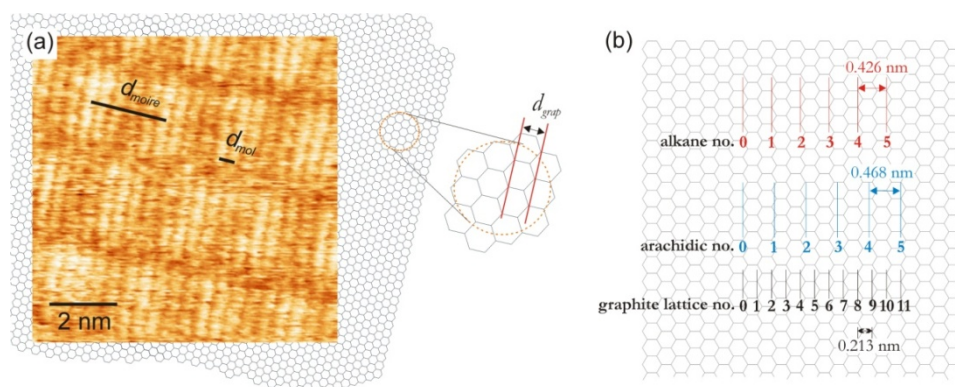


Fig. 4.9 (a) Moiré pattern apparent on an arachidic acid monolayer on HOPG exhibiting a periodicity of five molecules (imaging parameters $V_b = 0.71$ V and $I_t = 0.68$ nA). The parameters $d_{moiré}$ and d_{mol} denote the moiré periodicity and intermolecular distance, respectively (b) Comparison of simple alkane and arachidic acid molecules lay on HOPG.

A direct measurement in STM images is not a practical choice for the accuracy expected for this study, here a moiré pattern resulting from the superposition of tunneling current contributions from the substrate lattice with the molecule lattice, is used. The moiré pattern exhibits a periodicity of $n_{mol} = 5$ molecules (see Fig.4.9). From this, the intermolecular distance, d_{mol} , can be calculated as $d_{mol} = n_{graph} \times d_{graph} / n_{mol}$, where $d_{graph} = 0.213$ nm is the periodicity of the graphite atomic lattice. The number of graphite periods between moiré periodicity is assumed to be $n_{graph} = 11$. This is a plausible value as evident from Fig.4.9(b) because the periodicity would be 10 for simple alkane chains strung along the lamella, and arachidic acid molecules require only little more space due to the carboxylic end group. From this analysis, we obtain a value for the intermolecular distance of $d_{mol} = 0.468$ nm, and can adjust earlier propositions of a larger intermolecular distance that were based on a wrong assumption for the brightness modulation periodicity [132].

4.6. 2. Disposition of molecules and Monolayer Structure

With a precise value for the intermolecular distance, the molecules can be arranged as indicated by Fig.4.2, enabling to discern the true arrangement of molecules in the unit cell.

For this, relative positions of molecules in directions along as well as perpendicular to the lamellae are considered.

TABLE 4.1. Unit cell and H-bonding parameters for possible models of the arachidic acid monolayer on HOPG.

model	unit cell dimensions in nm and angle between unit cell vectors	O-O distance in nm derived from structure model
a	a= 0.936 b= 2.95 85°	0.44
b	a= 0.936 b= 2.83 85°	0.31
c	a= 0.936 b= 2.71 85°	0.20

The relative positions of molecules along lamellar direction with respect to the underlying graphite are fixed. On the other hand, perpendicular to the lamellar direction, various distances are possible, all of which give the same image contrast in the STM images. Remember that the image contrast is a result of the moiré effect from the molecular lattice with that of the graphite lattice. This gives rise to three different plausible models with three different O-O distances. This is obtained by moving one of the molecular rows by equal steps of the graphite zigzag distance of 0.123 nm, resulting in the three models 'a', 'b' and 'c' with unit cell parameters described in table 4.1.

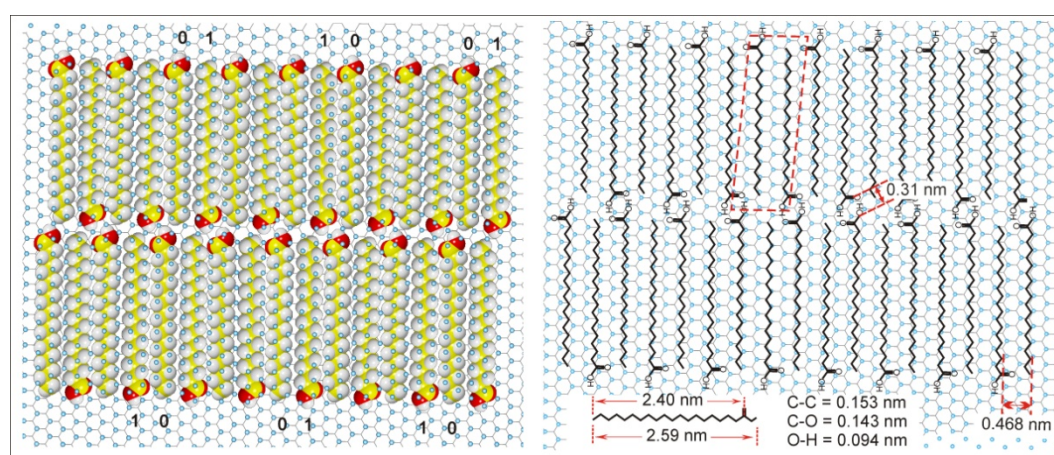


Fig. 4.10 Ball and stick models for the molecular arrangement of arachidic acid on HOPG (model 'b' in table 1) superimposed by the hexagonal grid of β carbon atoms as imaged by STM. In the carbon skeletal chains of the stick model, bond lengths are drawn to scale. The length of the molecule is determined by a construction of a model from known bond lengths and bond angles taken from literature [35, 91, 92, 142].

The true unit cell dimension $|\mathbf{b}|$ is obtained by an analysis of the respective dimension in the models and the known length of the arachidic acid molecule. The length of the arachidic acid molecule can be calculated to be 2.40 nm from the terminating carbon to the C=O bond as in Fig.4.10 from the known lengths and angles of the involved bonds [35, 91, 92, 142]. Using this value and relating the molecular length to the unit cell dimension $|\mathbf{b}|$ in the model in Fig.4.10, precisely reproduces the prediction from model 'b' that is $|\mathbf{b}| = 2.83$ nm.

The choice of model 'b' as the true molecular assembly structure is further supported by considering the carboxyl-carboxyl inter-lamellar hydrogen bonding as discussed before in the energetics section. Model 'b' assuming an O-O bond distance of 0.31 nm is the energetically most favorable one because this value is closest to the gas phase value. Note that this is an unrelaxed value resulting from purely geometric considerations. The actual O-O bond distance might be slightly different due to molecular relaxation, possibly yielding an energetically more favorable configuration.

At this point, we can define all dimensions of the oblique unit cell of the molecular structure from model 'b' as $|\mathbf{a}| = 0.94$ nm and $|\mathbf{b}| = 2.83$ nm where the angle between unit cell vectors \mathbf{a} and \mathbf{b} is 85° . The unit cell accommodates two molecules and is tilted by 5° with respect to the molecular axis. Note, that this is the unit cell of the molecular structure but not the unit cell of the STM image that is influenced by moiré effects. A close inspection of the STM image reveals variations in apparent contrast between nominally equivalent molecules that imply a much larger unit cell than determined above. This is also reflected in the Fourier spectra in Figs. 4.1 and 4.3, where the dimensions of the structural unit cell are not clearly represented as dominating spots.

4.7. Conclusion

Arachidic acid, being a pro-chiral molecule, crystallizes into enantio-pure molecular domains having unit cells that are tilted by 10° with respect to each other. The deviation of the registry between alkyl chains and the graphite lattice results in peculiar contrast features in STM imaging in the form of an asymmetric appearance of the molecules, periodic contrast enhancement, and a characteristic moiré pattern observed under certain experimental conditions. Using methods of internal calibration of the STM images with respect to the graphite surface atomic structure, an oblique monolayer unit cell (85° angle) with dimensions of 0.936 nm \times 2.83 nm has been unambiguously determined, allowing for a favorable, unrelaxed O-O distance of 0.31 nm for hydrogen bonding between carboxylic dimers.

Chapter 5

Differentiating Low-Dimensional Organic Structures from Innate Graphene Manifolds

This chapter describes the intricacies of using HOPG as a substrate for STM imaging of organic adsorbates. It is divided into two parts: the first part comprises a discussion of 1-D and 2-D innate structures present on HOPG surface, and the second part on how to differentiate them from adsorbates. This chapter mainly involves measurements on bare HOPG sample, and a few cases of graphitic structures observed with molecules on HOPG. Also, evidence for moiré rotation as a cause for graphite superlattices is derived. In the context of differentiating adsorbate structures, the 1-D case will be given more emphasis in view of its closer connection to the studies on organic nanofibers that is discussed in chapter 6. The presence of defects in graphene modifies its physical and chemical properties; therefore, this study may have implications also in the fundamental areas of research on graphene-based devices [146-148]. A mechanism is proposed on the creation of innate graphite fibers from asymmetric graphite flakes created at step edges.

5.1. HOPG as a Substrate for STM Studies

Scanning probe microscopy offers a unique advantage over other surface techniques in studying surfaces and adsorbates due to its ability for real space imaging. Scanning probe techniques has also proved its versatility as an alternative method for fabrication of graphene devices [149]. For STM studies of adsorbates, suitable substrates need to be chosen that do not mask the molecule-molecule interactions. Therefore metals or graphite are usually used. Although graphite offers many advantages as a substrate, the presence of 1-D and 2-D structures seen on bare HOPG complicates the understanding of adsorbate structures on HOPG.

The feasibility of HOPG as a substrate for STM studies has been questioned as early as 1991 in the context of DNA or biomolecules [150] albeit with no much follow-up in this direction. Graphite, due to its chemical inertness and large atomically flat planes, remained a favorite ever since its first use as a sample in STM studies in ambient conditions [151]. There were many reports on the anomalous features observed on HOPG when imaged by STM, such as enormous height of atoms above the centers of carbon rings and asymmetry of neighboring carbon atoms [81, 151-154] [155]. It is known that, as far as the STM imaging of bare HOPG surface is concerned, there have always been many intriguing

aspects such as the inability to observe all atoms of the (0001) surface, superperiodicities and fiber-like structures. The observation of only the β carbon atoms has been attributed to the electronic effects arising from the asymmetry induced by AB stacking of graphene layers (discussed in chapter 3), resulting in a suppression of charge density at the Fermi level at α sites [81]. However it was shown later, that although this is true at low bias voltages, the α and β sites could be selectively imaged at voltages > 0.5 V by changing the bias polarity [156]. Considering the then accepted picture of mechanical interaction, it has been claimed that at higher bias voltages, the tip-sample mechanical interaction is absent and only then the true electronic structure of the sample could be obtained. The anomalously large corrugation amplitude for the superlattice has not been well understood, and could not be attributed to surface morphology and density of states. This, rather, could be due to tip-sample mechanical interaction as reasoned by Kuwabara et al. [157]. While considering the imaging mechanism of monatomic steps on graphite, Atamny et al. showed that the investigation of graphite steps by STM is impossible without modifying them, and thus underlining the influence of mechanical tip-sample interactions on the STM imaging of HOPG [22]. However, the mechanical tip-interaction model in STM imaging was later ruled out [154],[158]. Although different from a context discussed here, the interaction of hydrogen with graphite surface has been found to induce long-range electronic effects on graphite [159]. STM imaging of a graphite surface with or without adsorbates have always been intriguing and to some extent controversial [22-24].

5.2. Innate Graphite Low-Dimensional Structures

Carbon is polymorphic. The diversity of materials that carbon can form is related to the ability of s and p orbitals to hybridize into sp, sp² and sp³. Classically the hybridization was thought to relate to the dimensionality of the material but with the discovery of new forms of solid state carbon, the understanding in this view has evolved. Solid state carbon has been known to appear in five basic forms: diamond (sp³), graphite (sp²), non-crystalline structures such as charcoal, fullerenes, molecules such as C-60, carbon nanotubes discovered in 1991 [160] and recent fabrication of isolated graphene layers [161] [162] [163]. Graphene, which is a monolayer of graphite, is the thinnest known material and the strongest ever measured [164] [165, 166]. Graphene has immense potential for applications [167] [168]. Nanographenes, which are extended polycyclic aromatic hydrocarbons, are promising for future electronics [169]. The high charge carrier mobility makes graphene ideal for integrated electronic circuitries, and with its planar geometry can be integrated rather straightforwardly into the current silicon technology. So, study of native graphite structures- all of which are, in one way or the other essentially of graphene origin, can provide more insight into graphene research.

Graphite consists of graphene sheets arranged in an AB stacked fashion. The two-dimensional graphene sheet can be distorted in the third dimension with relatively low energy to form a very rich family of structures without changing the in-plane bond lengths. Further, here the experiments are done in ambient conditions and it is known that

nanofabrication of most layered materials can occur more easily in air with the presence of water vapor than in UHV [170], and the formation of nanotubes has been reported to improve in the presence of small quantities of water [171]. Applying a voltage pulse to improve resolution is a usual method employed in scanning probe techniques; however, with adsorbates present, it may initiate processes like clustering of molecules [172]. Graphitic structures are weakly bound and can be manipulated easily [21]. H. Hiura showed that bias voltages above 3.1 V can be used to tailor graphite surface and at voltages as high as 3.19 V, a groove of 0.35 nm depth could be created, which means that such high voltages could affect only up to the topmost layer [173, 174]. So, in normal STM operation, the possibility of any dramatic modification of graphite layers by the electric field can be ruled out and innate graphite low-dimensional structures could be originating as a result of cleavage process.

The native low-dimensional structures found on the bare graphite surface can be broadly classified into two: planar and fibrous structures. They are basically of graphene origin, which means that these features are a result of bending, folding (1-D structures) or rotation of graphene sheets (2-D structures).

5.2.1. Planar (2-D) Graphite Structures

The rotation of two lattices of the same symmetry and lattice constants results in a moiré pattern. The symmetry of the resulting lattice reflects that of the original lattices but the periodicity depends on the angle between the two participating lattices. The periodicity D of moiré pattern is given by

$$D = \frac{d}{2 \sin\left(\frac{\theta}{2}\right)} \quad (5.1)$$

Here θ represents the rotational angle and d is the lattice constant, which is 0.246 nm for the graphite lattice. Once θ is found, the orientation Φ of the moiré pattern with that of underlying atomic lattice can be found from

$$\Phi = 30^\circ - \theta / 2 \quad (5.2)$$

Graphite with its weak inter-layer interaction is amenable to deformations resulting in the modification of its electronic structure. The superlattices seen on HOPG usually exhibits hexagonal symmetry [175] [157], and the consensus on their origin is due to moiré rotation effects [157], [20, 176]. The observed superlattice periodicities, corrugation amplitudes, dependence on bias voltages etc. were summarized in a recent review by Pong [177]. With a fortuitous observation of tearing and folding back of the top layer by STM tip, Beyer *et al.* showed that the superperiodicity is caused by a rotation of the top layer with respect to the underlying crystal, by measuring the angle Φ from the STM image [20]. Observing spatially changing superlattice periodicity had recently been reported which was attributed to the shear strain causing spatially-varying rotation of the layers [178]. Although the described work supports the moiré hypothesis, there are also arguments against a simple

moiré theory, mostly based on experimental measurements on angle Φ in disagreement with angles calculated from Eqn.(5.2) [179, 180].

The rotation of the topmost layer giving rise to anomalous periodicities on the bare HOPG surface could be induced by various reasons. Cleavage using an adhesive tape can induce a rotation, the impact of the STM tip can tear the graphitic layers [181] or other factors such as intercalation. Intercalates are foreign species in the inter-planar interstitial sites of a graphite crystal with the layer structure retained. The intercalation of molecules from a solution into interlayer spacing can cause the topmost layer to slide. Since pure graphite is a semimetal, the graphite bonds can gain or lose electrons to intercalate by ionic bonding. Daulan et al observed moiré pattern on HOPG when graphite was electrochemically intercalated with FeCl_4^- in CH_3NO_2 solution [180]. Although those images look very similar to the usual superperiodicity structures reported on HOPG, they attributed it to the charge density waves resulting from a charge transfer between the intercalate and the graphite. The main reasoning for discarding it as a moiré pattern, again, was the disagreement on angle Φ calculated from Eqn.(5.2). It has been reported that moiré patterns could be produced purposefully albeit with no control on their periodicity, by immersing HOPG in organic solvents like dichloroethane, whereas dry-prepared HOPG samples seldom displayed moiré patterns [158]. In any case, from the above discussion, it is evident that the presence of an organic solution can increase the number of such superlattices on HOPG [23, 158].

Planar Graphite Structures with Organic Solution on HOPG

Three different cases of graphite superlattices, observed in the presence of dilute organic solutions on HOPG, are reported below. Remember that the presence of an organic solution may facilitate layer rotation. Fig. 5.1 shows a superlattice structure observed with arachidic acid on HOPG. This is shown here simply for illustrating how the layer rotation leads to superlattice periodicities. The second example (Fig. 5.2) is a graphite superlattice observed with the 3CH-12 solution on HOPG. The third example in Fig. 5.5 was observed with 3CB-8 on HOPG and can provide evidence for the moiré rotation hypothesis.

Example 1

Graphite superlattices represent planar structures that have a much larger periodicity than the normal graphite(0001) surface. Fig. 5.1 shows an STM image of such a superlattice but also with the underlying graphite lattice. This STM image was taken with a solution of arachidic acid on HOPG. The shorter lattice seen in the image has the lattice constant of graphite. The measured moiré periodicity is $D= 1.41 \pm 0.04$ nm. With D known, using Eqn.(5.2), one can obtain the rotational angle θ and the angle the moiré pattern makes with the graphite lattice Φ . Using a value of $D= 1.45$ nm gives $\Phi= 25^\circ$ which is slightly

different from the directly measured angle in the STM image. This discrepancy probably could be resulting from thermal drift present in the STM image.

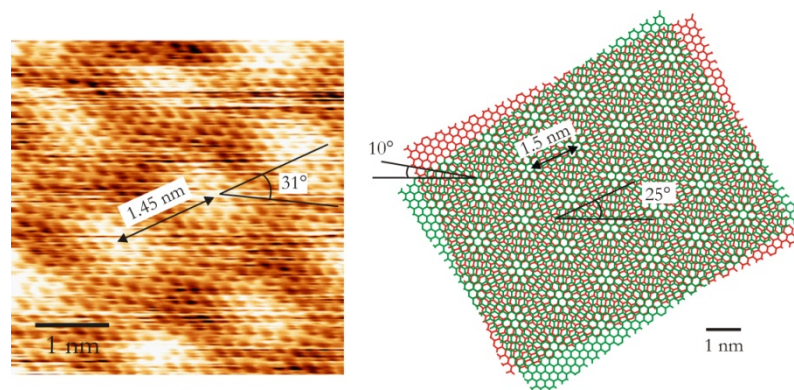


Fig. 5.1 (Left) STM image showing both the superlattice and the underlying graphite (0001) surface in a single frame. The shorter lattice structure is bare HOPG surface. The image was obtained at arachidic acid/HOPG interface (imaging parameters 0.34 V, 0.87 nA). (Right) The observed periodicity can be explained by a graphite moiré effect arising from the rotation of topmost graphene layer. The discrepancies in the values results from the thermal drift present in the STM image.

Thus the moiré rotation of two topmost graphite layers can provides reasonably good agreement between calculation and measurements. However, the width of the rows here is ~ 2 nm which is close to the length of 2.7 nm of the stretched arachidic molecule. Recall the image in Fig.4.9 discussed in chapter 4, which is a moiré pattern of arachidic acid with that of graphite lattice. Both images look similar except that in Fig. 5.1, the graphite lattice can be explicitly seen and the tunneling parameters are slightly different for the two images. But in both cases, the voltage and current are intermediate and are neither typical for imaging molecules nor the graphite lattice. One can, therefore, equally well argue that Fig. 5.1 shows a moiré pattern of the molecule with that of graphite. Here, however luckily the width of the rows is not perfectly in agreement with the length of the arachidic acid molecules and therefore one can exclude molecule contribution and attribute it to graphite. As discussed before, the moiré hypothesis has been questioned and needs to be supported by more experimental evidence. In an attempt in this direction, with the help of STM images exhibiting a rare fortuitous change of moiré periodicity in real time, it will be shown that moiré patterns are indeed a result of layer rotation. The superlattice changes its periodicity during scanning and the changes in periodicity as well as directions of the superlattice have a one-to-one agreement with moiré equations (5.1) and (5.2).

Example 2

The occurrence of perfectly circular bright lobes with a hexagonal unit cell and periodicity 3.2 nm could cause some confusion about the origin of it. This particular image is suspected to be a graphite moiré pattern caused by a rotation of the top graphene by 4.4° as illustrated in Fig. 5.2.

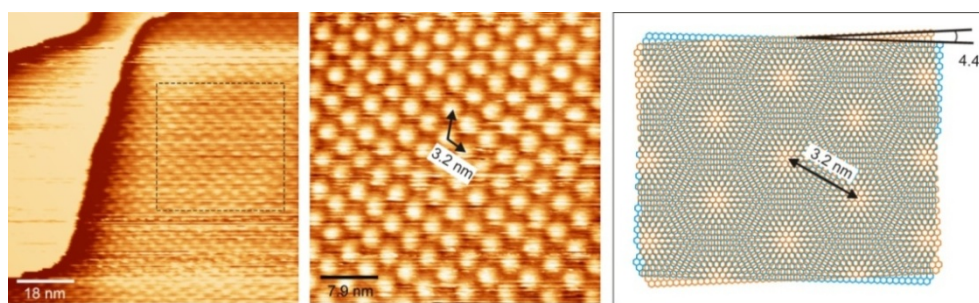


Fig. 5.2 Graphite superlattice observed with 3CH-12 on HOPG. The layer has hexagonal symmetry with a periodicity of 3.2 nm. (Right) Formation of the observed pattern from a moiré rotation of 4.4° between graphene layers.

Example 3- Evidence for Moiré Rotation

As discussed in the previous sections, the superlattice periodicities reported in literature vary from a few to several tens of nanometers [177]. However there has been no report on observing a change in the periodicity of a particular superlattice by itself or due to any internal or external stimulus. If such a change happened, it could possibly serve as a verification of the moiré hypothesis. Here a fortuitous instance where the STM tip movement causing the rotation of a graphene layer on HOPG is reported.

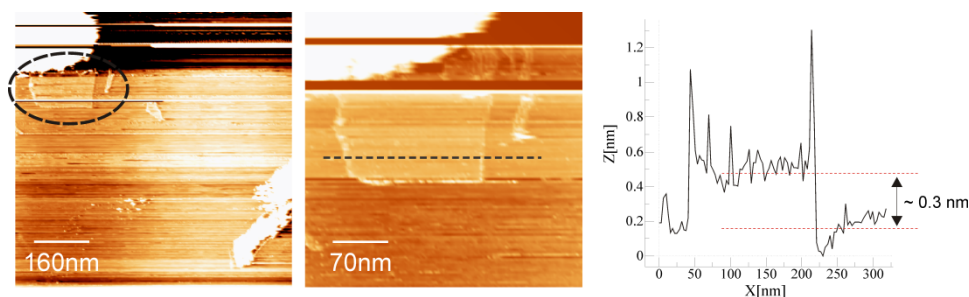


Fig. 5.3 STM image showing a graphite flake presumably created during cleavage and the corresponding line profile. The flake is one layer thickness representing a single graphene sheet.

Fig. 5.3 shows STM images taken after a drop of a dilute solution (0.028 wt.-%) of 3CB-8 was deposited on HOPG. The molecule is known to exhibit gel nature in solution [101, 182] but the image here apparently exhibits a layer structure. However, detailed analysis shows that this is indeed a graphite superlattice formed from the rotation of a graphite flake on the surface. What is interesting and helpful in establishing its origin was a change in the superlattice structure observed during scanning. Here, as in the line profile in Fig. 5.3, the concerned area is approximately one layer high (interlayer separation of graphite is 0.34 nm) which could be a graphite flake produced during the cleavage process. Due to the presence of the liquid, during scanning, this flake got easily moved off by the tip. Fig. 5.4 shows a part of the region within the ellipse in Fig. 5.3. The damage caused by the tip can be clearly seen in the lower left part of the rectangular area in Fig. 5.4(b).

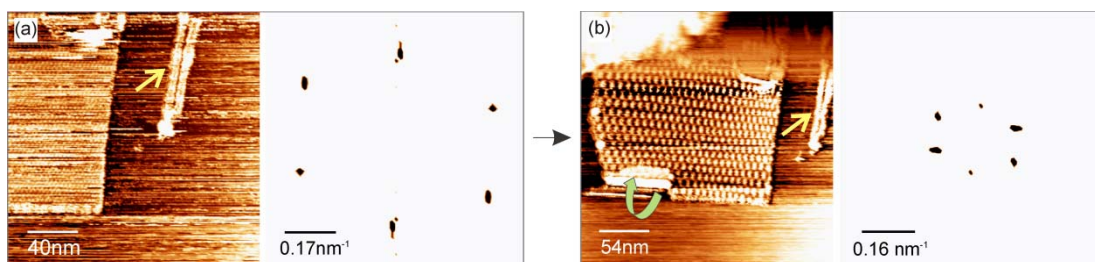


Fig. 5.4 Change in the superperiodicity of graphite surface observed during a study of 3CB-8 on HOPG. The width of one of the fibers (~ 8 nm) indicated by arrows remains the same in both images excluding any artifacts or tip effects. (a) Periodicity of 3.2 nm (b) Periodicity changed to 7.6 nm. The FFT's of the region containing superperiodicities are also shown for both images which show hexagonal symmetry in each case.

Next to the graphene flake, a fiber of 3CB-8 molecules was formed. The width of the fiber (~ 8 nm) indicated by the yellow arrow remains the same in both images. Thus the change in the shape and periodicity does neither represent a molecular feature or any image artifacts nor change in the tip conditions. The initial and final structures show hexagonal symmetry which is evident from the respective FFT's. The change in the superlattice structure was caused by the STM tip while making a change of the scanning area from large-to-small-to-large. During this process, the STM tip motion in Y-direction caused a small rotation of the layer, the effect most easily visible as a damage in image of Fig. 5.4(b) indicated by the green arrow. Because the damage is limited to a region on the lower left part of the rectangular region, the tip has presumably rotated the layer rather than moving it as a whole in Y-direction.

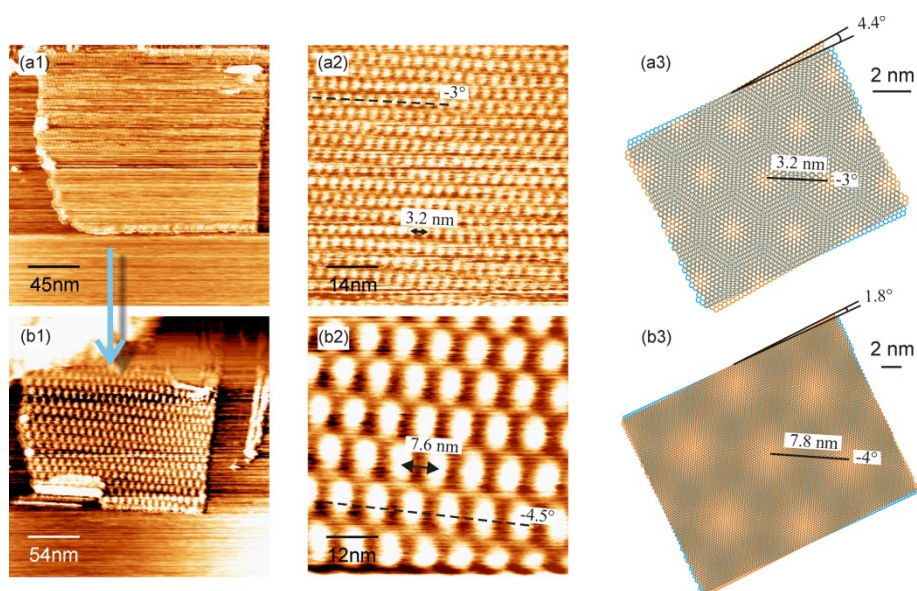


Fig. 5.5 (a1) Same region as highlighted in the ellipse in Fig. 5.3. Imaging parameters are 0.19 V, 0.6 nA. (b1) After a rotation of the top graphene layer caused by the STM tip. Imaging parameters are 0.08 V and 0.6 nA. The change in the magnitude and directions of periodicities imply moiré rotation as the cause for hexagonal structures in (a1) and (b1).

In Fig. 5.5, the drawing shown is a graphite lattice with a carbon-carbon distance of 0.142 nm, which means that they are not the β atoms unlike the one used in some reports in literature. This is because once there is a rotation; the concept of β atoms is obsolete. Fig. 5.5 presents evidence in support of a layer rotation as the origin of the superperlattices observed on HOPG. Usually the superperiodic structures remain stable for long unless one can deliberately rotate the top layer by some means. Here, a rotation induced by the STM tip resulted in a change of the periodicity of the superlattice.

The periodicity of the hexagonal structure in Fig. 5.5(a) is 3.2 nm. Now, assuming that the layer structures are caused by moiré rotation and using the value of D_1 in Eqn.(5.1), the rotational angle θ_1 can be found to be 4.4° . Similarly for the modified superlattice in Fig. 5.5(b1), $D_2 = 7.6$ nm and $\theta_2 = 1.8^\circ$. This shows that the top graphene layer is rotated in the clockwise direction which is in agreement with the direction of force that presumably caused the damage to the layer. In order to verify the assumption that the structures are actually a result of a moiré rotation, in Fig. 5.5(a3), the periodicity direction is made to lie along the same direction as in Fig. 5.5(a2) which is -3° . Now, one can see that after a rotation of 2.6° of the top graphene layer in the clockwise direction, a new larger periodicity resulted in the drawing in Fig. 5.5(b3). This periodicity is 7.8 nm with a direction of -4° . If the assumption of a moiré rotation is right, one should see a similar change in the direction of periodicity for the STM image as well. In the image of Fig. 5.5(b2), the direction is -4.5° . So, this shows an almost perfect match between the angles calculated for the moiré rotation. The small deviation is probably caused by thermal drift in the STM images. This is the first measurements of such a kind directly giving a verification of the moiré hypothesis.

5.2.2. Fibrous (1-D) Graphite Structures

Before discussing fibrous structures which are curved geometries formed from planar graphene sheets, it is essential to look at the feasible geometrical distortion directions of a graphene sheet.

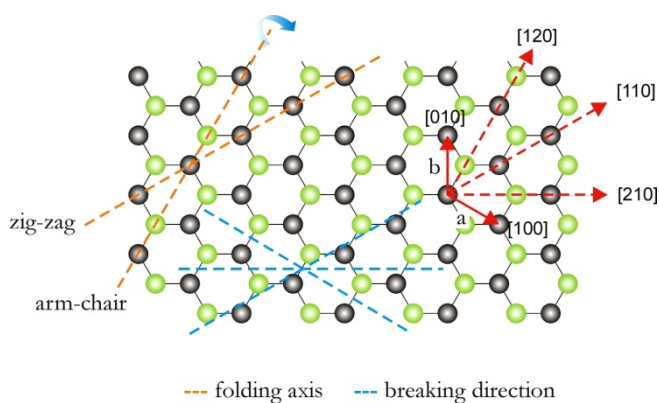


Fig. 5.6 The directions and axes favorable for breaking (tearing) and folding of the graphene layer. Folding axes are so chosen not to disturb the hexagonal structure and always pass through atom positions while the breaking directions pass through bonds.

Tearing and folding of graphene layers while cleaving graphite using adhesive tape has been reported previously [20]. There are some energetically favorable directions for folding and breaking of graphene flakes [21, 183]. The breaking (tearing) always should take place between two bonded atoms and therefore the favorable directions are as shown in Fig. 5.6. For folding, the axis should go through two carbon atoms rather than through a C-C bond. Further, for folding it is also assumed that the hexagonal structure is not disturbed and therefore the plausible folding axes are shown in the image. All directions differing 60° from each folding/breaking direction are equivalent. In general, folding and breaking take place at angles in multiples of 30° with the main crystallographic axes.

Bare HOPG Structures

One example illustrating the above process is discussed. Fig. 5.7 shows an STM image of a bare HOPG surface taken immediately after cleaving. The structures seen are the graphene layer torn apart into many tiny pieces and part of each folded and rolled over to become partially rod-shaped. Here, the bright triangular features are unidirectional indicative of a common force behind their creation which could be the shear force applied during cleavage.

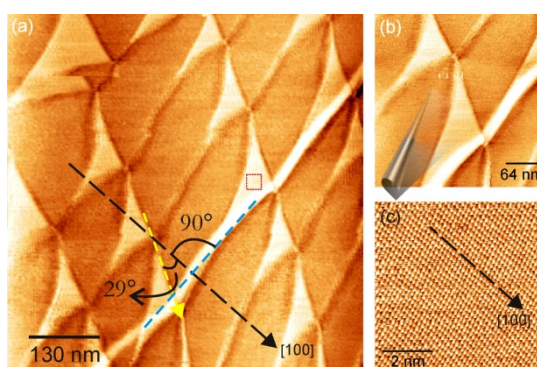


Fig. 5.7 (a) STM image of a freshly cleaved HOPG (0001) surface. The pattern is presumably formed during cleavage, first having torn or broken in the direction indicated by yellow dashed lines and then part of the torn sheets folded around an axis of dashed blue line. (b) A small region imaged within the image of (a). (c) Region highlighted within the red rectangle in the image (a). This shows a normal graphite lattice with no superperiodicity. Comparing the breaking (yellow line) and folding (blue line) directions with one of the graphite crystallographic axis (dashed black line) shows that breaking and folding take place in accordance with Fig. 5.6.

The shear force applied during cleaving presumably was not along one of the main crystallographic directions (or in any direction deviating by multiples of 30° from them), thus creating an energetically less favorable situation for a uniform exfoliation of the layer. For exfoliation to occur, the shear force applied should exceed the static interlayer shear force [146]. The occurrence of such a periodic pattern might have been caused by a non-uniform pulling effect on the surface. The atomic resolution image of HOPG in Fig. 5.7(c) is taken at the region indicated by the red rectangle in Fig. 5.7(a) and does not show any superlattice. The height of the triangular bright regions is ~ 0.25 nm and the height of the

folded fibrous part is ~ 0.4 nm. The bright rod-like regions observed near step edges (will be discussed in later sections) or at places where tearing occurs, interestingly always show heights of ~ 0.4 - 0.6 nm. It seems that the free edges of graphene layers have a tendency to roll into rather curved geometries, and this protrusion gives them a bright appearance. The brightness may also be due to a change of hybridization of graphite from sp^2 to sp^3 occurring as a result of the bending of graphene sheets [21].

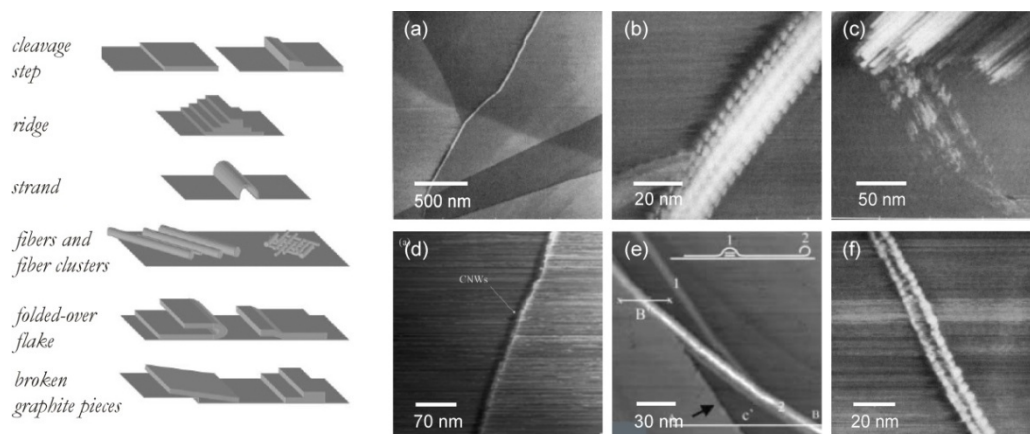


Fig. 5.8 (left) Schematic of different structures formed on HOPG (adopted from [177]) which in turn was based on [23]). Images (a), (b), (c) and (f) taken from [23], image (d) from [24] and (e) from [22]. (Right) (a-e) STM images of bare graphite structures. (a,b) strands, (c) fiber bundles, (d,e) folded layer, (f) a fibrous structure seen on HOPG in the presence of an organic solution, the structure is believed to be of graphite origin.

The bare HOPG surface also shows a variety of 1-D structures. Being polycrystalline in nature, HOPG is composed of misoriented grains of micrometer size. Upon cleavage, the surface comprises atomically flat terraces ranging in size from a few hundred nanometers to tens of micrometers. The surface also contains various defects such as cleavage steps, graphite strands, ridges, fibers, fiber bundles, folded-over flakes, broken graphite pieces and broken carbon particles [21-24], and such graphite defects have been confused with DNA strands [184].

The classification into different structures according to Fig. 5.8 is not always strictly possible due to the coexistence of many structures in the same place, and there are structures which cannot be categorized under any of these. For this reason, the origin of some structures remains unexplained. For instance how the fibers or fiber bundles are formed on bare HOPG surface has not been explained. It should be mentioned that in the experiments here, the HOPG samples used are brand new. This means that it had never been used before for depositing molecules. This is important to avoid intercalation effects or other reactive effects resulting from previous exposure to solutions.

AFM images of bare HOPG surface also reveals the presence of fibrous structures on bare HOPG. The fibrous structures in Fig. 5.9 always appear to have a larger width to height ratio, although a common numerical value for this could not be found.

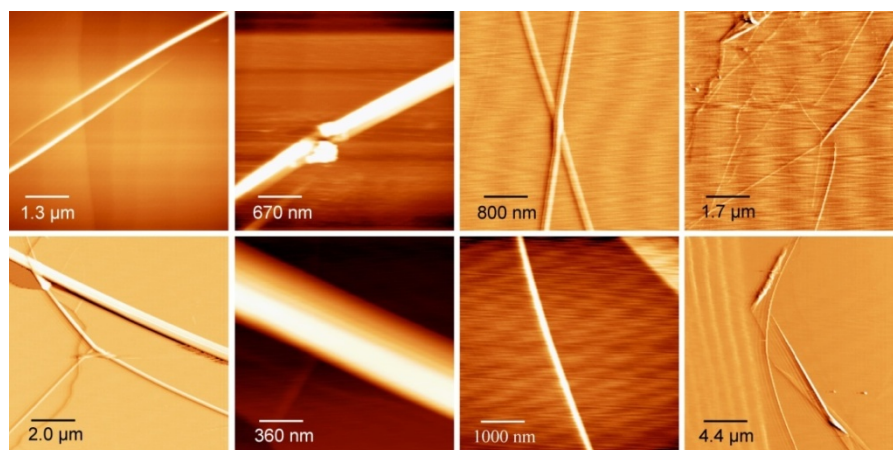


Fig. 5.9 AFM images of bare HOPG surface. All samples were freshly cleaved and never before used for depositing molecules. The widths of these fibers are always observed to be much larger than heights.

In these experiments and from data available in literature, the most common 1-D defects seen on bare graphite surface are fibers, strands/wrinkles and fiber-like features appearing at step edges.

HOPG with Molecules

Some organic fibers formed on HOPG from the wedge shaped amphiphilic molecules investigated in this thesis work are shown in Fig. 5.10. They have a startling resemblance with bare graphite structures of Fig. 5.8.

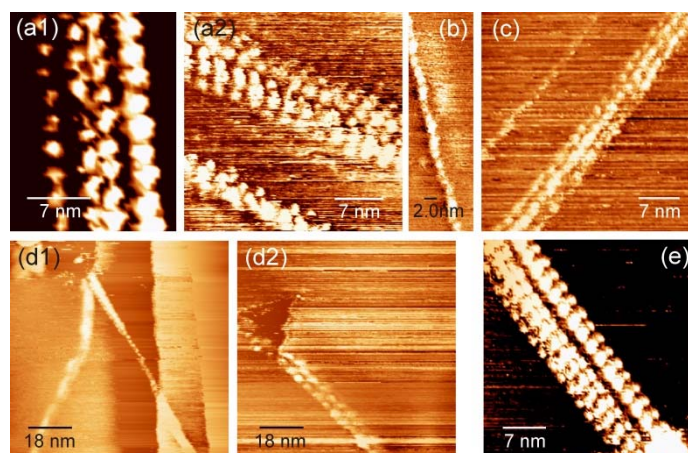


Fig. 5.10 Some of the high resolution STM images of 1-D structures after some wedge-shaped liquid crystalline molecules are deposited on HOPG. (a1) and (a2) 3CB-8. (b) 3CB-10. (c) 1CH-10. (d1) and (d2) 2CH-10. (e) 2CB'-10.

So far, innate graphite structures observed on bare HOPG surface have been discussed. In the following section, some methods will be devised to differentiate them from adsorbate structures, with planar and linear structures considered separately.

5.3. Differentiating Adsorbates from Innate Graphene Manifolds

The objective here is to unambiguously interpret the organic adsorbate low-dimensional structures on HOPG (that will be discussed in chapter 6) and differentiate them from those of native graphite ones. Difficulties arise due to the close resemblance of graphite/graphene innate structures with molecular layers/fibers, and differentiating between the two is inevitably a prerequisite for a proper interpretation of molecular structures on HOPG. Differentiating graphene low-dimensional structures from organic adsorbates is a most important task as the interest in HOPG as a substrate for STM studies is ever increasing. The interpretation is affected both at small scan areas involving sub-molecular details as well as at large scans.

5.3.1. Differentiating Adsorbate Layers from Graphite Planar Structures

In the 2-D case of forming molecular layer structures, most often one is lead to the immediate conclusion that very periodic and highly ordered structures observed could result only from adsorbates deposited on HOPG, and not from the substrate itself. This, however, can be misleading at least on few occasions. While some studies have been reported pointing to difficulties associated with innate 1-D graphite structures mimicking adsorbates as discussed previously, the 2-D graphite super lattice discussion has been limited entirely to within the bare HOPG regime. Here is one example from literature exemplifying the need to be wary of in the 2-D case.

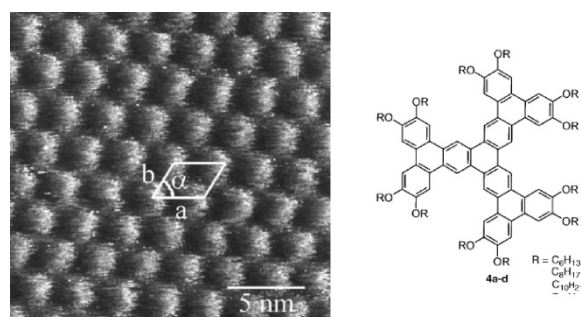


Fig. 5.11 (Taken from [185]). STM image of a monolayer of the a triphenylene derivative (shown in the right panel) at 1,2,4-trichlorobenzene-HOPG interface. It has a hexagonal symmetry with a periodicity of ~ 3.3 nm which is identical to the periodicity and symmetry of image (a2) in Fig. 5.5.

The STM image in Fig. 5.11 taken from literature was reported to be of adsorbate origin, as it was observed with a solution of a triphenylene derivative dissolved in 1,2,4-trichlorobenzene on HOPG [185]. However, it can easily be seen that this structure is identical to the image in Fig. 5.5(a2). Therefore, one could equally well argue that this indeed is a graphite moiré structure and does not represent the adsorbate layer.

As already noted, the presence of an organic solution may lead to an increase in the number of superlattices on HOPG [158]. Compared to 1-D innate graphite manifolds, planar graphene structures are usually limited simply to their superlattice appearance. The

following suggestions are put forward to straightforwardly distinguish graphite superlattices from molecular adsorbates: (i) It is known that graphite lattice influence molecular ordering [186], and therefore by imaging at large areas, one can look for domain structures which are usually showed only by molecular layers. These domains are usually oriented at 120° to each other. On the other hand, one cannot expect graphite moiré patterns to show such domain structure. (ii) Zooming in to a smaller scan range of the layer structure to get higher resolution. Unlike organic adsorbates, graphite superlattices do not show further details on ‘zooming in’ except on occasions showing the underlying graphite lattice, depending on the tip condition and voltage (as in Fig. 5.1). The organic adsorbates may show further subtle details such as individual molecules or alkyl/aromatic parts getting resolved. (iii) A large number of measurements to make sure that the same periodicity is indeed repeatedly obtained. If it is molecular structure, one should get the same periodicity for all measurements while for graphite; chances are that superperiodicity could change from place to place and from measurement to measurement or observe no superlattice at all. (iv) The symmetry of graphite superlattice should always be hexagonal as expected from the assumption of moiré rotation.

5.3.2. Differentiating Adsorbate Fibers from Fibrous Graphene structures

The simple methods/suggestions proposed here will help to save time and properly assign the origin of the 1-D structures on HOPG to graphitic or an adsorbate. Unlike their planar counterparts, the 1-D innate graphite structures are varied and shows close resemblance to fibers formed from organic molecules containing alkyl and aromatic parts. There is no single-step differentiating factor but one has to incorporate one or many of these methods pertinent to each specific case.

1. Fibers with Well-Defined Periodicity- arrangement of bright blobs

Owing to experimental difficulties, elucidating inner structural details of isolated, one-dimensional organic structures using STM has not been tried very often. But in this thesis work, studies are concentrated on scales down to atomic/sub-molecular resolution of organic strands formed on HOPG from some wedge shaped amphiphilic molecules. Some of the images of fibers formed from liquid crystalline molecules are shown in Fig. 5.10. At a first look, they seem to have a close resemblance with innate graphite fibers in Fig. 5.8 and Fig. 5.12 and it is the need of the hour to unambiguously differentiate adsorbates from these graphite structures.

While considering DNA like strands on HOPG, Heckl explained how the superstructures or innate graphite 1-D structures with well-defined periodicities, could result from misorientation of grains at domain boundaries [187]. The periodicities of bright blobs in these types of fibers which are different from strands/wrinkles varies from 0.67 nm [187] to 1.8 and 5.3 nm [188]. Simonis used the same argument of abutting pentagons-heptagons to explain the double-helical structure observed on bare HOPG. Here also, having the

same periodicity 0.67 nm reproduced by a model of lattices misoriented at 38° as shown in Fig. 5.12(c) [184]. They have additionally showed a supporting simulated STM image, although, the shape of the protrusions could not exactly be reproduced.

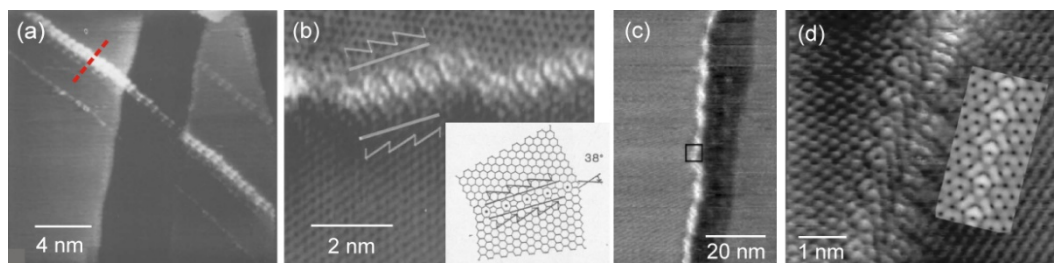


Fig. 5.12 (a), (b) images taken from reference [187] showing how the grain misorientation leading to superstructures on bare HOPG with definite periodicities. (c) Identical structure with same periodicity taken from [184] and explained using the same argument as for (a) and (b). (d) Area within the rectangle in (c). Inset shows a simulated STM image reproducing the periodicity of original STM image albeit with no perfect agreement on the shape of the protrusions.

These types of structures were seldom reported in literature, the predominant ones being the strands or wrinkle-like structures. So, it can be inferred that these structures should be produced and observed only at domain walls. In this thesis work also, no such periodic structures were found. The grain dimensions of graphite are usually of the order of few micrometers and therefore not expected to be always observed with the small scan range of STM used here. In the case of observing fibers with well-defined periodicities, it can be verified whether or not they result from grain misorientation by imaging the graphite lattice on both sides of the strand.

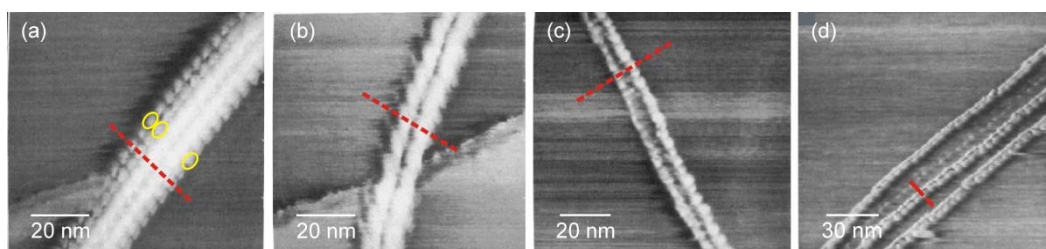


Fig. 5.13 A common feature associated with graphite strands with well-defined periodicity is their parallel arrangement of individual units/bright blobs making a straight line perpendicular to the strand axis, sometimes reminiscent of multiple-tip effect. (a) and (b) taken from reference [23] represent the different parts of the same strand seen on bare HOPG. (c) Strand observed with Nafion on HOPG but believed to be of graphite origin (taken from the same reference [23]) (d) Strands observed on bare HOPG taken from reference [188].

In cases of observing such fibers with well-defined periodic arrangement of individual structural units, it can still be distinguished from adsorbate structures, by adhering to some distinguishing features (i) The distinctive way in which individual units of such fibers are arranged- from various sources reported in literature, a peculiar arrangement of bright blobs (marked in yellow ellipses) in these fibers can be found; the bright blobs always align along a straight line against the fiber axis as if each strand is a replica of the other (see

dashed red lines in Fig. 5.13). However, this is not the case for adsorbate fibers as in the high resolution STM images of Fig. 5.10. (ii) Also, mostly the bright blobs of graphite strands are seen to be of equal size and shape unlike in adsorbate fibers. This reminisces of multiple tip effects. (iii) In the case of observing a strand with a well-defined periodicity, it is a imperative to image the bare HOPG lattice on both sides of the strand to verify/decline the presence of grain boundaries which could cause a periodic structure [187].

2. Occurrence near Steps

Many features which look like isolated fibers could actually be just graphite step edges. Such cases mainly involving the deposition from dilute solutions require extra attention as they may appear absolutely similar to adsorbate fibers at large area scan. Therefore, this needs to be investigated at smaller scan scales. Two cases of bare HOPG results are shown in Fig. 5.14.

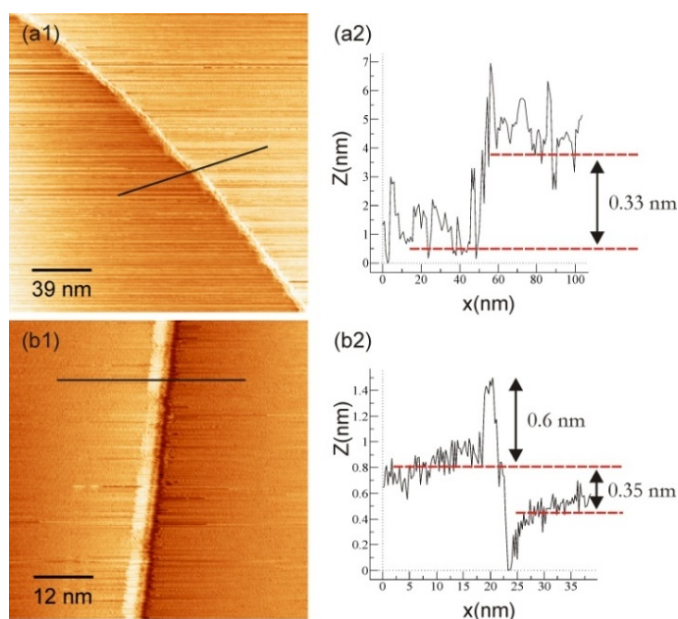


Fig. 5.14 (a1) and (b1) show STM images of fiber-like features resulting from step edge disruptions. (a2) and (b2) are the respective line profiles indicating the presence of single graphite steps.

From the images shown in Fig. 5.14 and many others of this kind, what may appear as an isolated adsorbate fiber on large scan scales, may actually be a graphite step edge.

One of the most prominent 1-D features observed on bare HOPG surface is the fibrous appearance near step edges, whose true origin can be found only by imaging at smaller scans. These fibrous structures seen near step edges may be expected to be caused by the folding-over of graphene layer. And if one expects the layers to fold according to Fig. 5.6, then the strands should make well defined directions with respect to the graphite lattice. However, they were observed to make no definite angles as can be seen in Fig. 5.15.

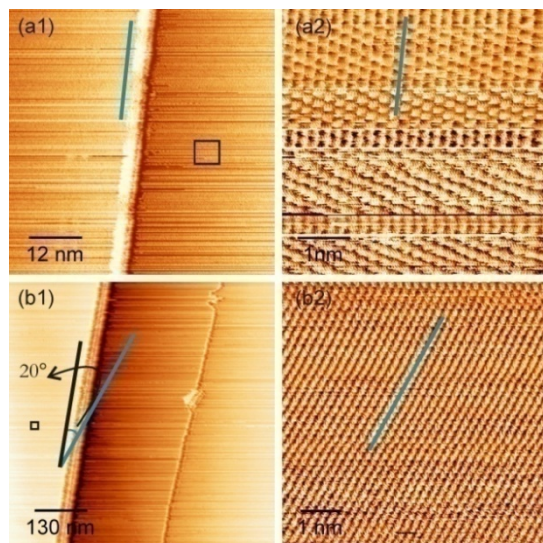


Fig. 5.15 (a1) and (b1) Fiber-like features on step-edges and the angle they make with graphite lattice. (a2) and (b2) are graphite lattice imaged at the regions within the rectangles in the STM images in (a1) and (b1). The blue lines show one of the main crystallographic directions of graphite.

The heights of these protruded linear structures at step edges are always seen to be in the range 0.45 to 0.6 nm. A folding should be expected only when the linear structure makes a definite angle with the graphite lattice. In other cases, higher brightness at step edges is probably a result of a difference in work function of the unoccupied sp^2 orbitals compared to the basal plane [23] or a change from sp^2 to sp^3 [21]. The heights of these protruded linear structures at step edges are always seen to be in the range 0.45-0.6 nm.

3. Large and Small Area Scans

Sometimes, step edge originated fiber-like structures may appear without showing any immediate indication of a single/multi step associated with it (from the uniformity of brightness on both sides of it), and it can be misinterpreted as an adsorbate fiber.

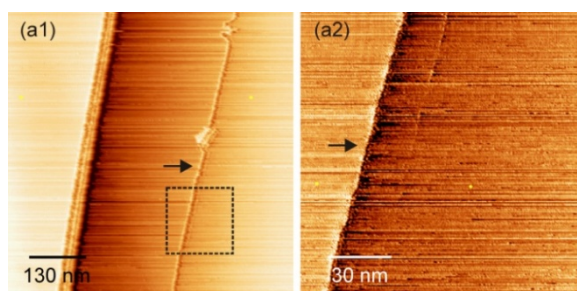


Fig. 5.16 (a1) An isolated fiber-like feature (indicated by the arrow) on bare HOPG. (a2) Region within the rectangle in (a1) at a closer scan clearly showing a single step of graphite (verified from line profile which is not shown).

Fig. 5.16 shows such an example for the linear structure indicated by the arrow. However, imaging the same fiber with a smaller scan range resolves the single graphite step

associated with it. This shows the need to study structures at smaller scans before coming to conclusions from large scans or large scale morphology of adsorbate fibers (see also the following discussion on wrinkles).

There are also real graphite fibers on bare HOPG that are not associated with or produced from step edge disruptions. The graphite fiber shown in Fig. 5.17 is not associated with any step features and represents a real graphite strand. The small range scans of such strands show no well-defined or stable structure unlike in the case of their counterparts seen at grain boundaries (see Fig. 5.12).

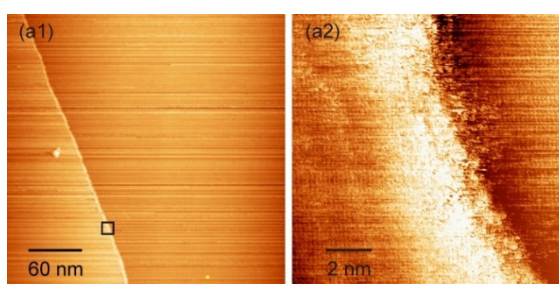


Fig. 5.17 (a1) A real graphite fiber whose origin unrelated to any step disruptions or grain boundary mismatch. (a2) Area imaged within the rectangular region in (a1).

The absence of grains can be understood from the graphite lattice visible on either sides of the strand. However, under most stable conditions, even if the structures could show further details such as a graphite lattice, it therefore should be easily distinguished from adsorbate fibers.

4. Voltage dependence

No significant influence of scanning parameters on image contrast has been observed on 1-D graphitic features.

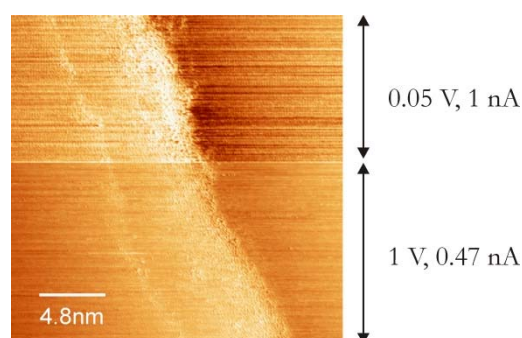


Fig. 5.18 A real graphite fiber imaged at two different scanning parameters as indicated.

Because only pure graphite fibers are of interest and not the often observed step edge disruptions, a pure graphite strand and its image contrast dependence on applied voltage is shown in Fig. 5.18. The bottom part is imaged at 1 V, 0.47 nA, which are typical scanning

parameters for adsorbate structures while the top part is imaged at 0.05 V, 1 nA, typical for the graphite(0001) surface. The z-range which can be used to improve resolution was maintained constant throughout the whole image in order not to influence the contrast variation.

5. Fiber bundles

Another native graphite structure observed is the fiber bundles. In this work, they have been observed only in the presence of an organic solution. Fig. 5.19(a) and (b) shows graphite fiber bundles observed after a drop of the solution of 3CB-8 was deposited on freshly cleaved HOPG.

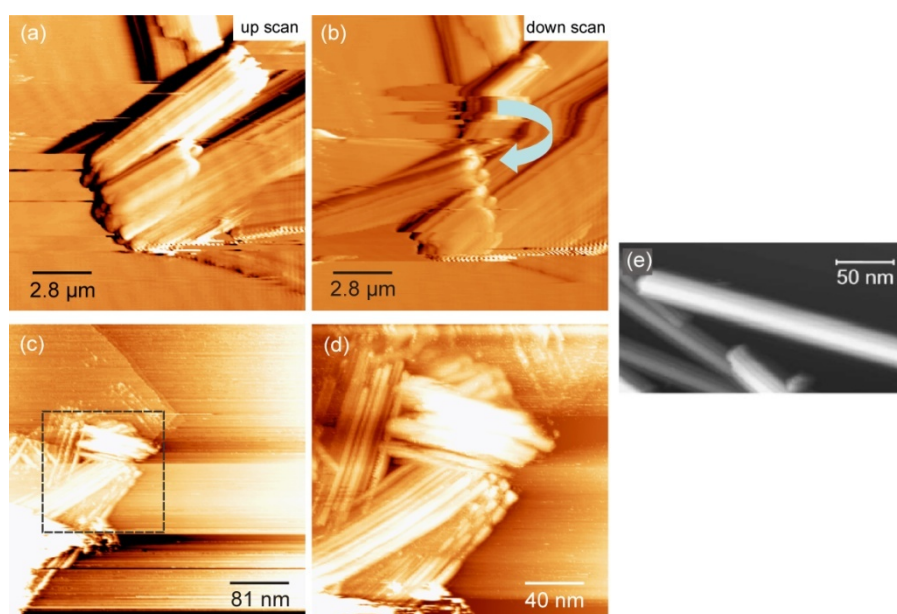


Fig. 5.19 (a) and (b) shows AFM images of fiber bundles presumably of graphite origin observed with an organic solution (3CB-8) on HOPG. (b) Shows the motion of a bundle caused by STM tip during downward scanning. (c) and (d) STM image with another organic solution (2CH-12) on HOPG. (d) Area within the square in (c) showing individual fibers arranged in a parallel fashion. (e) Multi-walled carbon nanotubes deposited on HOPG and imaged by STM (taken from [173]).

The length and width of these bundles varies, but they always appear to be stacked in a parallel fashion. Images (a) and (b) in Fig. 5.19 are consecutive AFM images of the same area one scanned in the ‘up’ direction followed by a ‘down’ scan. During the downward scan, the tip has moved one of the bundles. The tip moved the bundle as a whole without any noticeable damage to the bundle. Image (c) and (d) is a relatively small-area STM image showing similar bundle when another organic solution (2CH-12) was deposited on HOPG. This shows the individual fibers distinctively. One feature of graphite fiber bundles is that they usually occur near multiple steps as can be seen in Fig. 5.19(c). These bundles seem to resemble multi-walled carbon nanotubes deposited on HOPG as in Fig. 5.19(d) [173]. Whether they provide a surrogate and natural path to produce carbon nanotubes needs to be investigated. Although an image was not shown, Campos *et al.*

reported CNT formation on graphene while etching graphene with thermally-activated nickel nanoparticles [148]. In short, whenever such bundles are observed even in the presence of organic solutions, they can most probably be attributed to graphene manifolds.

6. Wrinkles on HOPG

Some of the fiber-like structures seen on HOPG may be what can be called as wrinkles in comparison to what is observed on CVD grown graphene films. This is different from graphite fibers. Wrinkles usually found to have height in the range of 20 to 25 nm. Wrinkles are often interconnected and tend to arrange mostly with an angle of 120° with each other which is more clearly visible for graphene films grown on Ni before transferring them to a Si/SiO₂ substrate [189] but this is not always true.

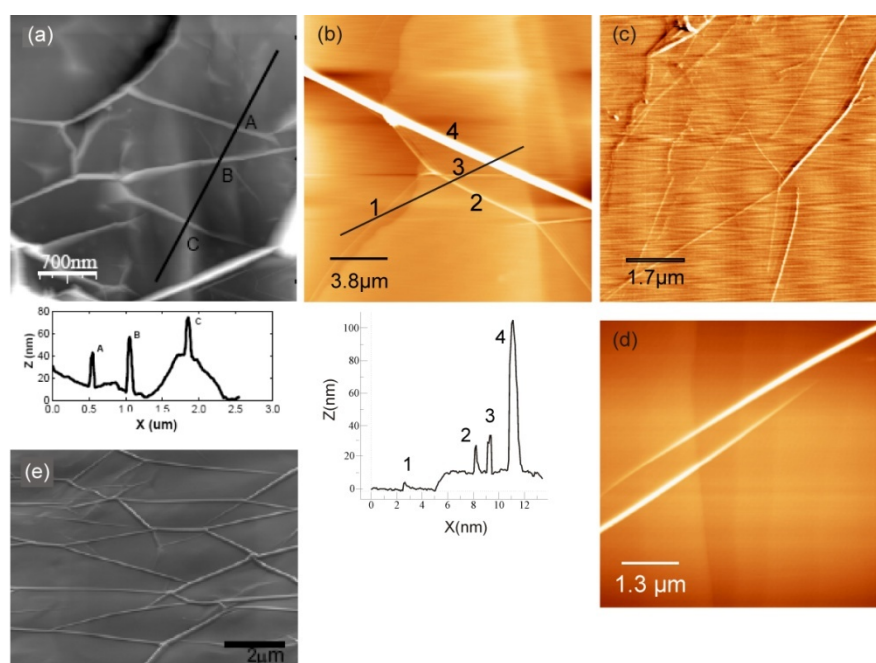


Fig. 5.20 (a) STM image of CVD grown graphene thin film on Ni after transferred to Si/SiO₂ from HNO₃ solution and (below) the line profile for the black line in (a) (courtesy of [189]). (b) AFM image of bare HOPG. The heights of bucklings numbered 1, 2 and 3 are in the range of 20-25 nm which are comparable to those of (a). The 4th bright structure has a height of ~ 100 nm. (c) Another AFM image of bare HOPG showing wrinkles. (d) Bare HOPG showing wrinkles and has a height of 25 nm at the thicker part. (e) SEM image of CVD grown thin graphene films on Ni foil (taken from reference [230]).

Fig. 5.20(a) shows a CVD grown graphene film on Ni after being transferred to Si/SiO₂ from a HNO₃ solution and Fig. 5.20(e) shows a CVD grown thin graphene film on a Ni foil. Wrinkles are the dominant large scale surface morphology on both cases and they could result from tearing and then transferring onto some substrate [190]. Wrinkles of 10 nm width and 3 nm height were also reported for graphene sheets fabricated on SiO₂ through mechanical exfoliation [191]. In contrast to graphene films on Ni or Si/SiO₂, the wrinkle-like features are much less in number on a bare HOPG, as can be seen in Fig.

5.20(b),(c) and (d). From comparison, the wrinkles are essentially the graphite structure of ‘strands’ shown in Fig. 5.8. The thinner wrinkles have a width of at least 150 nm. These structures, although, resemble adsorbate fibers, can be distinguished from strands by the large widths they possess. Isolated organic strands have widths only in the range of few nanometers.

7. Angle between adsorbate fibers and graphite lattice

In the case of adsorbate fibers on HOPG, they are usually aligned along certain directions of the substrate owing to the interaction between alkyl chains and graphite. Unlike fiber-like features observed at step edges, real graphite fibers follow the graphite lattice symmetry.

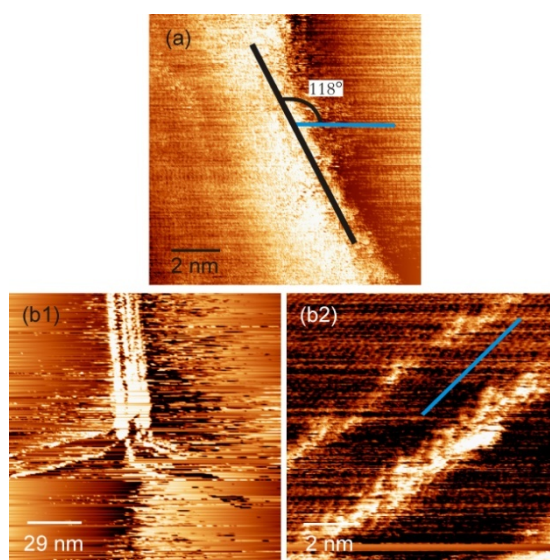


Fig. 5.21 (a) A fiber observed on bare HOPG. The blue line is drawn along a visible graphite lattice direction. (b1) and (b2) Organic fibers on HOPG aligned along graphite symmetry directions.

Fig. 5.21(a) is a bare HOPG image showing a graphite fiber aligned along one of the main graphite crystallographic directions. Fig. 5.21(b1) and (b2) shows organic fibers formed from wedge shaped amphiphilic 3CB-8 molecules on HOPG. The alignment of organic fibers involving alkyl chains is influenced by the underlying substrate symmetry. In contrast to amphiphilic organic monolayers on HOPG, which in general may follow one of the main crystallographic directions, i.e. 60° apart, the experiments here on organic fibers showed also to prefer directions differing by 30° . In any case, they evidently follow the symmetry of the underlying substrate. At least from the data obtained here which shows the obligation of innate graphite fibers also to follow graphite symmetry, as well as the fact that the adsorbate fibers too prefer to follow the graphite lattice, one cannot easily make use of the alignment direction as a differentiating factor.

5.4. Mechanism of innate Graphite fiber Formation

Despite various reports of observing low-dimensional structures on bare HOPG [21-24] as well as wrinkles on graphene films deposited on insulating substrates [189, 191], the origin of these structures remain elusive and unexplained.

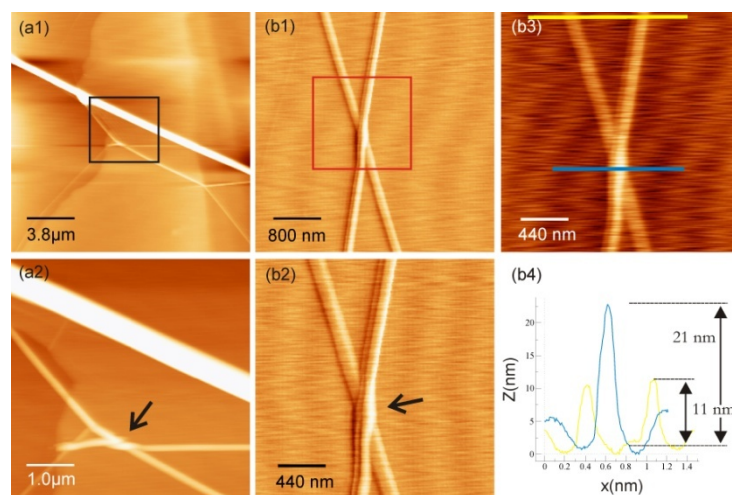


Fig. 5.22 Innate graphite 1-D structures. (a2) shows AFM image taken in the region indicated by the rectangle in (a1). It shows the wrapping around of one fiber on the other at the junction indicated by an arrow. (b2) Shows the region in red rectangle from (b1) in which one fiber is fallen over onto the other. (b4) Line profiles along the yellow and blue lines in (b3). The height at the junction is approximately the sum of heights of individual fibers.

Close inspection of wrinkle-like features shows well separated fibers quite different from what can be visualized as ‘wrinkles’. Fig. 5.22(a2) shows such wrinkles appear bent and wrapped around each other at the junctions, which shows that they actually represent individual fibers rather than just a buckling. This again underlines the need for smaller scans before interpreting 1-D structures on bare HOPG or deposited graphene sheets. They appear to diverge from the junction at angles of 30° or 120° . Fig. 5.22(b) shows two graphite 1-D structures one lying over the other. A simple buckling or strand hypothesis cannot explain features like this. From this analysis and the observation of large fiber bundles, it should be assumed that all fiber-like objects seen on bare HOPG surface cannot be attributed to strands/wrinkles or grain boundaries, but real fibers are also created. The following mechanism is proposed for the creation of these fibers/fiber bundles.

The fibers could be formed during the cleavage process. The graphite fibers might actually result from tearing of graphene flakes from step edges, and the tearing and folding of these flakes probably occur in certain directions as previously discussed [21] [184]. It should be assumed that the edges of graphite steps should be highly unstable and can be torn off very easily during cleavage. Due to the strong intra-layer covalent bond between carbon atoms, only the edges of steps are affected and instead of symmetric graphene flakes

(comparable length and width), asymmetric graphene flakes are torn-off, with the larger dimension along the tearing direction.

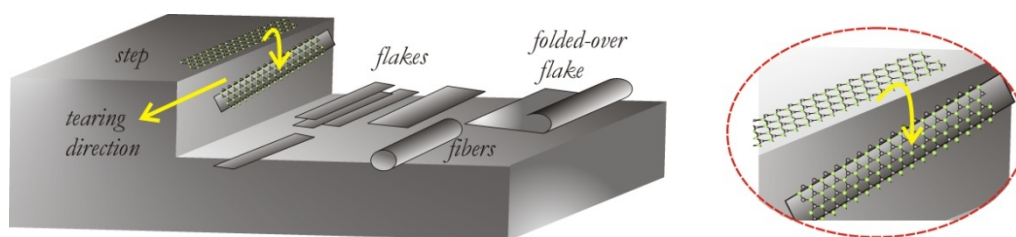


Fig. 5.23 Schematic of the mechanism for the formation of innate graphite fibers during cleavage. The flakes formed during cleavage have large length to width ratio resulting from tight covalent binding within the plane.

As step edges are the most vulnerable, larger number of fibers should be observed when the cleavage force applied is perpendicular to step edges, i.e. perpendicular to the tearing direction. This means that the extension of the graphene flakes formed is much larger in the tearing directions (along zig-zag or arm-chair directions) but only a few to several unit cells long, perpendicular to the step edges. Furthermore, the folding of these flakes should take place along an axis parallel to the longer dimension, which explains why very long graphite fibers are observed.

The flakes formed during cleavage must be highly unstable in their planar geometry and immediately roll into cylindrical rods or folded-over flakes depending on the length of the flakes. Flakes with a smaller width could be forming fibers easily but there must be an optimum width for the formation of fibers below which the flakes may break apart into smaller units or carbon particles. Thus it is clear that when multiple steps are involved, the flakes may not be of a single layer thickness and multi-walled carbon nanotubes can be formed. Apart from this there may also be isolated graphite flakes on the surface which could also form such fibers but the number of such fibers should be larger at step edges. At multiple steps, the probability of creation of a very large number of such asymmetric graphene flakes is higher and fiber bundles may result. The unidirectional alignment of individual fibers within the bundles points towards the origin of fibers from a common step structure. The fiber bundles may or may not have true cylindrical geometry due to the interaction between them and the graphite lattice on which they lie. So, the width of these fiber bundles, in general, should be much larger than their heights.

The mechanism of the origin of fibers proposed here can also explain why wrapped-around and one-over-another fibers are observed. In Fig. 5.22(b2), a second fiber (this fiber on the top looks like an asymmetric flake created from a step edge and folded-over onto itself) fell over the first one which was created before the first one, and already there on the surface. In Fig. 5.22(a1, a2), one of the strands, during its fall from the step edge, wrapped around another one created simultaneously with it. The 'wrapping-around' excludes the 'wrinkle' argument. While graphene deposited on SiO₂ can still have wrinkles,

close inspection of such ‘wrinkle-like’ structures on bare HOPG surface reveals that they are actually created by a process like the one described above.

5.5. Conclusion

Graphite innate structures especially the 1-D ones, with their extreme resemblance to adsorbate structures, can cause ambiguity with adsorbate low-dimensional structures on HOPG. However, they can be identified in a fairly convincing manner if some care is practiced. Some simple measures have been devised to distinguish innate graphene manifolds from adsorbate low-dimensional structures on HOPG. A mechanism is proposed to explain the formation of graphitic fibers/fiber bundles on bare HOPG basal plane. This work is intended only as an initiative towards graphene manifolds and more sophistication is required both experimental as well as theoretical. In the era of ever growing interest in graphene in its fundamental, as well as application-oriented directions, study of various innate graphite/graphene features call for more attention as they can provide valuable insights into the electronic and mechanical characteristics of graphene based structures.

Chapter 6

Liquid-Crystalline Amphiphilic Molecules on HOPG

6.1. Motivation

In chapter 4, the interest has been in self-assembled molecular films, where an attempt was made to understand the self-assembly process of a simple amphiphilic molecule (arachidic acid) physisorbed on HOPG. In this chapter, the attention is on more complex and technologically promising amphiphilic systems. As much as molecular films are important in organic/molecular electronics, so are interconnects- high conductivity organic wires to connect various switching elements. 1-D nano or microstructures of organic semiconducting materials are of great interest for their application to solution-processable organic electronic devices [192]. Electron transport through organic molecules is the basis for a large number of biological processes as well. Chemical synthesis as well as biological routes [193] can be explored for making nanostructures – colloids, nanotubes and wires, to use in micro and nanoelectromechanics and functional nanodevices. Although the crystalline state provides the highest degree of order and stability, the LC state has the advantage that there is a certain degree of mobility and thus the superstructures can be aligned or switched by external fields.

Considering the difficulty of preparing polymer-based systems in a controlled way, supramolecular wires formed through self-assembly, offer a promising route. A long term goal of organic electronics is to borrow nature's method [194, 195] in order to build complex circuits or larger functional ensembles by supramolecular self-assembly in solution. Despite the ubiquitous self-assembled systems seen in nature, the self-assembly of artificial functional molecular systems remains a challenge to the supramolecular chemist. One challenge of the 'bottom-up' approach is the generation of single supramolecular objects that are not part of a three-dimensional crystal or liquid crystalline phase [101].

Organogelators have a tendency to form fibrous structures and recently supramolecular structures formed from gels have captured much interest in the field of nanoelectronics. Self-assembled fibers in gel materials could be used to construct electrically active one-dimensional conductors. The gel state contains nanowires and if their alignment can be controlled, then they may prove useful in nanoscale devices [196]. Some other actively

pursued molecular systems for their electrical transport efficiency include tetrathiafulvalene (TTF) derivatives, polycyclic aromatic hydrocarbons (PAH) and others which can form one-dimensional columnar structures via π -stacking [197] or other selective ion channels involving crown-ether moieties [110, 198].

Several low-molecular weight (LMW) molecules can form organogels. If the volatile solvent can be removed from the gel leaving only the active nanostructures, the nanowires can be extracted. Such fibrous network has other interesting utilities as well. For example, a fiber network with uniform and nano-sized pore can act as a template to fabricate nanostructures and control nanoparticle size and shape. Another example is the drug delivery process that needs an effective holder to retain and release the drug in a controllable manner by means of a desired network structure [199].

Except from biological systems, organogel structures are the only synthetic self-organized linear objects that allow the construction of functional arrangements up to millimeter dimensions. With suitable functional groups they can guide ions, electrons or even photons and can serve as interconnects when integrated into electronic or bioelectronic devices [19, 121, 123, 192]. With such 1-D objects on a solid surface, there is particular importance associated with their orientation with respect to the substrate. The face-on arrangement on the substrate produces vertical columns which can find applications in solar cells and optical displays while the edge-on arrangement with columnar stacks lying parallel to the substrate could be useful for devices having coplanar electrodes such as field-effect transistors [200] and other envisaged chemical lab-on-a-chip applications. The charge transport in crystalline organic materials depends on the molecular packing motifs which control the strength of the intermolecular coupling. Therefore elucidating the structures of such 1-D objects in the sub-molecular regime is inevitable for understanding their true architectures. This knowledge will provide hints on how to design/modify the molecules, so that columns with specific functional properties can be produced.

6.2. Objective

The applications of the wedge shaped molecules depend on their unique supramolecular architectures and a combination of their alignment and conduction properties [201]. It is imperative to understand the architectures of these low-dimensional structures and how their aggregation properties are affected by a solid boundary. This is of both technological as well as fundamental importance. It is also an important question to which extent the stability of the linear structures is determined by molecular interactions and what is the contribution of the molecular geometry. Although the general morphology of fiber aggregates on solid surfaces formed from organogels and their columnar mesophases (LC phases) have been extensively studied using XRD, SEM, TEM, optical microscopy and polarizing optical microscopy, the molecule-by-molecule structural arrangement in individual fibers remains to be revealed. AFM has also been widely used to image organic fibrillar structures adsorbed on various substrates albeit on their larger morphological

features and less on the details of individual fiber structures owing to resolution limitations [202].

In this study, a series of surface-supported supramolecular low-dimensional structures formed from specially synthesized class of LMW wedge-shaped amphiphilic molecules containing amide functionalities are investigated. The objective is two-fold: to elucidate molecule-by-molecule architecture of these structures and to understand how the supramolecular architectures can be selectively produced by fine-tuning the relevant weak inter-molecular interactions. The influence of a solid boundary on the formation of these low-dimensional structures is a natural outcome of this investigation as well. One of the key questions addressed in this thesis work is how the columnar phase depends on the geometry and properties of their corresponding mesogens. Because many weak interactions responsible for gluing the supramolecular architectures together, are rather easily destroyed in solutions as well as in chemisorption process, there is a particular interest in physisorbed systems on solid substrates. The subtle mechanisms governing the aggregation of molecules in solution have been understood to some extent but for a deeper understanding of the fiber structures in solution, they need to be isolated and probed individually in real space.

The first molecular species extensively studied is 3,4,5-Tris(octyloxy)benzamide (3CB-n). Here '3C' stands for '3-chain' meaning the molecule has three alkyl chains. 'n' represents the number of methylene units in each alkyl chain. In order to unambiguously locate the position of the alkyl chains in the 3CB-n strands on HOPG, two different values of 'n' for which a mesophase is known to exist in solution, have been considered. In order to understand the effect of molecular geometry and the influence of secondary hydrogen bonding in the columnar order, the amide group (NH_2) is replaced by a hydrazine group (NHNH_2). The number of alkyl chains in the resulting hydrazine is also varied to elucidate whether molecular geometry plays a role in the fiber formation of (alkoxy)benzoylhydrazines on HOPG. That is, (alkoxy)benzoylhydrazines with three alkyl chains (3-chain hydrazine(3CH)), 2-chain hydrazine (2CH) and 1-chain hydrazine (1CH) have been studied. Further a covalently bound analogue of the two-chain alkoxy benzaamides, namely N,N'-Bis[3,4-bis(alkoxy)benzoyl]hydrazide has been investigated.

To modify one-dimensional structures to meet the requirements for specialized tasks, it is of utmost importance to first elucidate the molecule-by-molecule architecture of a single strand/fiber. To delve into the realm of sub-molecular resolution in real space, scanning probe microscopy is the ideal choice of experimental technique. STM can be used to visualize single molecules in real space and to investigate their chemical and electronic properties. It is also an important tool for investigating supramolecular self-assembly of monolayers as well as epitaxial growth of double and multilayers. It is true that STM has been extremely instrumental in probing planar structures [127] but its capability in imaging isolated organic 1-D structures at sub-molecular resolution has not been demonstrated with the same degree of efficacy. Petukhov et al. have recently succeeded in achieving high

resolution on some magnetic molecules and have clearly mentioned about the difficulty in achieving high resolution [203]. There are very few reports on using STM to obtain high resolution images of strands such that of polypropylene [204], silicon nanowires on HOPG in air and UHV [205], magnetic molecules on HOPG [203], and DNA or biomolecules [188].

In imaging isolated organic fibrous structures particularly related to gel-based systems, difficulties arise in strand isolation, perturbative effects in imaging [206], solvent evaporation resulting in a change in the system conditions during imaging, instability of strands and the destruction of fiber order at small scan areas. The presence of dangling alkyl chains and the non-planar nature of the fiber units further add to the experimental difficulties. Liquid crystals are known to possess a self-assembling tendency to form one-dimensional or two-dimensional liquid phases, which can overcome the thermally activated motion (on a macroscopic scale) of molecules due to the interaction between molecules. Liquid crystals were first studied by STM in 1989 by Spong et al. [62] and STM has been greatly instrumental in elucidating the structure of liquid crystal arrays on HOPG [34, 207, 208]. There have been reports of high resolution STM imaging of planar structures of liquid crystalline molecules on graphite [60, 209] and on other substrates [129], but not many on their 1-D counterparts. In the case of liquid crystal imaging by STM, the image contrast has been attributed to a modification of the work function [62] or resonant tunneling dominated by the LUMO [56, 59]. It is probable that depending on the bias voltage, the STM images may reflect the variation of both the DOS of the adsorbates and the local work function of graphite [210]. As there are no known deposition methods to yield isolated, single fibers, i.e., without clustering or bundling of fibers, the only plausible alternative is to use very dilute solutions. This however makes it hard to find a single, isolated fiber from the vast space of HOPG surface (12 mm* 12 mm) compared to the maximum scan range (below 1000 nm) of the STM used. It is not possible to find the region enclosing isolated fibers by examining with an optical microscope as such fibers are too thin. One can only see thicker fibers/fiber bundles with optical microscope and they are not the focus of the present work.

6.3. Substrate, Solvent and Experimental Conditions

The molecules contain amide functionalities which are capable of forming suprastructures using their hydrogen bonding ability. One of the major problems in the investigation of hydrogen bond involving self-assembly is that the molecules need to be soluble in a non-polar solvent [211]. 1,2,4 trichloro benzene ($C_6H_3Cl_3$)(1,2,4-TCB) is one of the best organic solvents with a low dielectric constant (2.2) and high boiling point (214°C). Out of experience, 1,2,4-TCB is found to be a good choice over tetrahydrofuran (THF) for the molecules and experimental conditions in this work. Another important aspect is the proper selection of the substrate. The formation of self-assembled nanostructures is more complicated on surfaces than in solution due to molecules' interaction with the surface. The substrate as well as molecular functional groups affect the morphology of structures

formed [202]. The substrate is one of the key parameters in determining the supramolecular assemblies of conjugated molecules and the deposition of molecules onto surfaces from solutions can lead to a variety of layer morphologies depending on the interplay of various interactions involved. For conjugated oligomers and polymers, the most usual architecture obtained is fibrillar when the molecule-substrate interaction is weak.

Aksay et al. [129] showed the influence of this factor in the self-assembly into mesoporous structures of the cationic surfactants on mica and graphite. While the channel architecture of the mesoporous silica films is cylindrical on the electrostatic mica surface, it is hemicylindrical on the hydrophobic graphite surface. For a discussion of the influence of the substrate on the self-assembly of discotic liquid crystals on HOPG and Au, see ref. [212]. Similarly, the hydrophobic/hydrophilic nature of the interface can influence the formation of supramolecular architectures. A homeotropic orientation of tapered non-polymeric and polymeric amphiphilic columnar molecules occurs most readily on carbon substrates [213]. HOPG is used as a substrate because of its atomic flatness, chemical inertness and for being hydrophobic. Hydrophilic substrates can hinder the self-assembling ability of molecules to form fibers by interacting with amide functionalities of the molecules. The graphite surface is hydrophobic and does not contain ionizable moieties to attract surface charges. Therefore, the tendency of the molecule to adsorb flat on HOPG is prevented by the amide moieties.

As discussed in the previous chapter, there are some serious issues to be dealt with before interpreting low-dimensional adsorbate structures on HOPG, namely the ambiguity arising from the innate graphite/graphene structures mimicking low-dimensional adsorbate. Therefore optical microscopy (OM) images were taken before and after depositing molecules on HOPG to make sure that organic fibers are indeed formed on HOPG. Furthermore, molecules were deposited on an Au(111) surface, and subsequently large scan area images of the samples were obtained by contact-AFM.

In the experiments, the imaging is done either in solution or after the complete evaporation of the solvent has taken place. Data acquisition involving single-stranded or thinner fibers formed from dilute solutions is an exhausting and time-consuming process; it often takes much time to find an isolated fiber. During this time, the experimental environment may change due to the evaporation of the solvent, tip contamination or tip motion. Phenomenon such as the dewetting (rupture of a thin liquid film on a substrate and the formation of droplets) may also affect imaging conditions. Often, the imaged apparent fiber structure later turns out to be of graphite origin. The experimental conditions itself evolve unfavorably during scanning due to the basic gel nature of molecules, solution concentration and solvent evaporation. The temperature variation was adjusted to be within ± 1.0 °C of room temperature.

In order to find an optimum dilute concentration that produces isolated fibers on HOPG, a dilution series has been prepared and each sample is probed using OM, AFM and STM. Later on, the particular concentration has been repeatedly used for STM investigation for obtaining high-resolution images of isolated organic strands. In some cases when concentrated solutions are used, the solution is heated to about 45-55° to melt the solution into the isotropic phase and a drop of the solution is applied onto the HOPG surface before solidifying. Mostly dilute solutions are used and imaging is done in liquid environment, i.e. with the tip forming a meniscus with the surface. For some concentrations, the solvent evaporates too fast and imaging is done on a surface devoid of solvent. No difference in the structure and morphology of adsorbates is observed regardless of imaging performed solution or not. Fibers/fiber bundles can be more easily found on HOPG with the use of higher concentrations, but in such cases; it is difficult to find an isolated fiber. Locating isolated fibers is the preliminary requirement for deciphering out the molecular architecture down to the sub-molecular level. Very dilute solutions may produce isolated fibers but locating them can be a difficult task as the maximum scan range for the STM is below 1000 nm and the HOPG sample is 10 mm*10 mm. Thicker fibers/fiber bundles can be observed with an optical microscope but no trace of adsorbate features can be observed with an optical microscope on regions where individual, single fibers are present. No significant difference in the morphology/structural arrangement in relation to the solution concentration is found except that higher concentrations give rise to larger bundles of fibers. Higher concentrations often show a gel-like character. Depositions from a very high concentration solidify fast and make it difficult for the STM tip to move over the sample often causing tip crashes and contamination.

6.4. (Alkoxy)benzamides

In this section, benzamides with three alkoxy chains attached are considered. For this reason, it is abbreviated as 3CB-n (three chain benzamide-n). Here 'n' stands for the number of methylene units in the alkyl chain. Two different alkyl chain lengths that are known to form a columnar mesophase in solution, are considered namely n= 8 and 10. The interest in varying the alkyl chain length here is primarily to unambiguously interpret the STM images as the attention is focused on revealing the architecture of the fibrous structures formed on HOPG from these molecules. It also may give provide insights into the influence of alkyl chain length on the fiber formation on HOPG.

6.4.1. 3,4,5-Tris(octyloxy)benzamide (3CB-8)

6.4.1.1. 3CB-n in Solution

In general, the molecular geometry of the mesogens is decisive for the generation of columnar mesophases, i.e. the mesogens must be wedge-shaped. Fig. 6.1 shows the steps

involved in the supramolecular self-assembly process leading to columnar mesophase in the solution [101, 104, 214].

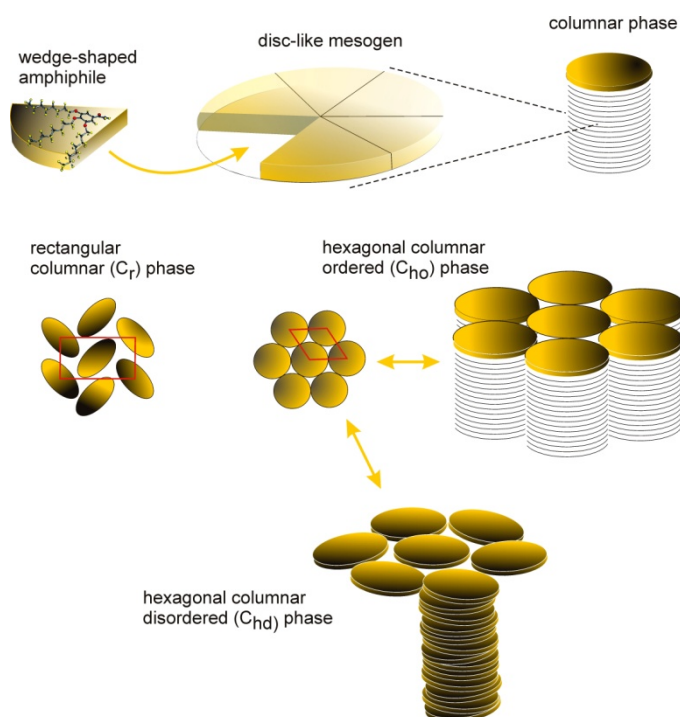


Fig. 6.1 Columnar mesophase formation in solution/melt from wedge-shaped LC amphiphilic molecules. The ellipses represent either a non-circular shape of the mesogen or a tilt of the discs against the column axis.

In Fig. 6.1, the mesogen has the shape of a wedge, which is crucial for column formation. Individual molecules self-assemble into a disc shape and further supramolecular assembly leads to the formation of columns with the discs arranged in a face-to-face fashion. Based on the intermolecular interactions, the columns may further assemble into a hexagonal or rectangular mesophase.

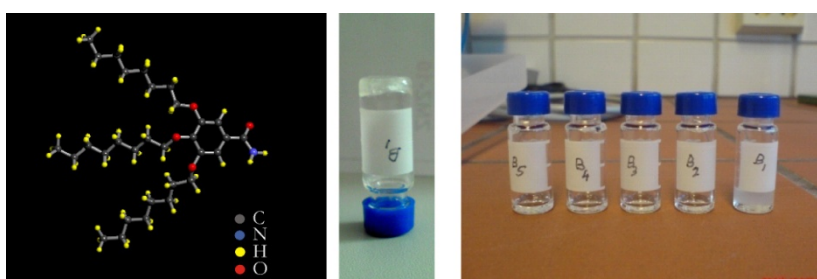


Fig. 6.2 (left) 3CB-8 molecule, (middle) the gel nature of a concentrated solution of the 3CB-8 molecule [101] at room temperature is evident from the viscous nature of the mixture with the bottle turned upside down. For STM studies, mainly dilute solutions are used. (Right) Dependence of gel nature on concentration, dilute solutions do not exhibit gel nature.

The molecules investigated here exhibit gel nature depending on their concentration and temperature. This can be understood from the following explanation. Adding small

amounts of solvent to a thermotropic columnar phase made of infinitely long columns may yield a lyotropic columnar phase. With increasing solvent addition, the orientational correlation between the columns is lost and a spatially isotropic network of the columns results, i.e. a gel is obtained. Fig. 6.2 shows a sample of 3CB-8 in 1,2,4-trichlorobenzene with the bottle in an upside down position showing the viscous solution (“stable to inversion in a test tube” method) representative of its gel nature. Dilute solutions do not show a gel nature and they are the choice of interest here. Earlier studies have shown 3CB-8 to exhibit an opaque or translucent gel nature in various other solvents and the gelation properties improved on increasing the alkyl chain length [182].

3,4,5-Tris(alkoxy)benzamides (3CB) (three chain benzamide) are the most simple class of thermotropic mesogens to form supramolecular columnar phases [101, 182]. While 3,4,5-Tris(alkoxy)benzamides are known to form stable columns, 4-alkoxybenzamides or 3,4-bis(alkoxy)benzamides only form crystalline structures. The 3,5-bis(alkoxy)benzamides form only a monotropic columnar phase. The mesophase generation depends also on the length of the alkyl chains. Short chain 3CB- n (3CB- n) ($n \leq 4$) shows a crystalline structure, 3CB-5 exhibits a monotropic phase and for $n = 6-14$, an enantiotropic columnar phase has been observed [101].

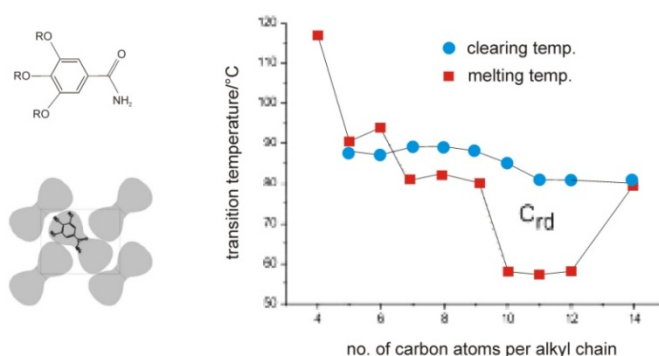


Fig. 6.3 (courtesy of [101]) Dependence of transition temperatures of 3,4,5-tris(alkoxy)benzamides (3CB- n) on the length of alkyl chains. C_{rd} represents rectangular columnar disordered mesophase. The molecule structure is shown on the left, R represents alkyl chain. The mesogen arrangement is schematically shown on the lower left.

The most stable phases are observed for $n=7-9$, which do not crystallize but form mesoglasses on cooling below -30 °C and exhibited the largest clearing enthalpies ($\Delta H_c = 6.1$ to 6.9 kJ/mol) and entropies ($\Delta S_c = 17.4$ to 18.4 J/mol K) of the whole series. Between $n=12$ and 14 , the melting temperature increased sharply reducing the temperature range of the columnar phase (for $n=14$, $T_c - T_m = 1$ °C). Also, attaching longer alkyl chains with $n > 15$ is found to impede mesophase formation presumably due to alkyl chain crystallization. The 3CB- n fibers forming dimers are found to be inclined at $25-30^\circ$ with respect to the column axis. The resulting mesophase exhibits rectangular symmetry (C_{rd} , $P2_1/a$). In the columnar mesophase, inter- and intra-dimer hydrogen bonds play a crucial role with the weaker intra-dimer hydrogen bonding contributing considerably to the stability of columns. In this thesis, 3CB- n with $n = 8$ and 10 are considered.

6.4.1.2. OM and AFM images of 3CB-8 on Au(111) and HOPG(0001)

Firstly, OM and AFM images of 3CB-8 from a 2.856 wt.-% solution was deposited on an Au(111) were obtained and results are shown in Fig. 6.4. Prior to deposition of molecules, the gold sample was rinsed in ethanol for one minute to remove hydrophilic contaminants.

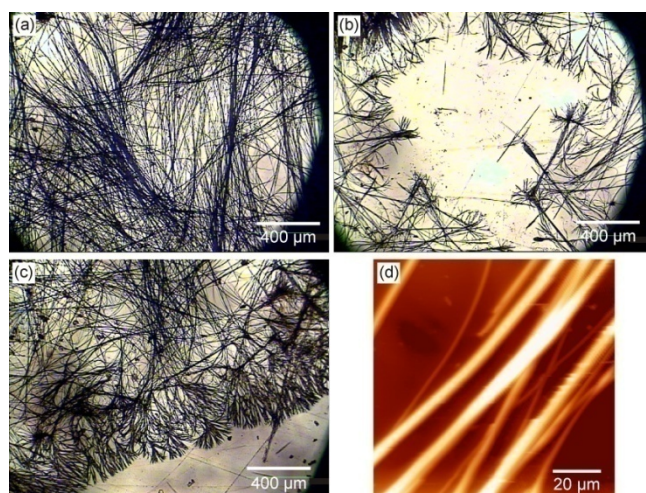


Fig. 6.4 Optical microscopy And AFM (lower right) images of 3CB-8 on Au(111)) surface showing fiber bundles.

As fibrillar appearance is evident on Au surface, in order to find appropriate solution concentration for STM studies, different concentrations of 3CB-8 on HOPG were tried. OM and AFM images of two such distinctive cases, one concentrated (2.856 wt.-%, same as used for Au) and the other dilute (0.285 wt.-%), are displayed in Fig. 6.5.

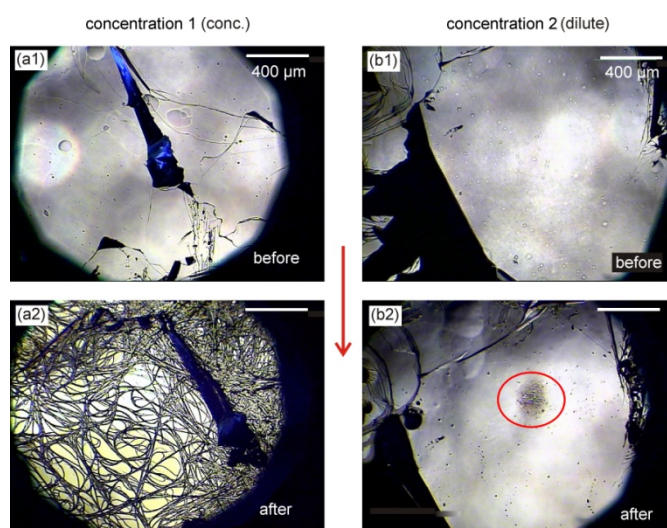


Fig. 6.5 Optical microscopy images taken before and after the deposition of 3CB-8 on HOPG. For deposition from dilute solution (right), the coverage is very low and the fibers are observed only on a small region within the region marked by the red ellipse.

As concentrated solution exhibits a gel nature at room temperature, it is heated to 45° for five minutes to obtain a clear solution and is then immediately applied to the substrates. For STM studies a dilution series of the molecule is prepared as discussed earlier and mostly 0.285 wt.-% or lower concentrations are used in order to avoid clustering or bundling of the fibers.

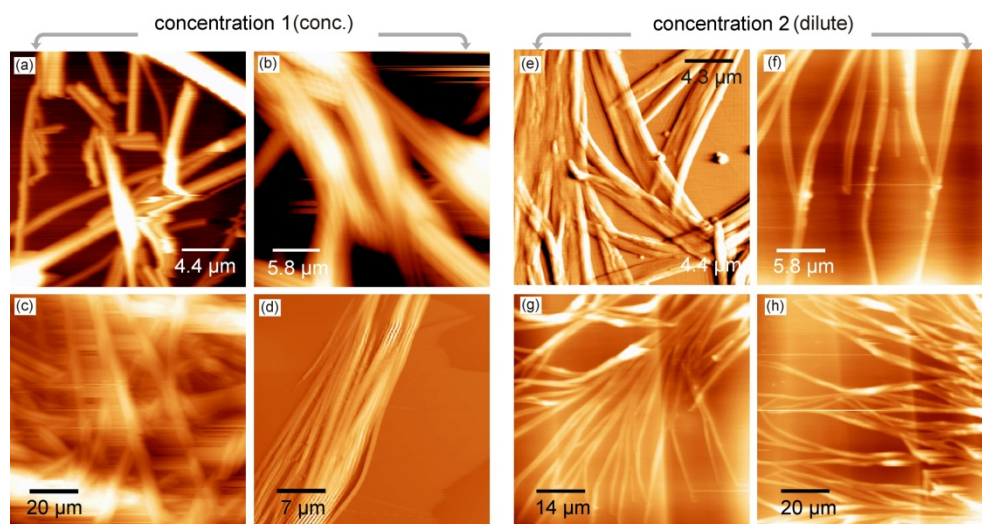


Fig. 6.6 AFM images of 3CB-8 on HOPG for the respective concentrations of the optical microscopy images in Fig. 6.5. All the images are taken at different areas on the sample. (a-d) show fiber bundles of 3CB-8 formed from a concentrated solution. (e-h) Fibers/fiber bundles formed from a dilute solution of 3Cb08 on HOPG.

Following the OM imaging, both samples are investigated by contact-AFM (Fig. 6.6). There is no immediate inference one can make from the two different concentrations except that higher concentration yielded much thicker fiber bundles. For concentrated solution, the phase on HOPG is close to the gel state with solvent molecules holding the fibrous network together.

For the same concentration, the fibrillar morphology on Au(111) is similar to that on HOPG. It should be mentioned that the gold sample⁴ is much larger than the HOPG sample and for each case; one drop of the solution is cast on the surfaces using a micropipette. The drop completely covers the HOPG surface while only partly covering the gold surface and dewetting effects results in a branch-like appearance on Au. The dilute solutions produce thinner fibers with heights and widths ranges of 25 to 140 nm and 600 to 1200 nm respectively. They, however; represent fiber bundles and not single fibers. Comparing the AFM images for concentrated and dilute solutions, it can be seen that the concentration does not affect the linear dimension of the fiber appreciably along the long axis. This show that individual fibers are formed, followed by bundle formation. Therefore the molecules' tendency to form long-chain fibers is easily discernible. The larger bundling observed for the concentrated solution could be caused by the presence of solvent

⁴ Gold sample - 20 mm* 20 mm, HOPG sample - 10 mm* 10 mm

molecules (as in a gel) trapped in between the network. Images are taken when visibly no solvent is present on the surface except that some solvent may still remain partially entrapped within the fiber bundles. The thinnest and isolated fibers are the focus of the present study which cannot be observed in detail with the AFM used.

6.4.1.3. STM images of 3CB-8 on HOPG

Some of the STM images of 3CB-8 fibers formed on HOPG are shown in Fig. 6.7. In the STM experiments, after a drop of the dilute solution is cast on to the HOPG surface, it takes some time for the solvent to completely evaporate from the surface. The structure of the fiber remains unchanged irrespective of whether the imaging is done in the solution or after complete evaporation of the solvent.

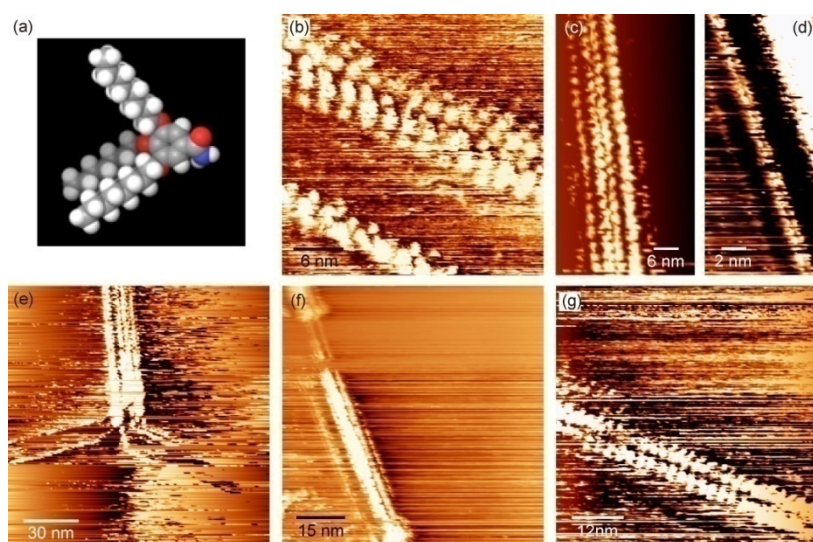


Fig. 6.7 (a) Geometry optimized structure of 3CB-8 calculated using *Macromodel 8.0*. The amide moiety and aromatic ring are out of plane by 26° . (b-g) Some of the STM images of 3CB-8 nanofibers formed on HOPG. In (b), (d) and (g) single-strand or three-strand structure is visible while (c), (e) and (f) shows larger bundles with individual chains stacked in a parallel fashion. Imaging parameters for (b) and (g) - 1.6 V, $I_t = 0.6$ nA, for (d) - 0.23 V, 0.62 nA, for (c), (e) and (f) - 1.36 V and 0.6 nA. A concentrated solution was used for (b),(c), (e) and (g). (d) and (f) were obtained from a 0.57 wt.-% solution.

The individual fibers/fiber bundles once formed are observed to be stable over many hours or even days on the HOPG surface. The individual strand structure of 3CB-8 is found to be independent of the solution concentration. It should be mentioned that on rare occasions, the graphite surface with 3CB-8 molecules shows a layer structure. This however, originates from top graphene layer rotation (see chapter 5 for details).

3CB-8 Linear Dimensions

The most frequently observed (and probably most stable) fiber structure consists of three-strands with the central strand having larger lobes with a diameter of ~ 2.2 nm, and the smaller bright blobs on either side of size ~ 1.4 nm each. Fig. 6.8(a) shows three of such

three-strand fibers with a width of 5.3 nm each. One of the fibers is lying in proximity to another while the third one is isolated. The period of the bright blobs along the fiber axis is 2.58 ± 0.19 nm. The distance between the central strand and adjacent strands show two different but discrete values- it is either ~ 1.7 nm or ~ 2.3 nm. This implies that at some places, strands (more specifically the bright blobs on it) are closer to each other than at other places.

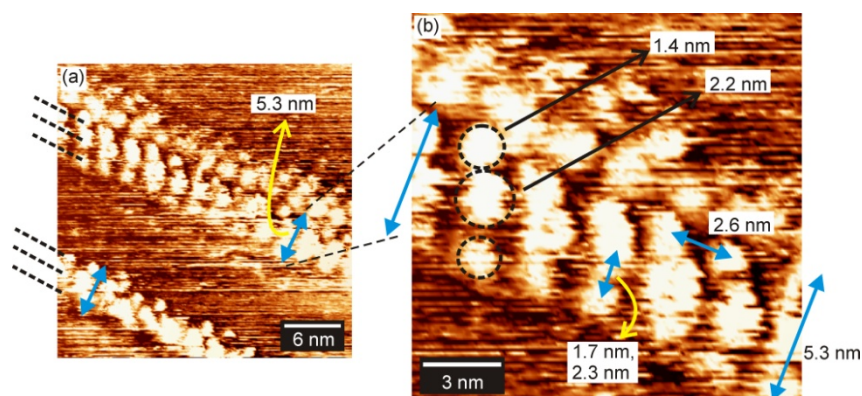


Fig. 6.8 (a) A high-resolution STM image of 3CB-8 fibers on HOPG showing the three-strand geometry. Three such three-strand fibers can be seen, each having a width of 5.3 nm. One three-strand fiber lie isolated while the other two are in close proximity. (b) Dimensions of a three-strand fiber. The STM imaging parameters are $V_b=1.6$ V and $I_t=0.6$ nA.

The larger blobs in the central strand are often seen with a dark region. As will be shown later, the three-strand fiber actually consists of a total of four single strands- three (represented by dotted lines) of them shown in the STM image and one strand underneath which is not directly visible in the STM image. The size of the bright blobs can give the number of molecules present in the structure but caution is required due to its position in a 3-D object constituted by individual elements lying in a non-planar geometry. Therefore, before discerning the origin of the bright blobs, let us look at the benzamide structure and STM imaging. The tilt of the molecular core with respect to the column axis is a common feature in many columnar mesophases and 3CB-8 is known to have a rectangular disordered phase (C_{rd}) in solution. In addition, the benzamides exhibits a deviation from the planar geometry in their gas phase by a 26° rotation between the amide group and the aromatic ring [215]. The aromatic part, due to its higher electron density usually appear as bright in STM images and the aliphatic part as dark in the color scale [60].

As the existence of a certain type of stable structure namely three-strand geometry is evident, it is essential to look for thinner fibers such as single-strands, which could be the most basic linear structure of 3CB-8 aggregates. Fig. 6.9(a) shows one such single-strand fiber while (b) shows many such strands combined together to form a thicker fiber (bundle). While the single strands usually exhibit blobs with a size of ~ 1.4 nm with a dark hole at the center and four lobes of size ~ 0.4 nm each, bright blobs in some strands increase in size to ~ 2.2 - 2.3 nm when the chains combine to form thicker fiber geometries. The fiber bundle in Fig. 6.9(b) also shows two different spots of different

sizes, either 1.4 nm or 2.3 nm. This larger blob can accommodate 6 lobes each of ~ 0.4 nm in a circular arrangement. As seen in Fig. 6.8, the three side-by-side blobs of the three-strand fiber do not arrange themselves along a straight line but in a space-filled manner with the smaller blobs packing into the free space in between the larger blobs of the middle chain. Also, the distance between a thin strand and a thick strand is different from two thinner strands.

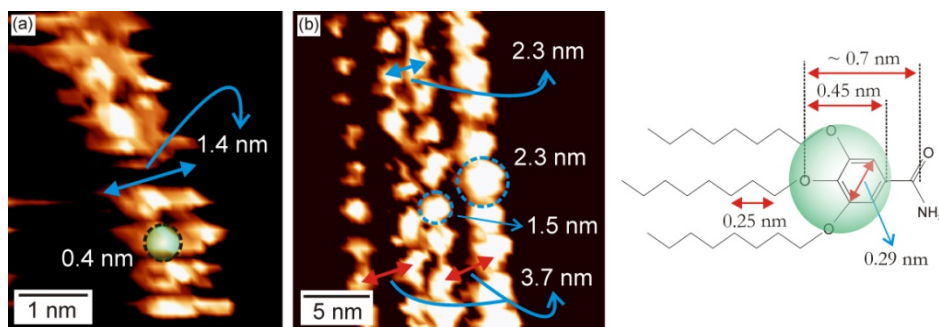


Fig. 6.9 (a) A high-resolution STM image of a single-strand fiber of 3CB-8 on HOPG. The periodic units in the fiber are tetramers. Imaging parameters $V=0.23$ V, $I=0.62$ nA. (b) A fiber bundle constituted by many single-strand (tetramer and hexamer units) fibers. Tunneling conditions are 1.36 V and 0.6 nA.

The size of the smallest bright spots in Fig. 6.9(a) is in the range of 0.4 to 0.5 nm, which is approximately the size of the green area in the drawing on the right side of Fig. 6.9, the sphere includes the aromatic core and the oxygen atoms. The aromatic core has a higher electron density due to the delocalized orbitals and is expected to be observed as a brighter region in the STM image compared to the sigma-bonded aliphatic chains (the HOMO-LUMO gap of aliphatic chains is in the range of 8 to 10 eV). However, the smallest observed spots (0.4 to 0.5 nm) are slightly larger than the aromatic core (aromatic ring size ~ 0.3 nm).

To understand the origin of the bright regions, let us look at the molecule closely in its electron density and molecular orbital (MO) aspects. The frontier molecular plots are sometimes employed [57] to successfully identify the sub-molecularly resolved STM images obtained at higher voltages falling within the energy range of the orbitals and their dependence on bias polarity. Within the molecular-orbital (MO) approximation, the net electron density in a molecule is the sum of occupied MO densities. Although in molecular aggregates, the proximity of the molecules can induce a splitting of the individual HOMO and LUMO energy levels, HOMO and LUMO are usually plotted in order to roughly understand the influence of frontier molecular orbitals in STM imaging.

The calculations are done using *ArgusLab*. 4.0.1⁵. In *ArgusLab*, a preliminary geometry optimization is done using a molecular mechanics force field such as the universal force field (UFF). The calculations of frontier orbitals and ESP are done with structures

⁵ *ArgusLab* 4.0.1, Mark A. Thompson, Planaria Software LLC, Seattle, WA, <http://www.arguslab.com>

optimized with the Austin Model (AM1) semi-empirical Hamiltonian. Here the HOMO and LUMO are superposed on the molecular structure of 3CB-8 (Fig. 6.10(a) and (b)). For tunneling into the LUMO (tip negative) or out from the HOMO (tip positive), protrusions are expected with different symmetries as shown in Fig. 6.10(a) and (b). No similarity is found in the STM images with regard to the HOMO or LUMO of the free molecules.

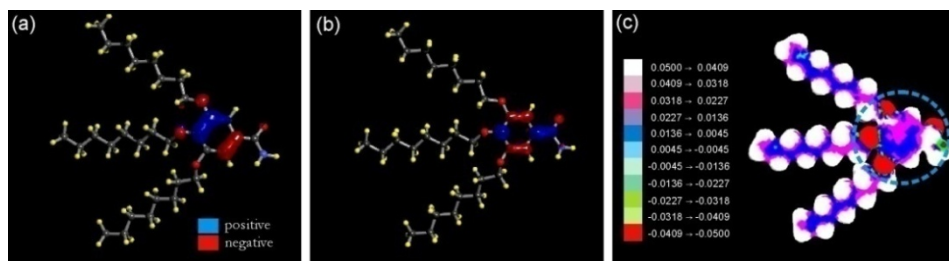


Fig. 6.10 Frontier molecular orbital and ESP (electrostatic potential) calculations for isolated 3CB-8 molecule using *Arguslab 4.0.1* (see text for details). (a) HOMO, (b) LUMO and (c) ESP. In (c), red and white colors represent the values for the most negative (electron-rich) and positive regions ESP.

A concept recently explored [216] for STM image interpretation of physisorbed molecules at low voltages is the electrostatic potential (ESP). ESP has been considered as the most significant discovery in quantum biochemistry in the last three decades and widely has been used to estimate the reactivity of molecules. It is the potential energy felt by a positive ‘test’ charge and thus electron-rich regions in the contour surface have negative potentials. In an ESP surface, the electron density surface gives the shape of the surface and the value of the ESP on that surface is represented by colors. In Fig. 6.10(c), surfaces of the electrostatic potential (in Hartrees, $1 \text{ H} = 27.2 \text{ eV}$) is mapped onto an electron density iso-valued surface. Regions relatively rich in electrons have a negative electrostatic potential (towards the red end in the color map in Fig. 6.10(c)). The ESP plot shows that the highest negative potentials are at the sites of oxygen atoms and the aromatic core is also at a higher negative potential. Therefore the smallest bright blobs (0.3 to 0.5 nm) appearing in the STM images represent the region of the molecule covering the oxygen atoms and the aromatic core. The STM may not be capable of separately resolving the oxygen atoms from the aromatic core in the present non-planar geometry.

From the molecular structure in Fig. 6.9, a 3CB-8 cyclic dimer will have a length of ~ 1.4 nm from oxygen end of one molecule to the oxygen end of the other molecule in the dimer. As the alkyl chain is not expected to appear bright in the STM image, the bright blobs with dimensions of 1.4 nm (in the strands on either side) can accommodate a dimer. Because of the circular shape of the spot, it can contain at least four molecules. Thus tetramer units are formed instead of 3CB-8 dimers, with molecules in a tetramer interconnected by hydrogen bonds. The middle chain similarly has larger blobs with a circular shape of 2.2 nm in size. They may represent hexamer units with six 3CB-8 molecules forming a circular H-O hydrogen bond network.

Angle between 3CB-8 Fiber and Graphite Lattice

In general, the morphology of films formed after solvent evaporation from gels are identical on polar and non-polar surfaces but there is a clear influence from the surface when the solvent evaporates from gelator solutions [196]. The presence of alkyl chains in the amphiphilic molecules can influence the monolayer ordering of the molecules on HOPG [111]. Similar to the simple alkanes on HOPG [93], [142], the alkyl chains of LC mesogens on HOPG are also known to follow the substrate symmetry [60, 209]. In monolayer structures of simple alkanes or alkyl derivatives, aliphatic chains can be usually observed with STM and appear as zig-zag bright protrusions [217]. For some monolayer structures, only the aromatic part can be imaged by STM, but in some other cases, both the alkyl chains and aromatic cores can be concomitantly imaged [218]. Hence, the imaging is system specific and additionally, if the alkyl chains are mobile and dangling, they are usually not imaged by STM.

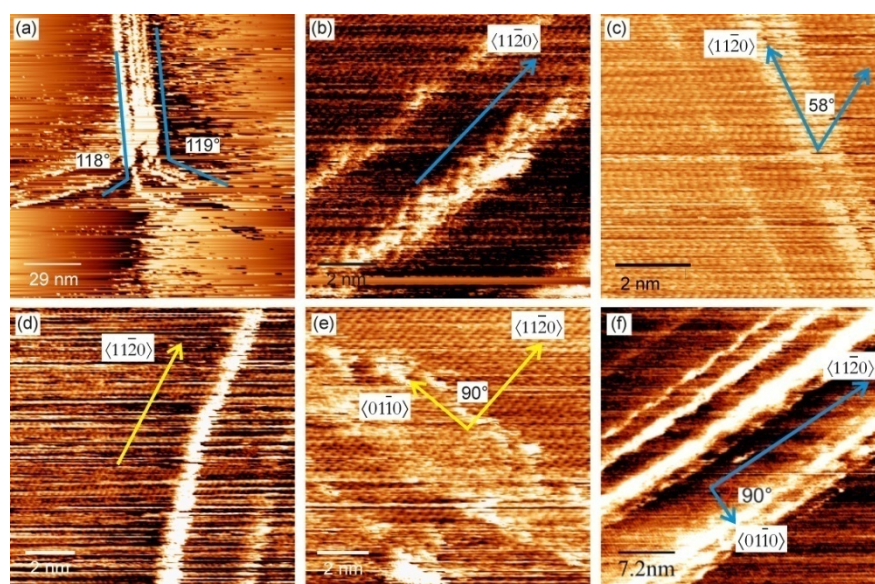


Fig. 6.11 STM images of 3CB-8 fibers/fiber bundles showing the orientation with graphite lattice. (a) Small fibers combining to form a big fiber. (b-f) 3CB-8 fibers imaged with underlying graphite lattice. Imaging parameters - (a) 1.36 V, 0.6 nA; (b) 0.29 V, 0.58 nA; (c) 0.19 V, 0.6 nA; (d) 0.33 V, 0.6 nA; (e) 0.3 V, 0.6 nA; (f) 0.32 V, 0.6 nA.

Fig. 6.11(a) shows a rare fortuitous observation of two fibers of different widths combined at a junction to form a thicker fiber, with all strands following specific graphite lattice directions. This exemplifies the strong influence of the substrate on the fiber alignment on HOPG. On the other hand bigger bundles of fibers do not show any particular alignment. From STM images in Fig. 6.11(b-f) showing the fiber and the underlying graphite lattice in one frame, 3CB-8 fibers are seen to be aligned along either of the two graphite crystallographic directions namely the $\langle 11\bar{2}0 \rangle$ or the $\langle 01\bar{1}0 \rangle$ directions. Usually the alignment of molecules takes place along one of the main crystallographic directions. Here it is not the molecules but the fiber that is aligned along these directions. The specific

alignment of fibers along certain directions indicates the influence of the substrate via van der Waals forces. A conclusion to be drawn from the directional orientation of these fibers is that at least one out of the three alkyl chains of the molecule is attached to the graphite lattice.

For a better understanding of the graphite surface on a simple unit of basic 3CB-8 molecules, say a 3CB-8 dimer, some basic simulations have been performed with *Macromodel 8.0* [219]. The force field calculations may not be as accurate as *ab-initio* methods, nevertheless, they offer useful supporting information. The simulations are limited to a vacuum environment and temperature to absolute Kelvin. *Macromodel 8.0* simulation program is highly efficient for the energy minimization of molecular configurations. An example is the minimized structure of 3CB-8 with a non-planar structure yielding a 26° rotation between the amide moiety relative to the plane of the aromatic ring (see Fig. 6.7(a)).

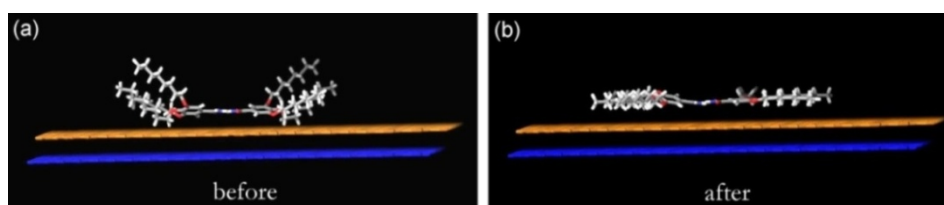


Fig. 6.12 Calculation with *Macromodel 8.0* for graphite-molecule interaction. (a) side-view of 3CB-8 dimer before and (b) after interaction with two 'frozen' graphene layers.

Simulations are done with the AMBER force field. Structure optimization is done using the Polak-Ribiere conjugate gradient (PRCG) algorithm until a final gradient below a convergence threshold of 0.005 kJ/mol \AA is reached. The HOPG surface is constructed from two polyaromatic sheets separated by 0.34 nm . This structure is then made to be 'frozen' so as to avoid any conformational changes for the graphite layer when interacting with molecules. One dimer of 3CB-8 molecules is then placed at a distance of about 0.5 nm from the top graphene layer as shown in Fig. 6.12(a) and minimized with respect to the force field energy gradient. As a result of the interaction with graphene layers, the alkyl chains which were originally lying away from the graphene are forced into a 'flat' configuration. The graphene-molecule distance in the resulting configuration is measured to be 0.26 nm .

Heights of fibers

The average height of a single-strand fiber is ~ 0.4 to 0.5 nm . However, when single-strand fibers combine together, the resulting structures exhibit a height ranging from 0.4 to 0.8 nm . This means that the fibers are not just placed side-by-side but there is significant interaction between the fibers presumably via alkyl chains. This also clearly shows that, unlike in solution, a hexagonal or rectangular symmetry for the fiber cross-section is not possible on HOPG.

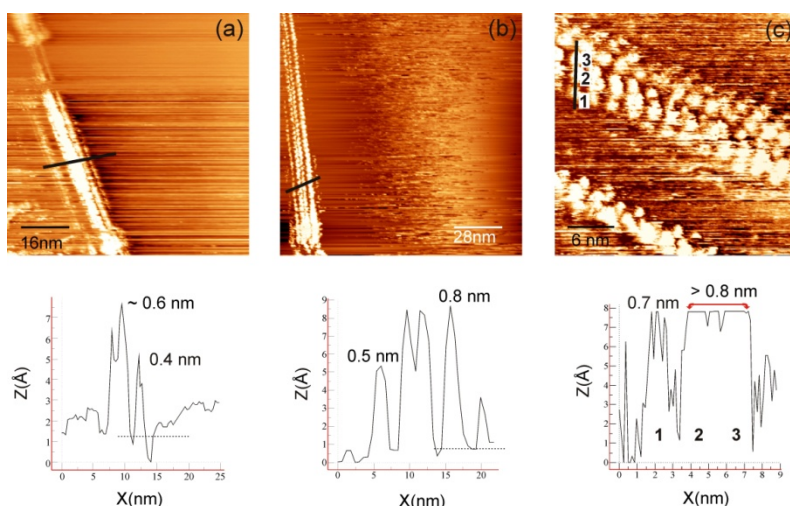


Fig. 6.13 (a-c) 3CB-8 fibers and their corresponding height profiles. Tunneling parameters for all images are 1.36 V and 0.6 nA.

An analogous observation is worth noting. The hydrophobic/hydrophilic nature of the interface has profound influence on the formation of supramolecular architectures on surfaces [129, 220]. On hydrophilic mica, electrostatic interactions [221] between substrate and surfactant head groups result in cylindrical micelles which meander across the surface exhibiting a loose registry to the underlying substrate lattice (Fig. 6.14).

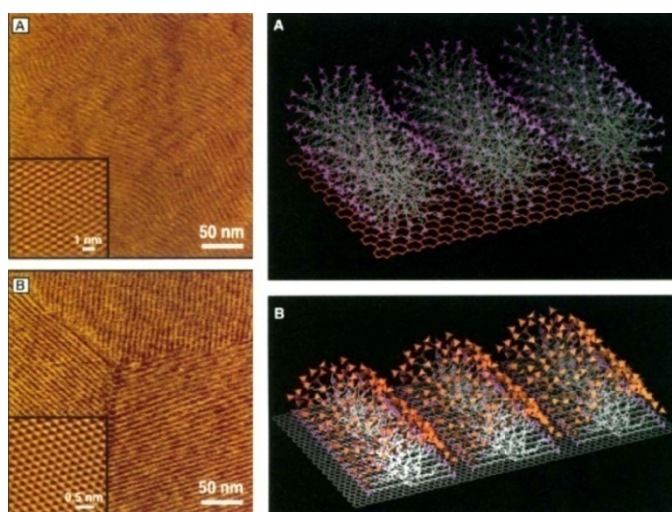


Fig. 6.14 (courtesy of Ref [129]). Supramolecular surfactant self-assembly of cetyltrimethyl ammonium chloride (CTAC) on (A) mica and (B) HOPG surfaces.

In contrast, hydrophobic and van der Waals interactions between surfactant tails and HOPG cause adsorption horizontally which lead to hemi-micelle cylinders. On the other hand for the case of nickel phthalocyanine molecules, the morphology of their helical assemblies is found unaffected by the type of substrate and both mica (hydrophilic) and HOPG (hydrophobic) produce helical nanofibers [222]. Note that these are not isolated strands but essentially planar structures consisting of molecular films.

6.4.2. 3,4,5-Tris(decyloxy)benzamide (3CB-10)

As we have seen from the previous section on 3CB-8, the location of the alkyl chains is not immediately discernible from the STM image. Alkyl chains usually appear in STM images as a result of topographic effects [127] and a parallel arrangement to the surface is the best configuration for this.

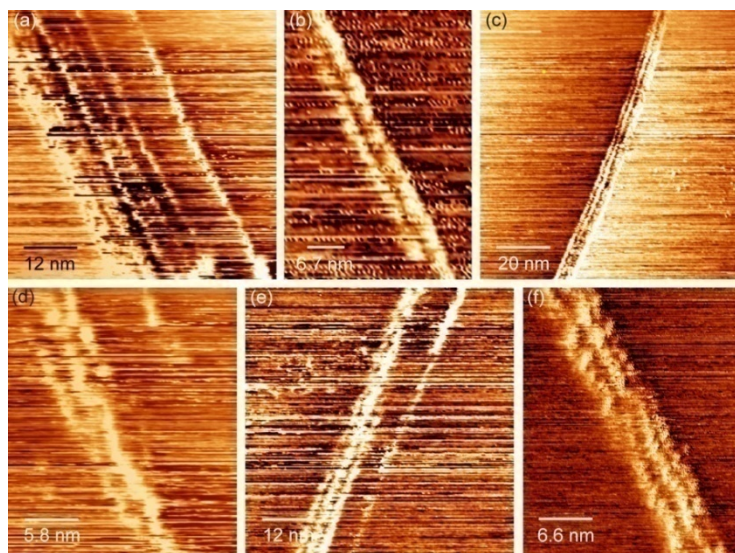


Fig. 6.15 Some of the STM images of 3CB-10 fibers formed on HOPG.

Due to the non-planar geometry of the blobs constituting the three-strand fiber, the alkyl chains presumably appear as ‘dark’ regions between the bright blobs. In order to unambiguously verify this, a molecule has been synthesized with the length of the alkyl chain increased by two methylene units ($n=10$). A comparison of results from both 3CB molecules can provide a clear understanding about the location of the alkyl chains in the fiber complex as well as decipher subtle details regarding the influence of alkyl chains on the 3CB- n three-strand fiber structure. Fig. 6.15 shows some of the STM images of 3CB-10 fibers formed on HOPG. For both 3CB-8 and 10, a common feature observed is the formation of fibers with three molecular strands (three-strand fiber) which is the most often observed isolated fiber entity. The three-strand geometry may be the preferred fundamental configuration for strand formation from dilute solutions, and it may favor the stabilization of the different inter-molecular and inter-strand interactions in an optimized manner.

The influence of alkyl chains in self-assembly of organic molecules is widely known [96] and the alkyl chain length defines the 2-D architecture [223]. In general, the tendency to form ordered monolayers increase with increased chain length as shown for alkanic acid monolayers on aluminium [96]. The reason for this is either an increased van der Waals interaction (2-D crystallization) between the aliphatic chains or their interaction with the substrate. A larger interaction area per molecule gives rise to a larger orientation effect which is the reason for an alignment with respect to underlying graphite. It should be

more amenable to get high resolution showing both aromatic and alkyl parts when the molecule lies on a plane and the interdigitation of alkyl chains can be imaged [224]. Simple alkyl chains lie parallel to the HOPG substrate but when attached to aromatic or functional parts with a non-planar geometry and when the molecule has more than one alkyl chain, they may either lie parallel to the substrate or freely float in random directions. This makes it difficult to image the alkyl parts apart from their insulating nature resulting from sigma bonds [225].

3CB-10 Linear Dimensions

Fig. 6.16 shows a single-strand 3CB-10 fiber. The periodicity, width and individual spot sizes in an isolated 3CB-10 fiber are 1.55 ± 0.05 nm, 1.4 nm and 1.4 nm respectively. Thus going from 3CB-8 to 3CB-10, although the alkyl chain length has increased by 0.25 nm, the periodicity along the fiber axis has decreased by ~ 1 nm.

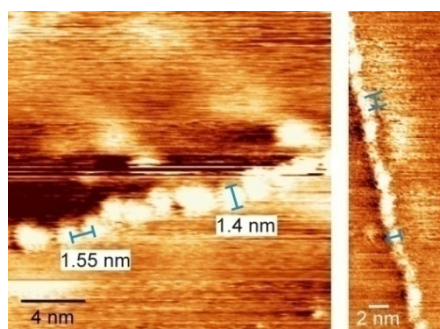


Fig. 6.16 Two different STM images of a single-strand 3CB-10 fiber. Tunneling parameters for STM image (left) are 1.09 V, 0.48 nA and (right) 1V, 0.43 nA.

For the 3CB-10 fibers with 3-chain structure (Fig. 6.17), the lateral distance (against the fiber axis) between the bright blobs is either 2.2 or 2.9 nm and the width of a three-strand 3CB-10 fiber is ~ 6.6 nm. These are 1.7 or 2.3 nm and 5.3 nm respectively for the 3CB-8 fiber.

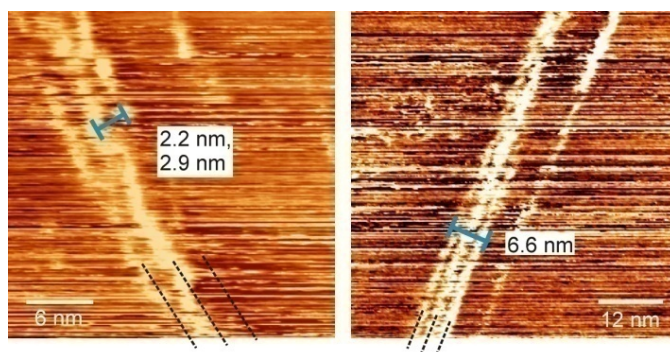


Fig. 6.17 STM images of three-strand 3CB-10 fibers formed on HOPG. Imaging parameters for left and right STM images are 1.06 V, 0.43 nA and 1.09 V, 0.48 nA respectively.

Angle between 3CB-10 Fiber and graphite Lattice

The angle between an isolated 3CB-10 fiber and the underlying graphite lattice follows the same pattern as for the 3CB-8 fiber.

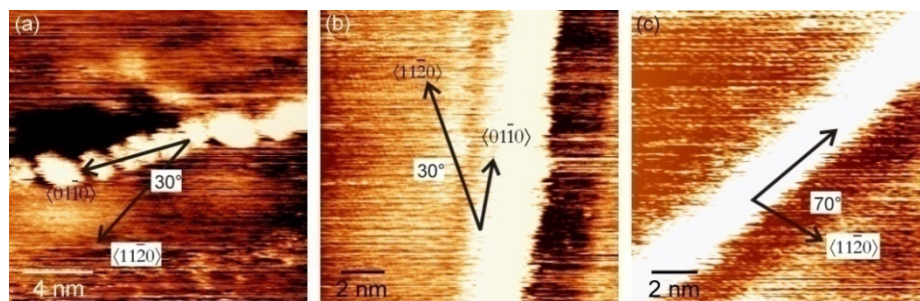


Fig. 6.18 The orientation of 3CB-10 fibers with underlying graphite lattice. Imaging parameters - (a) 1.07 V, 0.48 nA.; (c) 1.08 V, 0.43 nA.

Fig. 6.18(a) and (b) shows both the 3CB-10 wires as well as the underlying graphite lattice with the strands oriented along the $\langle 01\bar{1}0 \rangle$ graphite direction. In Fig. 6.18(c), there is a deviation of 10° from the $\langle 11\bar{2}0 \rangle$ direction; however this might have been caused by a motion of the loosely bound strand during scanning. Hence, just like the 3CB-8, 3CB-10 fibers also follow either the $\langle 01\bar{1}0 \rangle$ or the $\langle 11\bar{2}0 \rangle$ directions.

Height of 3CB-10 fiber

The maximum height of the three-strand 3CB-10 fiber is ~ 0.55 nm which is slightly less than that for the 3CB-8 fiber.

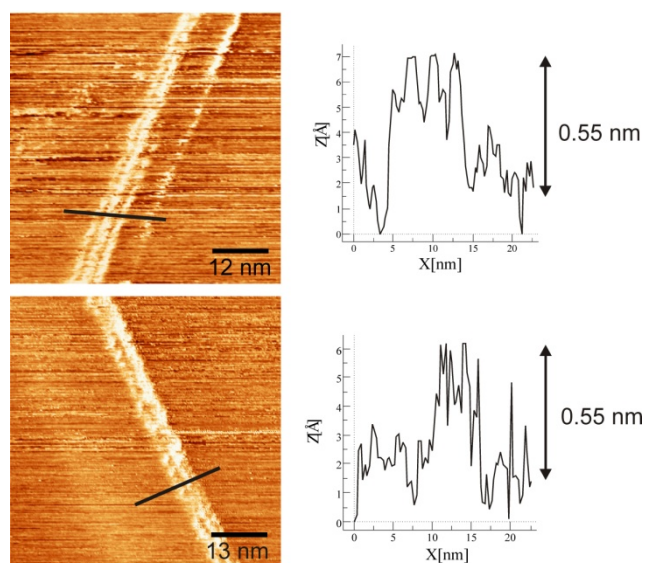


Fig. 6.19 Three-strand 3CB-10 fibers and corresponding height profiles along the blue lines in the STM images.

As for the 3CB-8 three-strand fiber, the heights of the individual strands differ slightly. The reduction in the height can be explained by the increase in the lateral distances (against the fiber axis) between strands.

6.4.3. Compare 3CB-8 and 3CB-10 Structures

Both 3CB-8 and 3CB-10 strands show a width of ~ 1.4 nm for a single-strand fiber. As mentioned earlier, this distance is of the dimension of end-to-end oxygen distance (Fig. 6.10) of a 3CB-*n* dimer which is independent of the alkyl chain length. This is one of the indications that the alkyl chains are not imaged (or appear dark) in the STM images. As illustrated in Table 6.1., compared to the three-strand 3CB-8 fiber, the 3CB-10 fiber has its periodicity along the fiber axis decreased by ~ 1 nm while the lateral distances between individual strands in the three-chain fiber exhibit an increase for both the lowest and the highest values by ~ 0.5 - to 0.6 nm. The 3CB-8 molecule has a stretched alkyl chain length of 0.87 nm and 3CB-10 has a stretched alkyl chain length of 1.12 nm, yielding a difference in the length of the alky chains of 0.25 nm.

TABLE 6. 1

	3CB-8	3CB-10
alkyl chain length	0.87	1.12
periodicity	2.6	1.55
inter-strand distance	1.7, 2.3	2.2, 2.9
width (three-strand)	5.3	6.6

From the table, it is clear that the alkyl chain length variation is manifested immediately in the periodicity (along the fiber-axis). This provides a ‘relaxation’ against the fiber axis causing an increase in the inter-strand distance. This increase in the distance between strands is twice the increase in length of one alkyl chain; each alkyl chain from the participating strands contributes 0.25 nm each. The increase in the inter-strand distance observed in the STM image is ~ 0.5 to 0.6 nm. The decrease in the periodicity is a direct consequence of the higher interdigitation of alkyl chains along the fiber direction. The slight reduction in the height of three-strand 3CB-10 fibers on HOPG compared to their 3CB-8 counterparts also can be ascribed to the same ‘relaxation’ between hexamer/tetramer strands. Other common features between 3CB-8 and 3CB-10 fibers include their basic fiber geometry and the orientation relative to the graphite lattice. The alignment of both 3CB-8 and 3CB-10 is along either the $\langle 11\bar{2}0 \rangle$ or the $\langle 01\bar{1}0 \rangle$ direction. There is a three-strand appearance for the often observed fiber architecture of both 3CB-8 and 3CB-10 strands, which could be the thermodynamically stable form of the 3CB-*n* fibers on HOPG. The three-strand (actually four strands) leads to a less ‘flat’ structure and a closure of the fiber cross-section becomes possible with the minimum number of

strands. This geometry is also a result of a ‘space-filled’ packing of the bright blobs when individual strands combine together to form a three-strand fiber.

6.4.4. Model for 3CB-n fibers

Single-strand 3CB-n fiber

Apart from the often observed three-strand fibers, the presence of isolated, single strands indicates that the smallest linear entity of the 3CB-8 molecule is a perfectly ordered single chain. The STM images suggest no dimer formation, but only tetramer and hexamer configuration can exist as basic building units. Single-strand fibers consist of a linear array of bright blobs (tetramer units) interconnected by alkyl chains.

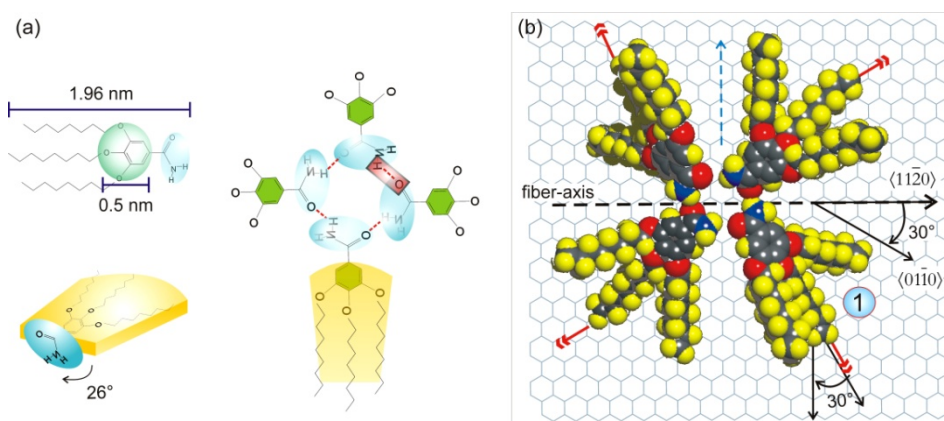


Fig. 6.20 Cartoon showing the formation of 3CB-n fibers on HOPG from individual molecules. The amide cores slightly ‘float’ above on the HOPG with alkyl chains (only those indicated by red arrows) partially attached to HOPG providing the necessary anchoring.

Each bright blob in the STM image covers a region of an aromatic core together with its neighboring three oxygen atoms. From each molecule, only one alkyl chain (middle one) attaches to the HOPG surface providing an anchoring effect. In the tetramer units, the amide functionalities form cyclic hydrogen network that ‘floats’ on the surface. The simulation done using *Macromodel 8.0* shows (Fig. 6.12) the effect of putting a single 3CB-8 dimer on the HOPG surface made of two graphene layers. The interaction with graphene sheets made the alkyl chains to lie flat on the graphene. This however is valid only for a single dimer and when a non-planar geometry of the basic units (tetramer) in the single-strand (or three-strand fibers) are considered, a complete ‘flat’ alignment of the length of the alkyl chains cannot be expected.

Considering one single unit (tetramer) of the single-strand fiber, the four alkyl chains- one from each molecule, is attached to the graphite (indicated by red arrows) which providing a good anchoring effect. This alkyl chain graphite interaction is alternatively along $\langle 11\bar{2}0 \rangle$ and $\langle 01\bar{1}0 \rangle$ directions for molecules within a tetramer. In Fig. 6.20, the fiber axis is along $\langle 11\bar{2}0 \rangle$ with the middle alkyl chain of the molecule numbered ‘1’ attached to the graphite

along $\langle 11\bar{2}0 \rangle$ direction. The middle alkyl chain of the neighboring molecule lies along $\langle 01\bar{1}0 \rangle$. However, the locations occupied by the participating alkyl chains are quite arbitrary and if molecule '1' instead would occupy the $\langle 01\bar{1}0 \rangle$ direction, the whole tetramer unit will rotate by 30° resulting in a fiber alignment along $\langle 01\bar{1}0 \rangle$. In short, the direction the alkyl chains occupy is arbitrary to one of the two directions and the fiber alignment along either of the graphite directions viz $\langle 11\bar{2}0 \rangle$ and $\langle 01\bar{1}0 \rangle$ results essentially from the four-fold symmetry of the tetramer units. The other two alkyl chains on either side are dangling and extend away from the surface. The formation of very long molecular strands requires reasonably strong forces along the strand axis. If there is no inter-tetramer interaction, then no 1-D structure would result as there is equal probability for every molecule or tetramers to meander across the surface. It is also possible that there are single-strand fibers with hexamer units but such structures have not been observed in experiments. The hexamer pattern is observed only for the middle strand in a three-strand fiber, i.e. a fiber formed by three strands with a hexamer-strand in the middle and one tetramer-strand on either side.

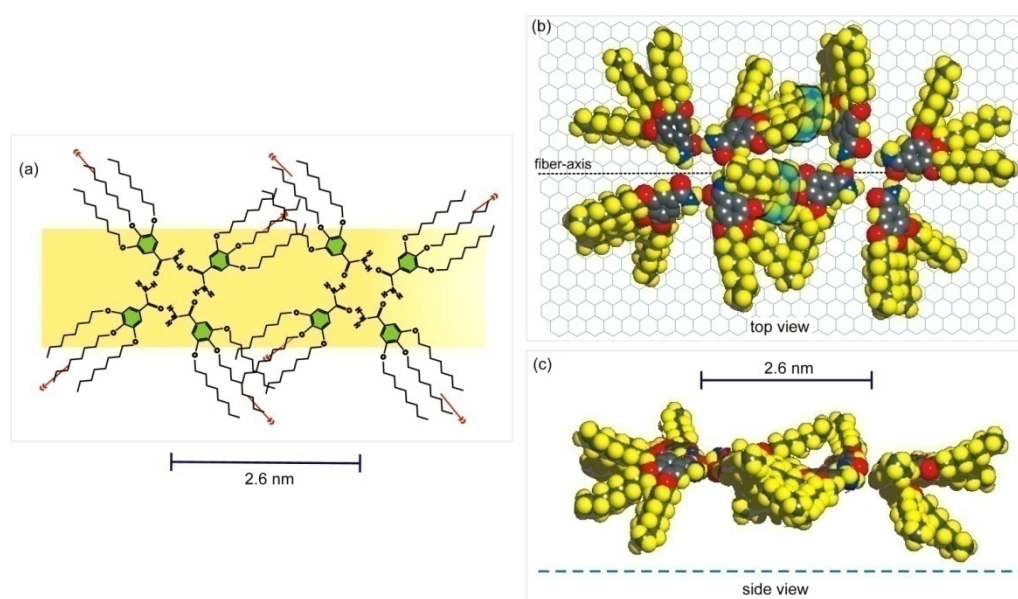


Fig. 6.21 (a) Schematic of the single-strand fiber formation from tetramer units. The hydrogen-bonded tetramer unit does not lie on a plane. (b) Top-view of two building units interacting via dangling alkyl chains and (c) Side-view of the same.

When individual tetramer units assemble linearly to form a single-strand fiber as in Fig. 6.21, the two dangling alkyl chains of one tetramer interact with the alkyl chains of the subsequent unit. The alkyl chains interdigitate and this provides cohesion along the fiber-axis direction. The weak interaction provided by these alkyl chains may explain the lower number of single-strands on HOPG compared to three-strands. However, once formed, the anchoring to graphite also plays a key role in its stability. It is possible that the subsequent tetramers are slightly rotated with respect to each other about the fiber axis to

favor a smooth interdigitation of alkyl chains but this is not unambiguously discernible from the STM images.

Three-strand 3CB-n fiber

The basic building unit (dotted blue arc in Fig. 6.22) of a three-strand fiber is a combination of two hexamers and two tetramers. The basic model is the same for both 3CB-8 and 3CB-10 although the diagram is specifically shown for the 3CB-8 fiber. The periodicity of 2.6 nm allows for an interdigitation of dangling alkyl chains without overcrowding the sphere cores. The middle strand has a width of 2.2 nm and the strands lying on either side of 1.4 nm each.

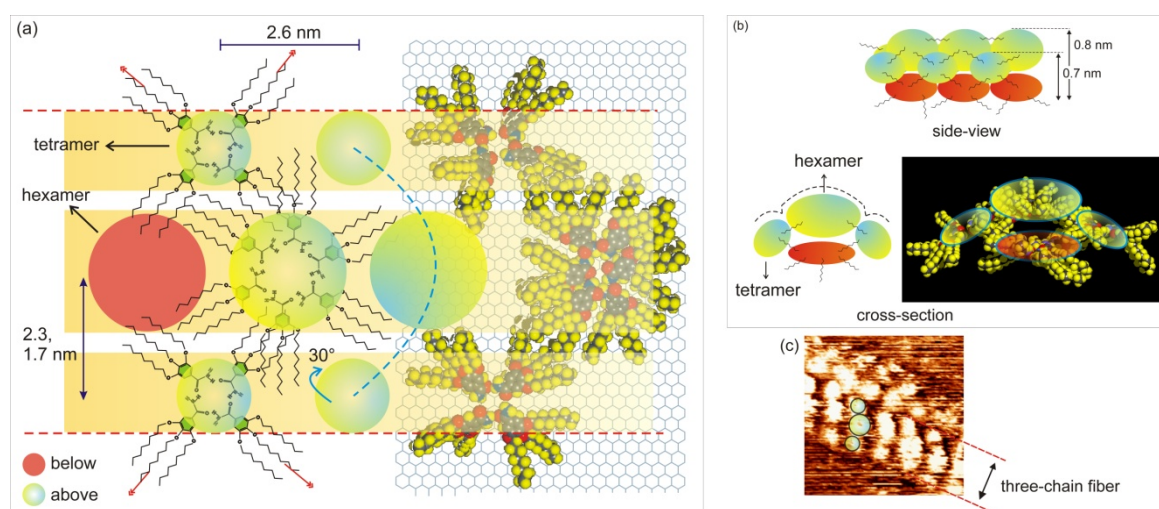


Fig. 6.22 Formation of three-strand fiber from two linear arrays of tetramer units on either sides (smaller green spheres) and two linear array of hexamer units, one on top (larger green sphere) and other on bottom (red sphere). (a) Top view of three-strand 3CB-n fiber (model shown for $n=8$). The skeletal model of molecules is shown lying on a plane although the molecules actually have an out-of-plane geometry. (b) Cross-sectional and side views of the three-strand fiber, the arrangement of basic building unit interconnected by alkyl chain interactions. (c) STM image of a three-strand fiber (enclosed within the two dotted red lines) with the green spheres superposed.

The formation of the three-strand structure is dictated as well by a lateral space-filled packing (against fiber axis) induced by alkyl chain interactions between the strands. The architecture of the fibers should be the same for any 3CB-n fiber with 'n' suitable for column formation on HOPG. The tetramers interact with the hexamers via the two dangling alkyl chains on the sides of the strands. Similarly two of them also interact in the same manner with the underlying hexamers. The other alkyl chains of the tetramers are attached to the graphite as for a single-strand fiber but now only partially due to the constraints induced by the curvature resulting from inter-strand interactions. A shift of the hexamers relative to each other along the fiber axis cannot be expected due to the completely dark region between the bright blobs in the STM image but the hexamers and tetramers are clearly displaced relative to each other. The height of the central chain in three-strand fibers is approximately twice that of its side chains. This shows a curved

geometry for the fiber but definitely not a cylindrical or rectangular cross-section. The central strand with hexamer units does not interact with the graphite lattice but is supported on either side by the two tetramer single-strands. The alkyl chains play a crucial role in the ordering along the direction of the fiber as well. There is inter-hexamer and inter-tetramer interaction via dangling alkyl chains along the fiber direction. This facilitates the inter-connection between basic building units of the fiber and yields overall stability.

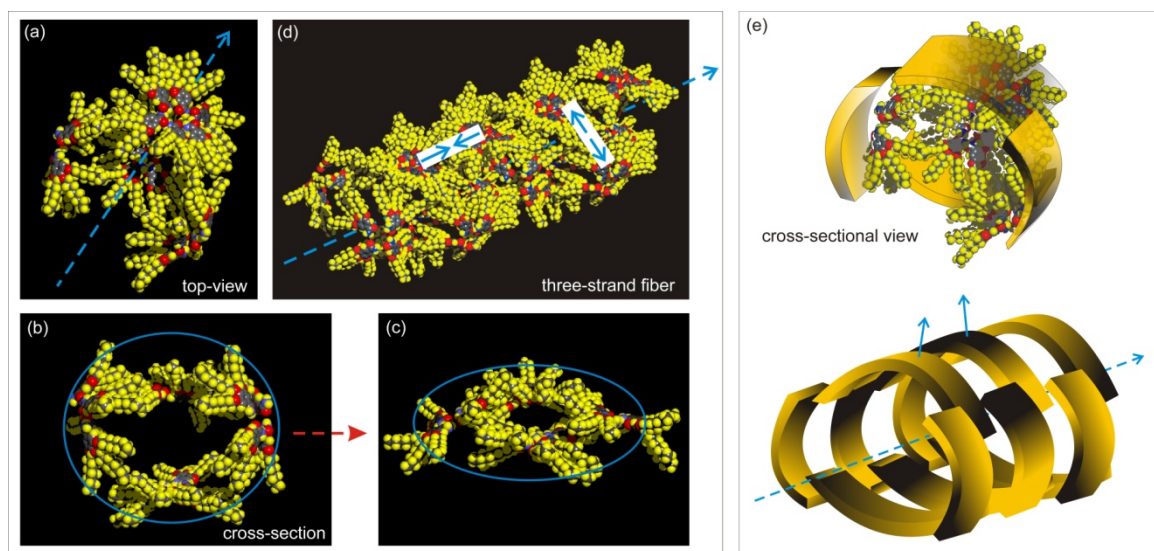


Fig. 6.23 (a) and (b) show respectively the top and cross-sectional view of a single building unit of a three-strand fiber of 3CB-8 (speculated model when no graphite is present). Compare this cross-section with rectangular disordered phase in solution. Three-strand fibers actually consist of four strands with one strand underneath. (c) The actual cross-section of the same unit on HOPG which is a more ‘flat’ configuration induced by graphite-alkyl chain interaction, mainly of the bottom hexamer and partly from the two tetramers on either sides. (d) Top-view of a 3CB-8 three-strand fiber with four periodic building units combined. (e) One basic building unit of the three-strand fiber and (below) schematic of fiber formation. The rotation of hexamers results in a tilt of adjacent units.

Fig. 6.23 is a proposed model for the three-strand 3CB-n fiber on HOPG. Only (c) represents the fiber geometry on HOPG while (a) and (b) is shown with the distance between top and bottom strands (hexamers) exaggerated for the ease of visualization. The more ‘flat’ structure in (c) is a result of the interaction mainly of the bottom hexamer and partially from the two tetramers with the graphite lattice. This kind of interaction of the alkyl chains with graphite on either side of the three-strand and the hexamers gives a strong anchoring effect and provides the necessary stability for 3CB-n fibers on HOPG. From the non-planar geometry of the hexamers and the fact that each molecule in itself is also non-planar with an angle of 26° between the amide group and benzene ring, the subsequent hexamers are rotated slightly with respect to each other about the fiber axis. This in turn rotates the tetramers as well due to the alkyl chain interactions and effectively appears as a tilt of subsequent fiber units (one fiber unit is shown in Fig. 6.23(e)) due to the curvature of the fiber-cross section. This rotation angle could be 30° from the symmetry considerations and enhances the interdigitation of alkyl chains between subsequent fiber units. The rotation is evident from the STM image as a dark hole in the

center portion of the hexamer blobs which is not observed for every unit (Fig. 6.8). This tilt could be the cause for the observation of two different inter-strand distances of an essentially 3-D object measured on a 2-D plane. This also implies that the fiber as an entity is stable and the fiber formation is independent of the molecule-graphite interaction. Although alkyl chains are attached to the graphite lattice yielding an alignment effect, it should be inferred that the fiber architecture is largely unaffected by graphite-molecule interactions except a ‘flattening’ of the fiber structure (cross-section).

Here one of the hydrogen atoms from the amide moiety is involved in the hydrogen-bonded network in the tetramer/hexamer units and the other hydrogen atom seems redundant in the formation of column structures on HOPG while the un-substituted benzamide crystal consist of two sets of hydrogen bonds; one connects molecules to form cyclic dimers, while the other sets of hydrogen bonds act as gluing force between dimers to form endless chains along one crystallographic axis [215]. In the case of the single-strand or three-strand fibers formed on HOPG, no information can be discerned from the STM image about the role, if any, played by the secondary hydrogen atoms in strand formation. Nevertheless, it may have a role in the further aggregation process leading to the formation of fiber bundles by three-strand fibers getting attached to each via a face-to-face hexamer/tetramer configuration. It can be speculated that as in the case of hydrogen bonding, π - π interaction may also play a crucial role in the formation of fiber bundles.

Conclusion: 3CB-n fibers

High resolution STM imaging of 3CB-n fibers formed on HOPG provides valuable insights into their architecture. Fibers formed from 3CB-n with two different ‘n’, varying in length by two methylene units, have been investigated to understand the influence of the alkyl chain length on the fiber structure and dimensions. The role of alkyl chains is crucial and they provide the necessary interaction forces between the building units (hexamer/tetramer) along as well as against the fiber axis. The most stable form of the isolated fibers is a three-strand structure which is semi-cylindrical. The STM images do not reveal the possibility of any stacking of disc-like mesogens as expected in the 3CB-n solution which is a rectangular columnar disordered mesophase (C_{rd}). The fiber formation of 3CB-n resembles more of carbon nanotubes (CNT’s) than a stacking arrangement (as in solution) in the sense that the strands are formed by a closure of tetramer/hexamer loops. Thus the structure is different from that in the columnar mesophase in solution. The formation of tetramers on HOPG could be a result of a lower mobility experienced by the molecules while on HOPG. The fibers are aligned along $\langle 11\bar{2}0 \rangle$ or $\langle 01\bar{1}0 \rangle$ directions resulting from the presence of more than one alkyl chain in a molecule and the symmetry of tetramer/hexamer units.

6.5. (Alkoxy)benzoylhydrazines

To understand the effect of molecular geometry and the influence of secondary hydrogen bonding in the columnar order, the amide group (NH_2) is replaced by a hydrazide group (NHNH_2). In solution, the secondary hydrogen bonds are believed to facilitate ordering along the column direction. The number of alkoxy chains in the resulting hydrazide is also varied to elucidate whether the molecular geometry plays a role in the fiber formation of (alkoxy)benzoylhydrazides. That is, 3-chain, 2-chain and 1-chain (alkoxy)benzoylhydrazides are studied. Furthermore, a covalently bound analogue of the 2-chain alkoxy benzaamides, namely $\text{N,N}'$ -Bis[3,4-bis(alkoxy)benzoyl]hydrazide is investigated.

6.5.1. 3,4,5-Tris(dodecyloxy)benzoylhydrazine (3CH-12)

In this study, the 3CH-12 molecule often observed to show different morphologies on HOPG depending on the concentration of the solution. Optical microscopy, AFM and STM studies show that 3CH-12 fibers on HOPG are formed only from concentrated solutions while dilute solutions produce monolayer structures on HOPG. In general, the structural properties of thin films on surfaces depend on the film thickness. Example include thin films of combined LC polymer with mesogens exhibiting a disappearance of smectic order perpendicular to the surface when the film thickness is below 10 nm [226] and some molecules forming different layer packings such as the 'face-on' or 'edge-on' arrangement on HOPG [227, 228].

3CH-12 Monolayer

Fig. 6.24 shows a 3CH-12 molecule and a 3CH-12 dimer. The predominant morphology of 3CH-12 molecules on HOPG deposited from a dilute solution (4.26 wt.-% or less) is a layer structure (Fig. 6.25).

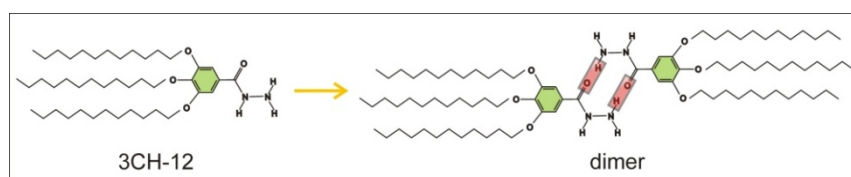


Fig. 6.24 3CH-12 molecule and its cyclic dimer

The observation of graphite superlattices during the investigation of 3CH-12 on HOPG, has been discussed in chapter 5. Based on the propositions made there, the origin of the layer structure seen on HOPG can be established. Furthermore, as shown in Fig. 6.26(a) and (b), which are images from two different measurements, show the formation of monolayers in real time. This unambiguously excludes the moiré pattern argument in the first place.

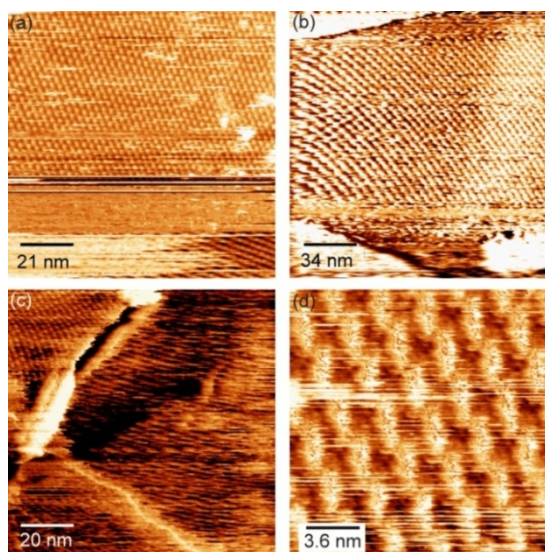


Fig. 6.25 (a-f) STM images of 3CH-12 on HOPG deposited from dilute solutions (4.26 wt.-% or less) forming monolayer structures. Image (f) is obtained by scanning over a small region within (a). Imaging parameters (a) 0.34 V, 0.66 nA;(b) 1.18 V, 0.66 nA;(c) 1.36 V, 0.67 nA;(d) 0.37 V, 0.66 nA.

Another fact that excludes moiré origin is that, on more than one occasion, a change in the monolayer appearance has been observed as shown in Fig. 6.25(d) with the bright blobs changing to some elliptical features but still retaining the periodicity. In the case of graphite moiré, which is predominantly an electronic effect, such changes are not expected.

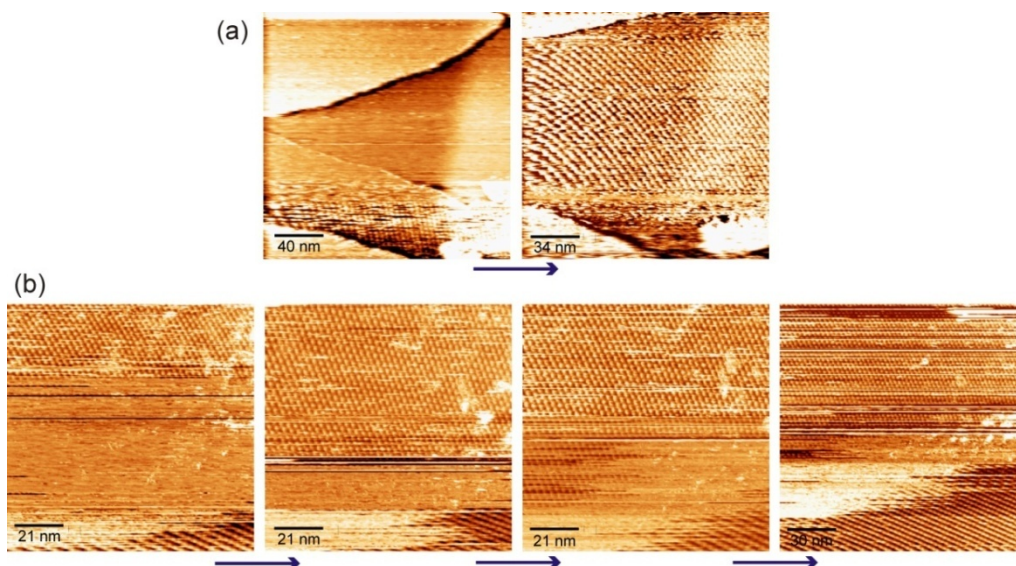


Fig. 6.26 (a) and (b) represent two different measurements showing the formation of monolayer of 3CH-12 on HOPG.

The unit cell of the 3CH-12 monolayer on HOPG is hexagonal with $a=b= 3.2$ nm. On close inspection, it can be seen that each bright blob in Fig. 6.27 actually consists of two separate spots each of dimension $1.4 \text{ nm} \times 0.9 \text{ nm}$.

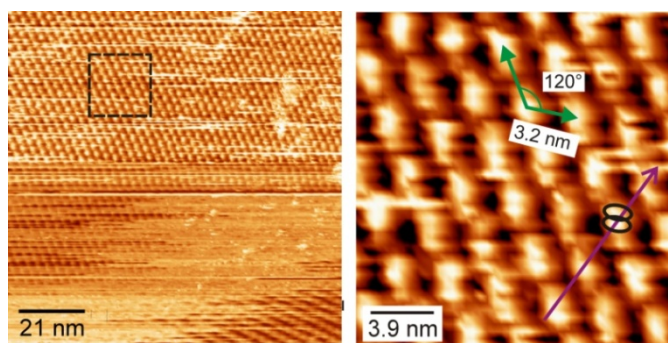


Fig. 6.27 (Left) 3CH-12 monolayer on HOPG. Area within the rectangle is enlarged and shown on the right. Unit cell parameters are $a=b=3.2$ nm, $\theta(a,b)=120^\circ$

A rotation of 30° or 120° is observed between adjacent domains of 3CH-12 molecules on HOPG as shown in Fig. 6.28. This is contrary to the general trend of monolayers formed from molecules possessing alkyl chains showing 60° or 120° angles between domains.

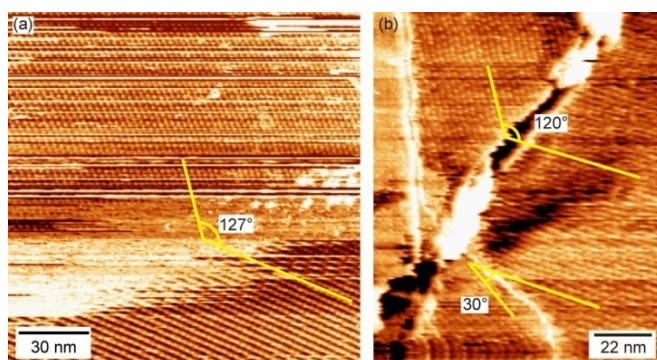


Fig. 6.28 Domain formation of 3CH-12 monolayer on HOPG influenced by the underlying graphite lattice.

The formation of such domains is most unlikely or even impossible for a moiré pattern (graphite superlattice) and hence, this fact further supports the origin of these structures to the adsorbate.

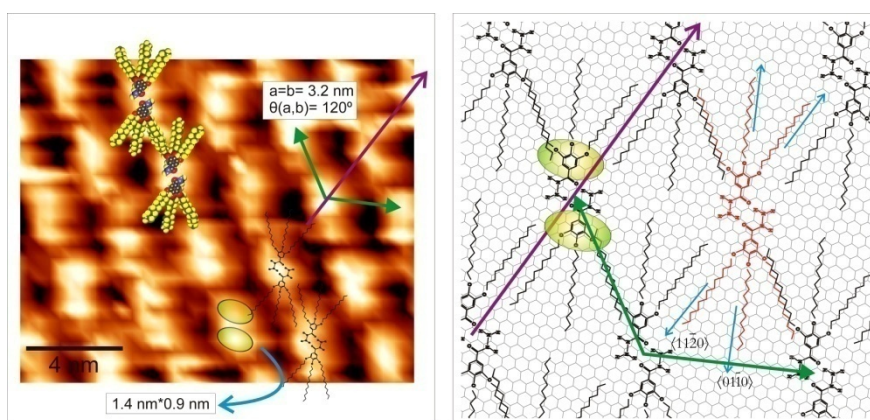


Fig. 6.29 Monolayer structure of 3CH-12 on HOPG with a ‘face-on’ arrangement. Two alkyl chains from each molecule are attached to the graphite while the other dangling alkyl chain is responsible inter-dimer interaction.

The proposed monolayer structure formed by 3CH-12 molecules on HOPG is shown in Fig. 6.29. A single bright blob in the STM image represents the two aromatic regions of a dimer separated by a small narrow dark region. This is shown as two ellipses. The ellipses are inclined to the direction of the array of spots (represented by the arrow) approximately by 30° and there is a relative shift between the two ellipses against the direction of the array of spots.

Two alkyl chains from each molecule indicated by blue arrows are attached to the graphite surface as shown with one having a commensurate adsorption along the $\langle 11\bar{2}0 \rangle$ and the other one with a weaker interaction along the $\langle 01\bar{1}0 \rangle$ direction. This explains the observation of rotation of domains by 30° as which one of the two alkyl chains follow either of the direction is quite arbitrary. Because these two directions differ by an angle of 30° , the minimum relative rotation possible between domains is 30° or multiples of it rather than multiples of 60° . The other alkyl chains in the dimer which are diagonally opposite, are expected to be dangling, and may interact with alkyl chains of the neighboring dimers.

3CH-12 Fiber

The OM image (Fig. 6.30(a)) shows 3CH-12 needle-like crystallites and their clustering. This is probably a gel-like state due to the high concentration used and the molecules are densely populated over the whole substrate surface. The sample is heated to make an isotropic solution prior to deposition and the drop of solution deposited soon partially get solidifies to a highly viscous fluid with a gel-like appearance. AFM images also support this observation with a visible network of fiber bundles.

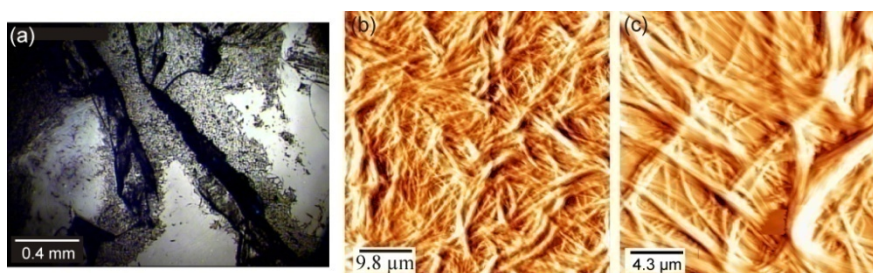


Fig. 6.30 (a) Optical microscopy image showing the needle-like crystallites of 3CH-12 on HOPG formed from concentrated solutions. (b) and (c) AFM images showing network of fiber bundles.

The effect of concentration, temperature and cooling rate on the morphology of 3CH-12 has not been investigated in detail. However, from a number of trials, it is clear that a fibrillar morphology is observed only for concentrated solutions. The only observation of a fiber for a dilute solution is shown in Fig. 6.31(a) that exemplifies the lack of a perfect linear order. For this reason, in order to image isolated, single fibers by STM, first a drop of the concentrated solution is deposited on HOPG and after a few hours, a drop of the solvent is allowed to slide over the surface to remove excess molecular aggregates. This leaves some fibers on the HOPG substrate avoiding multilayer and fiber bundle formation

while individual fibers can be imaged. However, the fibers seem to be highly unstable and often perturbed by the tip motion during STM imaging at small scan ranges strongly hindering high resolution imaging.

Some of the STM images of 3CH-12 fibers formed on HOPG are shown in Fig. 6.31. The thinnest linear chains (Fig. 6.31(f)) have a periodicity of 1.09 ± 0.01 nm and a height 0.4 to 0.5 nm. The bright blobs have the dimension of $1 \text{ nm} \times 0.9 \text{ nm}$ with the longer extension along the fiber axis. The width of the fiber is 1.6 nm. The bright blobs have a very different arrangement compared to those of 3CB-n fibers.

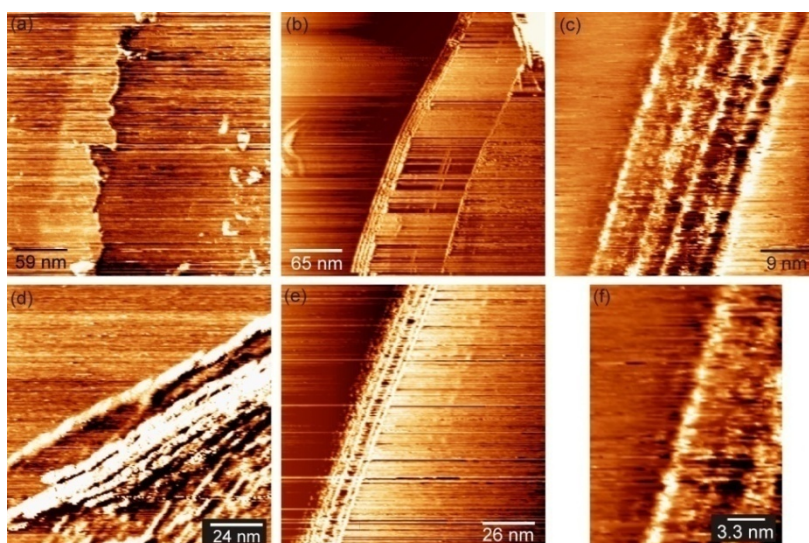


Fig. 6.31 (a) STM image of a 3CH-12 fiber formed from dilute solution (imaging parameters are). (b)-(f) Fibers formed from concentrated solutions. The fibers are unstable and easily perturbed by the tip motion during imaging. Imaging parameters (a) 1.06 V and 0.66 nA; (b-f) (1.03- 1.05) V, (0.47- 0.49) nA.

The comparatively smaller period of the bright blobs along the fiber may indicate an inter-dimeric π - π interaction being responsible for the ordering along the column.

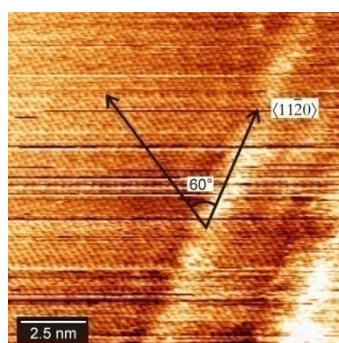


Fig. 6.32 STM image showing both a single-strand 3CH-12 fiber and the graphite lattice in one frame, showing the alignment of the fiber with respect to the graphite substrate. Tunneling conditions are $V = 1.04$ V and $I = 0.45$ nA.

This may plausibly lead to a partial overlap of the aromatic ring of a dimer with the aromatic ring of a subsequent dimer, forming an extended conjugated and delocalized π -system. The fiber is aligned along the $\langle 11\bar{2}0 \rangle$ direction (Fig. 6.32).

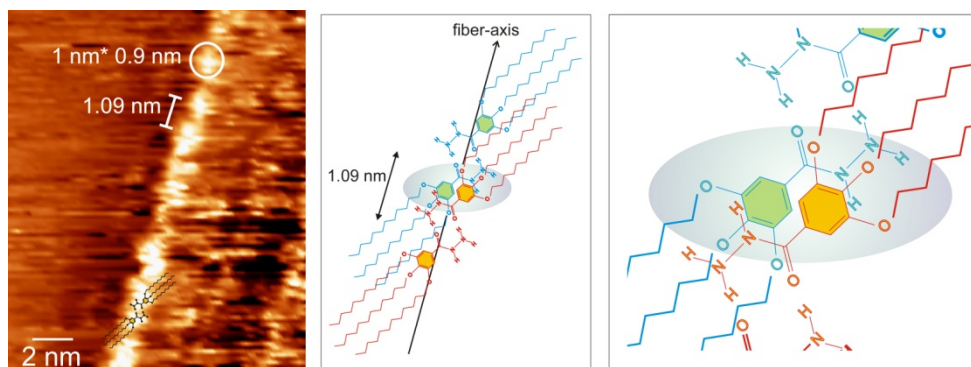


Fig. 6.33 Fiber formation of 3CH-12 arising from a partial overlap of the π -clouds ‘edge-on’ arrangement. The individual 3CH-12 dimers are inclined with respect to the fiber axis to allow for this overlap.

The proposed model for a single 3CH-12 fiber is shown in Fig. 6.33. It cannot be precisely discerned from the STM image whether the aromatic cores have a face-on or edge-on orientation with respect to the graphite surface but it seems to have an intermediate configuration considering the presence of alkyl chains. The molecules should be inclined with the direction of the fiber axis in order to be commensurate with distance measurements in the STM image and the tilting avoids over-crowding of alkyl chains. This configuration may also favor secondary hydrogen bonding. The formation of such a configuration may require a higher density of molecules on the surface; otherwise, molecules will form a monolayer with a flat face-on arrangement as described above. At least one alkyl chain can be expected to be completely or partially attached to the graphite surface.

At lower concentrations, the molecules are free to move on the surface and stabilized by the formation of a monolayer. In both cases, the basic units involved are 3CH-12 dimers. It is probable that the 3CH-12 fibers seen on HOPG are pre-organized in solution itself to produce a columnar structure. The 3CH-12 molecules’ tendency to aggregate through π - π interactions may be also due to its poor solubility in 1,2,4-trichlorobenzene. Unlike in the case of 3CB-*n* molecules, 3CH-*n* molecules are not able to form hydrogen-bonded tetramers or hexamers due to the spatial extension of the hydrazine moiety at the ‘wedge-tip’. Although the additional hydrogen atom does not prevent dimer formation, it is not particularly amiable for tetramer or higher combinations due to the presence of three alkyl chains per molecule.

Conclusion: 3CH-12 Monolayer and Fiber

The monolayer structure on HOPG is produced as a result of alkyl chain interactions with graphite and via inter-alkyl forces among dangling alkyl chains. The inability of 3CH-12 to

form long chain fibers and their lower stability can be attributed to the weak inter-dimer π - π interactions being responsible for the holding forces along fiber axis. The aggregation of the needle-like crystallites on HOPG from concentrated solutions could be resulting from lateral secondary hydrogen bonding. The monolayer structure might exclusively be a surface-supported effect whereas the fibers may preexist in solution. In both the monolayer and fiber, the basic building block is dimer and no trimer or tetramer presence can be discerned from the STM images. This is also the reason why the fibers possess a very different structure from 3CB-n fibers. The additional hydrogen atom (that is from hydrazine) that is designed for ordering along columns through face-to-face stacking of discs seems redundant for fiber formation on HOPG.

6.5.2. 4-(decyloxy)benzoylhydrazine (1CH-10)

This molecule is a benzoylhydrazine with just one alkoxy chain attached to it (Fig. 6.34), the alkyl chain length is 1.12 nm. In contrast to 3CH molecule, 1CH has less number of alkyl chains. This allows for tetramer formation.

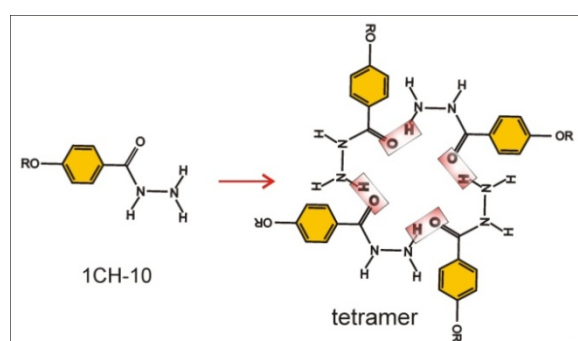


Fig. 6.34 1CH-10 molecule and the formation of a tetramer by hydrogen bonded cyclic network.

It has a structure with three strands (top-view) but at places, there are four strands visible (Fig. 6.35).

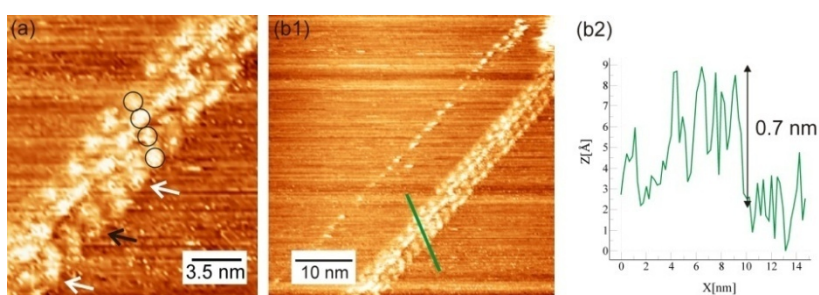


Fig. 6.35 (a) A 1CH-10 fiber containing six single-strands. (b2) Height profile along the green line in (b1).

Unlike for the three-strand 3CB-10 fiber, the three-strand fiber of 1CH-10 has the same width for all the strands, presumably a result of only tetramer units being involved in the fiber formation. Due to this reason, although the alkyl chain length remains the same in both molecules, 1CH-10 three-strand fiber has a smaller width of 6 nm (6.6 nm for 3CB-

10). The heights of individual strands in the fiber differ slightly with the maximum height of the strands being ~ 0.7 nm, which in comparison is lower than that of the 3CB-n fibers. This is again due to the presence of only tetramers and no hexamer units involved in fiber formation. The absence of hexamer units is presumably a consequence of space requirements demanded by the additional hydrogen atoms of NHNH_2 compared to NH_2 for the 3CB-n molecule.

Fig. 6.36(a) is an STM image showing one isolated and three closely placed single-strand fibers. The four lateral bright blobs in the individual periodic units in the three-strand fiber do not have the same brightness, and at some places only three bright blobs can be seen. It seems that there are a total of six strands constituting this fiber.

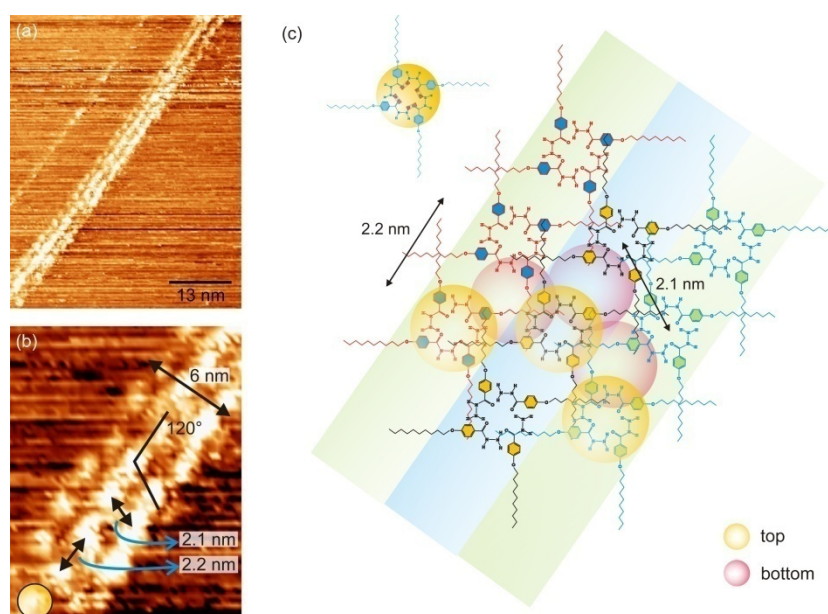


Fig. 6.36 (a) STM image showing one single isolated fiber and a three-strand fiber of 1CH-10. (b) Linear dimensions of the fiber, periodicity-2.2 nm, lateral separation between fibers-2.1 nm. (c) 2-D model of three-strand fiber. The alkyl chains are actually dangling and do not lie as depicted in the 2-D drawing. (see inset of (c)). Imaging parameters used for the STM image are 1.29 V and 0.69 nA.

A single-strand is formed by a linear array of 1CH-10 tetramers. Although the 1CH-10 molecule possesses only one alkoxy chain, the tetramer formation makes it possible to have inter-strand interactions in a three-strand fiber via alkyl chains. The three-strand fiber structure of 1CH-10 molecules is identical to the 3CB-n three-strand fiber (refer Fig. 6.23) in the sense that 1CH-10 molecules form tetramers and the fiber gets stabilized by inter-strand interactions via alkyl chains. However, the number of strands is higher (six) for 1CH-10 due to the lack of sufficient alkyl chains and hexamer units. The periodicity of bright blobs along the fiber is 2.2 nm. The lateral distance between strands is 2.1 nm and the individual bright blobs are composed of four smaller spots each of them having 0.3 to 0.5 nm dimensions. The 2-D model is shown for a three-strand fiber, with three strands of 1CH-10 on the top. The height differences in the chains suggest that in the 3-D picture, the actual arrangement should be with three more single strands lying below. The alkyl

chains of the lower tetramers that do not participate in the inter-strand interactions may be attached to the graphite. Due to the resemblance of basic structures between 3CB-n and 1CH-12 fibers, it can be concluded that many of the properties of 1CH-10 fiber on HOPG should be similar to 3CB-n fiber.

6.5.3. 3,4-bis(decyloxy)benzoylhydrazine (2CH-10)

An extension of the 1CH-10 molecule with one more alkoxy chain at the tail is a 2-chain hydrazide namely 3,4-bis(decyloxy)benzoylhydrazide. Only few experiments were done for this molecule and a high resolution STM image of a fibrous structure observed is shown in Fig. 6.37.

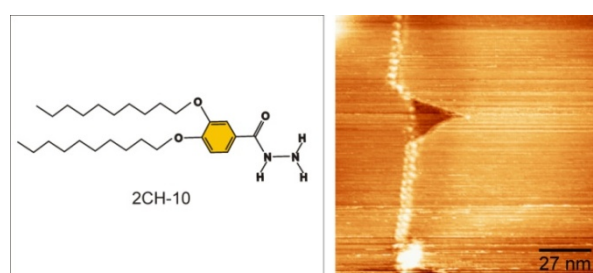


Fig. 6.37 Structure of the 2CH-10 molecule and the STM image of a fiber-like structure observed on HOPG with 2CH-10 molecules deposited on HOPG.

Large scan area images show that the graphene layer is highly perturbed presumably during HOPG cleavage.

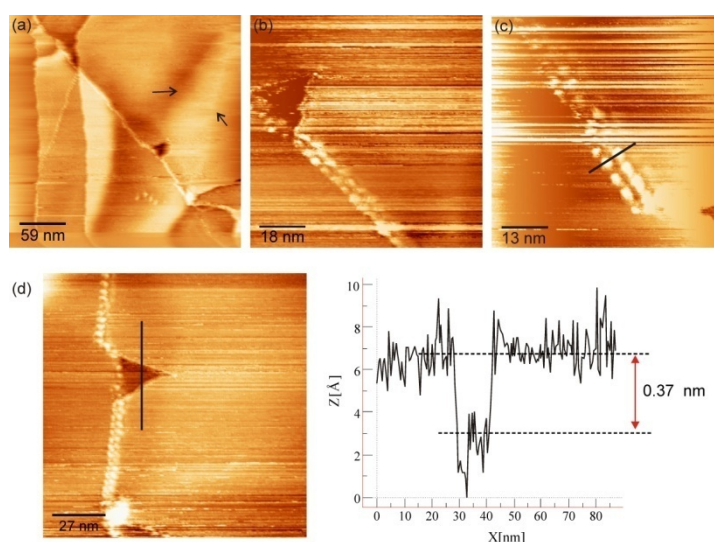


Fig. 6.38 (a) Large area scans of the region with the fiber-like structure. In (a) ‘buckling’ of the flakes of underlying graphite layer can be seen (indicated by arrows). (b) and (c) shows the appearance of a replica-type parallel arrangement of bright spots similar to graphitic fibers. (d) A pit on graphite layer and the corresponding line profile. The pit depth is 0.37 nm comparable to the graphite inter-layer separation of 0.34 nm. Imaging parameters (a) 1.21 V, 0.6 nA; (b-d) 1.7 V, 0.6 nA.

The linear structure observed appears to have an arrangement of bright blobs as if they are replicas stacked in a parallel fashion (indicated by the solid black line) in Fig. 6.38(c). Due to these reasons, the origin of this fibrous structure can be attributed to graphene distortions (see chapter 5). The pit formed on HOPG has a depth 0.37 nm very close to the inter-layer separation of graphite (0.34 nm). The pit formation has created a tearing of the graphene layer and the boundary between the torn-off portions gives an illusionary fiber-like appearance as in the case of a grain boundary [187].

6.5.4. N,N'-Bis[3,4-bis(decyloxy)benzoyl]hydrazide (2CB'-10)

This molecule can be regarded as a covalently bound analogue of alkoxy benzamide. From literature, it is known that symmetrically substituted methyloxy-3CB'-1 and ethyloxy-3CB'-2 hydrazides form crystalline compounds that melting above 177 °C, while higher derivatives formed a columnar disordered (C_{hd}) mesophase [101]. The clearing temperature decreases continuously with increasing length of the alkoxy chains from $T_c=209$ °C (n=3) to $T_c=141$ °C (n=14). X-ray data reveal that the number of molecules per column cross-section is two, forming a hydrogen-bonded cyclic dimer. Dimers are not flat but their projection perpendicular to the column axis is nearly circular in shape, obeying the symmetry condition for the formation of hexagonal superstructures. The absolute values of the clearing enthalpies and entropies of 3CB'-n are 60% larger than for the analogous 3CB-n compounds, indicating a stronger intermolecular interaction. The linear N,N'-bis[(4'-decyloxy)benzoyl]hydrazide (1CB'-10) is a calamitic mesogene (rod-shaped) as can be expected from its linear shape while N,N'-Bis[3,4-bis(decyloxy)benzoyl]hydrazide (2CB'-10) shows a hexagonal disordered columnar mesophase. The columnar structure is identical in all cases.

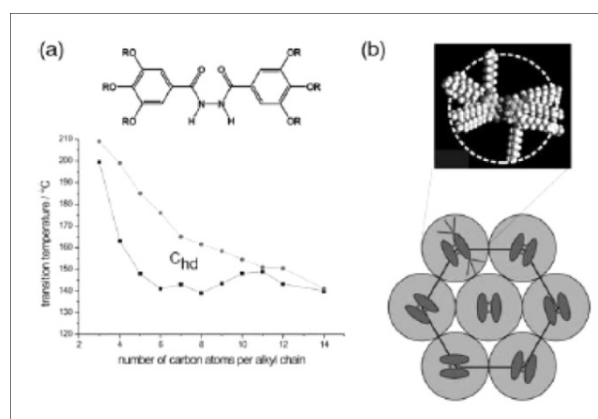


Fig. 6.39 (taken from [110]) transition temperatures of N,N'-Bis[3,4,5-tris(alkoxy)benzoyl]hydrazides, N,N'-3CH-n and schematic figure of mesogene arrangement in the C_{hd} phase.

An STM image of two strands of N,N'-Bis[3,4-bis(decyloxy)benzoyl]hydrazide (2CB'-10) fibers on HOPG is shown in Fig. 6.40. The width of the thicker fiber is 5.6 nm. The heights of individual bright blobs in the fiber are not the same, with an apparent maximum height over 0.8 nm.

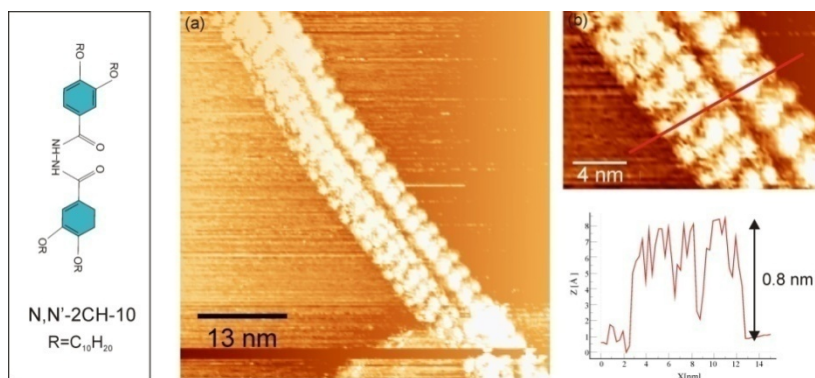


Fig. 6.40 (left) A 2CB²-10 molecule. (a) STM image of a fiber formed on HOPG. (b) Height profile (below) of the fiber along the red line in image (b). Imaging parameters are $V = 1.3$ V and $I = 0.6$ nA.

The distances and sizes of spots are illustrated in Fig. 6.41(c). Eight elliptical bright blobs are arranged side-by-side in a zig-zag manner in each periodic unit of the fiber. The periodicity is 2.5 nm along the fiber axis and the distance between ellipses in adjacent strands is 1.5 nm.

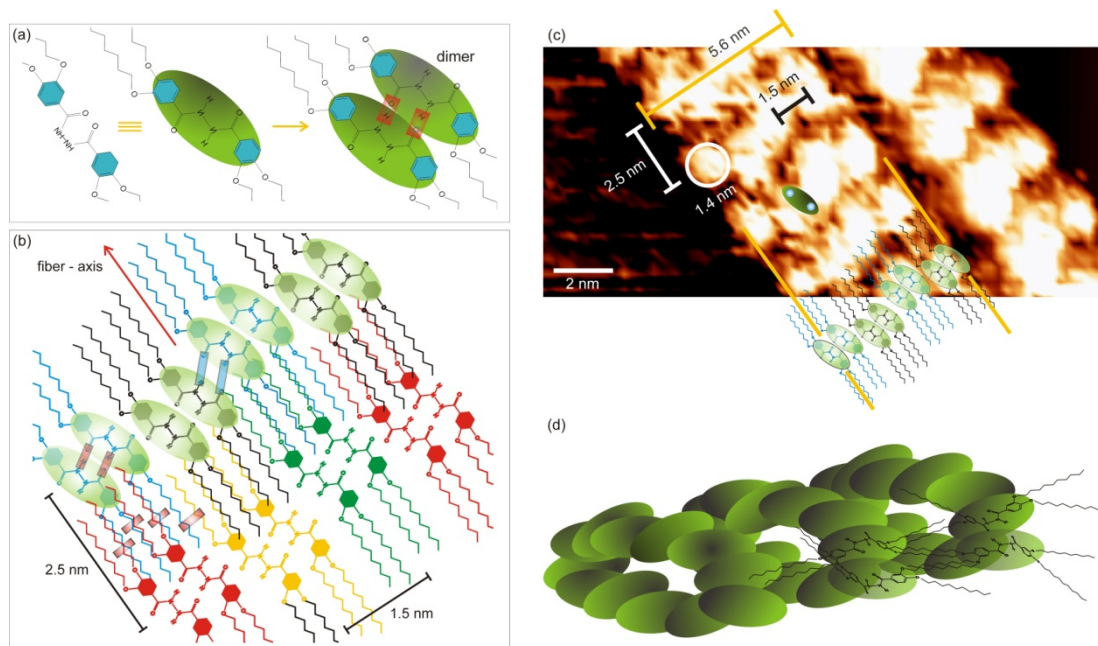


Fig. 6.41 (a) Formation of a 2CB²-10 dimer. (b) The zig-zag arrangement of the dimers in the fiber (shown on a plane) showing alkyl chain interactions between dimers along fiber axis. In a 3-D representation, the aromatic units do not lie on a plane parallel to HOPG(0001) surface. (c) STM image with molecules and dimers superposed. (d) The 3-D structure of the fiber on HOPG with distance between top and bottom ellipses exaggerated for ease of visualization.

The proposed structure of the 2CB²-10 fiber is shown in Fig. 6.41. The periodicity of the basic building units (consisting of eight ellipses) allows for an optimum interdigitation of the dangling alkyl chains between dimers in subsequent units. There is no lateral interaction between dimers in the same unit via alkyl chains. Each dimer in a unit (blue) interacts with its immediate predecessor (red) as well as with the dimer next to it (yellow)

via alkyl chains (indicated by red rectangles over alkyl chains). Thus inter-dimer alkyl chain hydrophobic interactions with immediate neighbors in the preceding unit play an important role in the ordering along the column axis. Due to the height difference observed, it is clear that all ellipses are not simply lying 'flat' on HOPG but a model like in Fig. 6.41(c) can be expected. The hydrogen bonded dimers are closely packed in a steric influenced manner. Although it is shown in Fig. 6.41(c) with the aromatic parts lying parallel to the HOPG surface, the actual configuration is illustrated in Fig. 6.41(d), where the molecules in a dimer do not lie on the same plane but with a cross-like configuration represented by tilted ellipses. The hydrogen bonded dimers are arranged in zig-zag which is the result of a closely packed steric commensurate arrangement. This is a consequence when the fiber is formed from free dimers through alkyl chain interactions. The fiber is stabilized by inter-dimer alkyl chain van der Waals interactions occurring only along the fiber direction. As a result, stable fibers of 2CHd-10 should be expected at a higher number of strands in comparison to fibers formed through tetramer strands. There is no alkyl chain interaction between the dimers of the same periodic unit. The inter-strand interaction occurs along the fiber direction

Chapter 7

Conclusion

This thesis is an attempt to delve into details of molecular self-assembly of some amphiphilic molecules on the cleaved surface of highly oriented pyrolytic graphite (HOPG), with due emphasis on their low-dimensional architectures. Two types of molecular systems capable of forming supramolecular architectures through self-assembly (SA) have been studied. The first one is a monolayer structure (2-D SA) of a simple long-chain fatty acid on HOPG and the second and central theme of the thesis involves the fibrous structures formed on HOPG from some wedge-shaped liquid crystalline molecules. The wedge-shaped molecules often form isolated or bundled linear structures (1-D SA) on HOPG. This is one of the first studies elucidating the structural arrangement of isolated organic nanofibers particularly of the class of liquid-crystalline columnar phase with resolution down to the sub-molecular level. Another issue addressed is related to the study of adsorbate columnar structures on HOPG. This is about the close resemblance of the adsorbate structures with innate graphene manifolds usually produced as a result of cleavage and weak inter-layer bonding in graphite. Some simple and straightforward methods have been devised to differentiate them from adsorbate structures when aiming at an unambiguous identification of the origin of 1-D and 2-D structures seen on HOPG (0001).

Although the morphology of arachidic acid on HOPG has been studied before, it is for the first time that a precise determination of the structure of the monolayer has been achieved. The method used is not based on the analysis of calibrated STM images but uses the periodicity of the graphite surface lattice for an intrinsic calibration, thus excluding the possibilities of erroneous effects such as thermal drift or measurement errors. The deviation of registry between alkyl chains and the graphite lattice results in peculiar contrast features in STM imaging in the form of an asymmetric appearance of the molecules, periodic contrast enhancement, and a characteristic moiré pattern observed under certain experimental conditions. Utilizing the information from high-resolution STM images incorporated with the underlying mechanism responsible for image contrast (moiré pattern), the monolayer structure is determined. This gives an oblique unit cell for the monolayer, with dimensions of $0.936 \text{ nm} \times 2.83 \text{ nm}$ (85° angle), allowing for an unrelaxed O-O distance of 0.31 nm between carboxylic dimers. Furthermore, it has been shown that the arachidic acid molecules crystallize into enantio-pure molecular domains having unit cells that are tilted by 10° with respect to each other.

The central part of this work was elucidating the molecule-by-molecule architectures of some organic nanofibers formed on HOPG from a class of benzamide liquid crystalline molecules. By suitable modification of the molecules, the role of the molecular geometry and intermolecular interactions in the formation of these supramolecular columnar structures on HOPG has been investigated with due emphasis on attaining sub-molecular resolution in each case. No information could be discerned from the STM images supporting a ‘stacking of discs’ –like architecture (as in solution), rather fiber formation on HOPG relies on a closure of dimer, tetramer or hexamer loops interconnected by alkyl chains. Molecules 3CB-n, 1CH-10 and 2CB'-10 follow this route. The alkyl chains play a crucial role in the ordering of strands along and against the fiber axis. Less stable fiber structures on HOPG are also observed for molecules such as 3CH-12 where inter-dimer interactions depend on π - π interactions, with alkyl chains playing a minor role. The hydrophobic HOPG surface does not seem to have any strong effect in altering fiber structures but alkyl chain-graphite interactions ‘flatten’ the fiber-cross section. In contrast to their solution counterparts with rectangular or hexagonal column cross-section, fibers formed on the hydrophobic HOPG show a semi-cylindrical cross-section.

By varying the alkyl chain length by two methylene units, the fiber architecture on HOPG of the 3CB-n has been altered and the role of alkyl chains in the formation of supramolecular fibers could be established. This also provides with the plausible position of alkyl chains in the STM images. The basic fiber structure does not change for 3CB-n (n=8, 10) molecules with different alkyl chain lengths, but is manifested as a modification in their periodicity and lateral distances along and against the fiber axis. An increase in the alkyl chain length is immediately manifested as an increase in the lateral direction, simultaneously providing a relaxation along fiber axis and thereby resulting in a reduction of the periodicity along the axis. The reduction in the periodicity may also mean a higher interdigitation of alkyl chains. Retaining the number of alkoxy chains intact but modifying the head group drastically changes the molecule behavior on HOPG. While the formation of 3CB-n (n=8,10) fibers is independent of the concentration, 3CH-12 molecule form monolayers on HOPG from a dilute solution as well as needle-like crystallites and fibers from a concentrated solution. Although, in general, the presence of additional hydrogen atoms is expected to improve column ordering (as in solution) through secondary hydrogen bonds, 3CH-12 molecules fail to form long-chain fibers. The secondary hydrogen atoms that are believed to promote the column ordering in solution seem redundant for the HOPG surface supported fiber formation. Subsequently, retaining the same head group (NHNH₂), the number of alkyl chains is varied to understand the influence of molecular geometry on fiber formation. The more seriously pursued molecule in this section is 3CH-12, which has the same number of alkyl chains as the 3CB-n, shows both monolayer as well as fibrillar morphologies on HOPG depending on the concentration of the solution from which the molecules are deposited. On the other hand, the 1CH-10 molecule, although having just one alkoxy chain per molecule, is able to form fibers similar to 3CB-n. This is attributed to its ability to form tetramers, thus overcoming

its lack of a favorable geometry and insufficient number of alkyl chains for inter-strand interactions. Although in comparison to a three-chain benzamide (3CB) molecule, 1CH-10 possesses a bulky head group (i.e. NH_2 to NHNH_2) that can forbid the formation of tetramers, the lesser number of alkyl chains of 1CH-10 provides a facile alternative to tetramer formation. The effect of geometry is evident with a covalent analogue of 2CB-n benzamide namely 2CB'-10 which form well-ordered linear chains with dimers as the basic units. Due to the extended spatial structure of 2CB'-10 compared to a simple two-chain(alkoxy)benzamide (2CB-10), 2CB'-10 molecules are not able to form tetramers. The molecules first organize themselves into hydrogen-bonded dimers and thereupon the dimers interacting via van der Waals interaction of their dangling alkyl chains to produce a linear structure. The fiber is stabilized by inter-dimer alkyl chain van der Waals interactions occurring only along the fiber direction which leads to a requirement of a larger number of units (dimer) needed for stable fiber geometry compared to those of fibers formed from tetramers. The very basic unit in the 2CB'-10 fiber is a dimer, which is also the geometrically most plausible configuration. For this reason, the fiber structure of the 2CB'-10 is distinctly different from 3CB-n fibers.

The most often observed fiber geometry for 3CB-n and 1CH-10 is a three-strand structure. This stable structure results from inter-strand interactions between four strands (one strand underneath) through inter- and intra-hexamer/tetramer units via alkyl chain interdigitation. The 3CH-12 fibers heavily depend on π - π interactions to produce a linear arrangement and require a concentrated solution to initiate such packing. The geometry of the molecule is a major obstacle for 3CH-12 for fiber formation. The presence of additional hydrogen atoms and the 'crowding' of three alkyl chains make 3CH-12 less favorable for tetramer formation and the easiest possibility is to form a monolayer with dimers lying flat on HOPG. The observed orientation of most fiber species on HOPG along either the $\langle 01\bar{1}0 \rangle$ or the $\langle 11\bar{2}0 \rangle$ direction can be attributed to more than one alkyl chains participating in the interaction and the symmetry of the building units (tetramers and others) that obliges the respective alkyl chain to occupy one of these directions alternatively. In short, fiber formation on the HOPG surface is highly favored when the molecules can form hydrogen bonded-ring networks or with a dimer geometry suitable for inter-alkyl chain interactions. For molecules lacking a favorable geometry or deficient in their number of alkyl chains, fiber formation is possible by association of individual molecules to form higher combinations such as tetramers, which can compensate for the inadequacies such as a lack of sufficient number of alkyl chains and leads to fiber formation on HOPG.

Bibliography

1. Whitesides, G.M., J.P. Mathias, and C.T. Seto, *Molecular self-assembly and nanochemistry: a chemical strategy for the synthesis of nanostructures*. Science (Washington, DC, United States), 1991. **254**(5036): p. 1312-19.
2. Joachim, C., J.K. Gimzewski, and A. Aviram, *Electronics using hybrid-molecular and mono-molecular devices*. Nature, 2000. **408**: p. 541-548.
3. Shaw, J.M. and P.F. Seidler, *Organic electronics: Introduction*. IBM Journal of Research and Development, 2001. **45**(1): p. 3-9.
4. Grätzel, M., *Photoelectrochemical cells*. Nature (London, United Kingdom), 2001. **414**(6861): p. 338-344.
5. Palmer, L.C. and S.I. Stupp, *Molecular Self-Assembly into One-Dimensional Nanostructures*. Accounts of Chemical Research, 2008. **41**(12): p. 1674-1684.
6. Barth, J.V., G. Costantini, and K. Kern, *Engineering atomic and molecular nanostructures at surfaces*. Nature (London, United Kingdom), 2005. **437**(7059): p. 671-679.
7. Barth, J.V., *Molecular architectonic on metal surfaces*. Annual review of physical chemistry, 2007. **58**: p. 375-407.
8. Kühnle, A., *Self-assembly of organic molecules at metal surfaces*. Current Opinion in Colloid and Interface Science, 2009. **14**: p. 157-168.
9. Smith, W.F., *Organic electronics - Self-assembly is ready to roll*. Nature Nanotechnology, 2007. **2**(2): p. 77-78.
10. Schenning, A. and E.W. Meijer, *Supramolecular electronics; nanowires from self-assembled pi-conjugated systems*. Chemical Communications, 2005(26): p. 3245-3258.
11. Mendes, P.M., A.H. Flood, and J.F. Stoddart, *Nanoelectronic devices from self-organized molecular switches*. Applied Physics a-Materials Science & Processing, 2005. **80**(6): p. 1197-1209.
12. Forrest, S.R., *The path to ubiquitous and low-cost organic electronic appliances on plastic*. Nature, 2004. **428**(6986): p. 911-918.
13. De Feyter, S., et al., *Supramolecular chemistry at the liquid/solid interface probed by scanning tunnelling microscopy*. International Journal of Nanotechnology, 2006. **3**(4): p. 462-479.
14. De Feyter, S. and F.C. De Schryver, *Two-dimensional supramolecular self-assembly probed by scanning tunneling microscopy*. Chemical Society Reviews, 2003. **32**(3): p. 139-150.
15. De Feyter, S. and F.C. De Schryver, *Self-assembly at the liquid/solid interface: STM reveals*. Journal of Physical Chemistry B, 2005. **109**(10): p. 4290-4302.
16. Amabilino, D.B., et al., *Monolayer self-assembly at liquid-solid interfaces. Chirality and electronic properties of molecules at surfaces*. Journal of Physics: Condensed Matter, 2008. **20**(18): p. 184003.
17. Elemans, J. and S. De Feyter, *Structure and function revealed with submolecular resolution at the liquid-solid interface*. Soft Matter, 2009. **5**(4): p. 721-735.
18. Abdel-Mottaleb, M.M.S., et al., *Self-assembly of tetrathiafulvalene derivatives at a liquid/solid interface - compositional and constitutional influence on supramolecular ordering*. Journal of Materials Chemistry, 2005. **15**(43): p. 4601-4615.
19. Hirst, A.R., et al., *High-Tech Applications of Self-Assembling Supramolecular Nanostructured Gel-Phase Materials: From Regenerative Medicine to Electronic Devices*. Angewandte Chemie-International Edition, 2008. **47**(42): p. 8002-8018.

20. Beyer, H., M. Muller, and T. Schimmel, *Monolayers of graphite rotated by a defined angle: hexagonal superstructures by STM*. Applied Physics a-Materials Science & Processing, 1999. **68**(2): p. 163-166.
21. Ebbesen, T.W. and H. Hiura, *Graphene in 3-dimensions - towards graphite origami*. Advanced Materials, 1995. **7**(6): p. 582-586.
22. Atamny, F., et al., *On the imaging mechanism of monatomic steps in graphite*. Applied Physics A: Materials Science & Processing, 2000. **71**(4): p. 441-447.
23. Chang, H.P. and A.J. Bard, *Observation and characterization by scanning tunneling microscopy of structures generated by cleaving highly oriented pyrolytic-graphite*. Langmuir, 1991. **7**(6): p. 1143-1153.
24. Guo, X.L. and D. Fujita, *Carbon nanowires spontaneously formed on surface of freshly cleaved highly ordered pyrolytic graphite wafer*. Japanese Journal of Applied Physics Part 1- Regular Papers Brief Communications & Review Papers, 2007. **46**(8B): p. 5568-5571.
25. Binnig, G., et al., *Tunneling through a controllable vacuum GAP*. Applied Physics Letters, 1982. **40**(2): p. 178-180.
26. Binnig, G., et al., *Surface studies by scanning tunneling microscopy*. Physical Review Letters, 1982. **49**(1): p. 57-61.
27. Binnig, G. and H. Rohrer, *Scanning tunneling microscopy - from birth to adolescence*. Reviews of Modern Physics, 1987. **59**(3): p. 615-625.
28. Binnig, G. and H. Rohrer, *In touch with atoms*. Reviews of Modern Physics, 1999. **71**(2): p. S324-S330.
29. Eigler, D.M. and E.K. Schweizer, *Positioning Single Atoms with a Scanning Tunneling Microscope*. Nature, 1990. **344**: p. 524-526.
30. Meyer, G., et al., *Controlled manipulation of atoms and small molecules with a low temperature scanning tunneling microscope*. Single Molecules, 2000. **1**(1): p. 79-86.
31. Otero, R., F. Rosei, and F. Besenbacher, *Scanning tunneling microscopy manipulation of complex organic molecules on solid surfaces*. Annual Review of Physical Chemistry, 2006. **57**: p. 497-525.
32. Foster, J.S., J.E. Frommer, and P.C. Arnett, *Molecular manipulation using a tunnelling microscope*. Nature, 1988. **331**(6154): p. 324-326.
33. Gao, H.J. and L. Gao, *Scanning tunneling microscopy of functional nanostructures on solid surfaces: Manipulation, self-assembly, and applications*. Progress in Surface Science, 2010. **85**(1-4): p. 28-91.
34. Sleator, T. and R. Tycko, *Observation of individual organic molecules at a crystal surface with use of a scanning tunneling microscope*. Physical Review Letters, 1988. **60**(14): p. 1418-1421.
35. Lide, D.R. and H.P.R. Frederikse, *CRC Handbook of Chemistry and Physics, 83th Edition*. 2003: CRC Press, Boca Raton.
36. Sugita, S., Y. Mera, and K. Maeda, *Origin of low frequency noise and 1/f fluctuations of tunneling current in scanning tunneling microscopes*. Journal of Applied Physics, 1996. **79**(8): p. 4166-4173.
37. Bychikhin, S.A., et al., *Scanning tunneling microscope - A nanoelectronic measuring instrument*. Measurement Techniques, 1998. **41**(4): p. 383-388.
38. Aguilar, M. and M. Pancorbo, *Noise characterization in scanning-tunneling-microscopy (STM)*. Pattern Recognition Letters, 1994. **15**(10): p. 985-992.
39. Bardeen, P.p.B.p., *Tunneling from a Many-Particle Point of View*. Physical Review Letters, 1961. **6**: p. 57-59.
40. Tersoff, J. and D.R. Hamann, *Theory and Application for the Scanning Tunneling Microscope*. Physical Review Letters, 1983. **50**: p. 1998-2001.

41. Tersoff, J. and D.R. Hamann, *Theory of the scanning tunneling microscope*. Physical Review B, 1985. **31**(2): p. 805-813.
42. Neaton, J.B., M.S. Hybertsen, and S.G. Louie, *Renormalization of molecular electronic levels at metal-molecule interfaces*. Physical Review Letters, 2006. **97**.
43. Masel, R.I., *Principles of Adsorption and Reaction on Solid Surfaces*. Auflage: 1 (März 1996) ed. Wiley series in chemical engineering. Vol. XIV, 804 S. : Ill., graph. Darst. ; 26 cm: Wiley & Sons. Gebundene Ausgabe: 824 Seiten.
44. Besenbacher, F., *Scanning tunnelling microscopy studies of metal surfaces*. Reports on Progress in Physics, 1996. **59**(12): p. 1737-1802.
45. Chen, C.J., *Introduction to scanning tunneling microscopy*. 2. ed. ed. Monographs on the physics and chemistry of materials. Vol. LXIII, zahlr. Ill. und graph. Darst. ; 24 cm. 2008, Oxford: Oxford Univ. Press, 2008. 423 S.
46. Hansma, P.K. and J. Tersoff, *scanning tunneling microscopy*. Journal of Applied Physics, 1987. **61**(2): p. R1-R23.
47. Eigler, D.M., et al., *imaging xe with a low-temperature scanning tunneling microscope*. Physical Review Letters, 1991. **66**(9): p. 1189-1192.
48. Faglioni, F., et al., *Theoretical description of the STM images of alkanes and substituted alkanes adsorbed on graphite*. Journal of Physical Chemistry B, 1997. **101**(31): p. 5996-6020.
49. Yang, Y.L., et al., *Effects of intermolecular interactions on the controlled assembly of organic monolayers: an STM study*. Surface and Interface Analysis, 2006. **38**(6): p. 1039-1046.
50. Giancarlo, L.C. and G.W. Flynn, *Scanning tunneling and atomic force microscopy probes of self-assembled, physisorbed monolayers: peeking at the peaks*. Annual Review of Physical Chemistry, 1998. **49**: p. 297-336.
51. Ramos, M.M.D., *can stm be used to image molecules on surfaces*. Journal of Physics-Condensed Matter, 1993. **5**(18): p. 2843-2848.
52. Ouyang, H., R.A. Marcus, and B. Kallebring, *scanning tunneling microscopy theory for an adsorbate: application to adenine adsorbed on a graphite surface*. Journal of Chemical Physics, 1994. **100**(10): p. 7814-7824.
53. Nejoh, H., *visible mechanism of liquid-crystals on graphite under scanning tunneling microscopy*. Applied Physics Letters, 1990. **57**(27): p. 2907-2909.
54. Richter, S. and Y. Manassen, *Aspects of molecular imaging with a scanning tunneling microscope*. Journal of Physical Chemistry, 1994. **98**(11): p. 2941-2949.
55. Lee, H.S., S. Iyengar, and I.H. Musselman, *Bias-dependent STM image contrast study of phenyloctadecyl ethers physisorbed onto highly oriented pyrolytic graphite*. Langmuir, 1998. **14**(26): p. 7475-7483.
56. Mizutani, W., et al., *voltage-dependent scanning tunneling microscopy images of liquid-crystals on graphite*. Applied Physics Letters, 1990. **56**(20): p. 1974-1976.
57. Florio, G.M., et al., *Self-Assembly of Small Polycyclic Aromatic Hydrocarbons on Graphite: A Combined Scanning Tunneling Microscopy and Theoretical Approach*. Journal of Physical Chemistry B, 2005. **109**(10): p. 4520-4532.
58. Lackinger, M., et al., *Tunneling voltage polarity dependent submolecular contrast of naphthalocyanine on graphite. A STM study of close-packed monolayers under ultrahigh-vacuum conditions*. Journal of Physical Chemistry B, 2004. **108**(7): p. 2279-2284.
59. Mizutani, W., et al., *Tunneling through a deformed potential*. Ultramicroscopy, 1992. **42**: p. 236-241.
60. Walba, D.M., et al., *Near-Atomic Resolution Imaging of Ferroelectric Liquid Crystal Molecules on Graphite by STM*. Science, 1995. **267**(5201): p. 1144-1147.

61. Lazzaroni, R., et al., *Electronic structure of molecular van der Waals complexes with benzene: Implications for the contrast in scanning tunneling microscopy of molecular adsorbates on graphite*. Journal of Chemical Physics, 1997. **107**(1): p. 99-105.
62. Spong, J.K., et al., *Contrast mechanism for resolving organic molecules with tunnelling microscopy*. Nature, 1989. **338**(6211): p. 137-139.
63. Sowerby, S.J., et al., *Scanning tunneling microscopy image contrast as a function of scan angle in hydrogen-bonded self-assembled monolayers*. Langmuir, 1998. **14**(18): p. 5195-5202.
64. Woodward, J.T. and J.A. Zasadzinski, *height amplifications of scanning-tunneling-microscopy images in air*. Langmuir, 1994. **10**(5): p. 1340-1344.
65. Xu, Q.M., et al., *Effect of chemically modified tips on STM imaging of 1-octadecanethiol molecule*. Journal of Physical Chemistry B, 2001. **105**(43): p. 10465-10467.
66. Ouseph, P.J. and M. Gossman, *Effects of self-modifying multiple tips on STM surface pictures*. Measurement Science & Technology, 1998. **9**(4): p. 701-704.
67. Giancarlo, L., et al., *Scanning tunneling microscopy of molecular adsorbates at the liquid-solid interface: Functional group variations in image contrast*. Langmuir, 1998. **14**(6): p. 1465-1471.
68. Sacks, W., D. Roditchev, and J. Klein, *Voltage-dependent STM image of a charge density wave*. Physical Review B, 1998. **57**: p. 13118-13131.
69. Lang, N.D., *theory of single-atom imaging in the scanning tunneling microscope*. Physical Review Letters, 1986. **56**(11): p. 1164-1167.
70. Yang, T., et al., *Self-assembly of long chain alkanes and their derivatives on graphite*. Journal of Chemical Physics, 2008. **128**(12): p. 124709.
71. Claypool, C.L., et al., *Source of image contrast in STM images of functionalized alkanes on graphite: A systematic functional group approach*. Journal of Physical Chemistry B, 1997. **101**(31): p. 5978-5995.
72. Ilan, B., et al., *Scanning Tunneling Microscopy Images of Alkane Derivatives on Graphite: Role of Electronic Effects*. Nano Letters, 2008. **8**(10): p. 3160-3165.
73. Liang, W., et al., *Electronic Origin of Scanning-Tunneling-Microscopy Images and Carbon Skeleton Orientations of Normal-Alkanes Adsorbed on Graphite*. Advanced Materials, 1993. **5**(11): p. 817-821.
74. Ortman, F., W.G. Schmidt, and F. Bechstedt, *Attracted by long-range electron correlation: Adenine on graphite*. Physical Review Letters, 2005. **95**(18): p. 186101.
75. Fisher, A.J. and P.E. Blochl, *Adsorption and scanning-tunneling-microscope imaging of benzene on graphite and MOS₂*. Physical Review Letters, 1993. **70**(21): p. 3263-3266.
76. Ludwig, C., et al., *video-STM, LEED and X-ray-diffraction investigations of PTCD A on graphite*. Zeitschrift Fur Physik B-Condensed Matter, 1992. **86**(3): p. 397-404.
77. Binnig, G., C.F. Quate, and C. Gerber, *Atomic Force Microscope*. Physical Review Letters, 1986. **56**(9): p. 930-933.
78. Chung, D.D.L., *Review graphite*. Journal of Materials Science, 2002. **37**(8): p. 1475-1489.
79. Di Ventra, M., *Introduction to nanoscale science and technology*. Nanostructure science and technology: Boston, Mass. [u.a.] : Kluwer Acad. Publ., c 2004. XIII, 611 S.
80. Dresselhaus, M.S. and J.G. Mavroides, *the Fermi surface of graphite*. Ibm Journal of Research and Development, 1964. **8**(3): p. 262-267.
81. Tomanek, D., et al., *Theory and observation of highly asymmetric atomic structure in scanning-tunneling-microscopy images of graphite*. Physical Review B: Condensed Matter and Materials Physics, 1987. **35**(14): p. 7790-3.
82. Jeffrey, G.A., *An Introduction to Hydrogen Bonding (Topics in Physical Chemistry)*. 13. März 1997 ed. Topics in physical chemistry. Vol. VII, 303 S. : graph. Darst. ; 25 cm: New York [u.a.] : Oxford Univ. Press, 1997. 303 Seiten.

83. Schmidt, W.G., et al., *Organic molecule adsorption on solid surfaces: Chemical bonding, mutual polarization and dispersion interaction*. Applied Physics A: Materials Science & Processing, 2006. **85**(4): p. 387-397.
84. Gowtham, S., et al., *Physisorption of nucleobases on graphene: Density-functional calculations*. Physical Review B, 2007. **76**.
85. Hunter, C.A., et al., *Aromatic interactions*. Journal of the Chemical Society-Perkin Transactions 2, 2001(5): p. 651-669.
86. Shibasaki, K., et al., *Magnitude of the CH/ π interaction in the gas phase: Experimental and theoretical determination of the accurate interaction energy in benzene-methane*. Journal of Physical Chemistry A, 2006. **110**(13): p. 4397-4404.
87. Israelachvili, J., *Intermolecular & Surface Forces*. 2nd Edition, reprinted ed. Vol. XXI, 450 S. : Ill., graph. Darst.: London [u.a.], Academic Press. 450 S.
88. Ertl, G., *thermodynamics of gas surface interactions*. Pure and Applied Chemistry, 1989. **61**(6): p. 1001-1007.
89. Bruch, L.W., R.D. Diehl, and J.A. Venables, *Progress in the measurement and modeling of physisorbed layers*. Reviews of Modern Physics, 2007. **79**(4): p. 1381-1454.
90. London, F., *The general theory of molecular forces*. Transactions of Faraday Society, 1936. **332**: p. 8.
91. Hentschke, R., B.L. Schurmann, and J.P. Rabe, *Molecular-dynamics simulations of ordered alkane chains physisorbed on graphite*. Journal of Chemical Physics, 1992. **96**(8): p. 6213-6221.
92. Hentschke, R. and R.G. Winkler, *Molecular-dynamics simulation study of the adsorption of chain alkanes from solution onto graphite*. Journal of Chemical Physics, 1993. **99**(7): p. 5528-5534.
93. Groszek, A.J., *Selective Adsorption at Graphite/Hydrocarbon Interfaces*. Proceedings of the Royal Society of London Series a-Mathematical and Physical Sciences, 1970. **314**(1519): p. 473-498.
94. Yin, S.X., et al., *Theoretical study of the effects of intermolecular interactions in self-assembled long-chain alkanes adsorbed on graphite surface*. Surface and Interface Analysis, 2001. **32**(1): p. 248-252.
95. Kolasinski, K.W., *Surface science*. Reprinted. ed: Chichester [u.a.] : Wiley, 2004. XX, 305 S.
96. Chen, S.H. and C.W. Frank, *Infrared and fluorescence spectroscopic studies of self-assembled n-alkanoic acid monolayers*. Langmuir, 1989. **5**(4): p. 978-987.
97. Langmuir, I., *The adsorption of gases on plane surfaces of glass, mica and platinum*, in *Journal of American Chemical Society*. 1918. p. 1361-1403.
98. Russ, J.C., *The Image Processing Handbook*. Auflage: 5 (30. Dezember 2006) ed. Vol. 817 S. : Ill., graph. Darst. ; 26 cm. 2007, Boca Raton, Fla. [u.a.]: CRC/Taylor & Francis. 832 Seiten.
99. Jorgensen, J.F., et al., *Calibration, Drift Elimination, and Molecular-Structure Analysis*. Journal of Vacuum Science & Technology B, 1994. **12**(3): p. 1698-1701.
100. Norgaard, K. and T. Bjornholm, *Supramolecular chemistry on water - towards self-assembling molecular electronic circuitry*. Chemical Communications, 2005(14): p. 1812-1823.
101. Beginn, U., *Thermotropic columnar mesophases from N-H center dot center dot center dot O, and N center dot center dot center dot H-O hydrogen bond supramolecular mesogenes*. Progress in Polymer Science, 2003. **28**(7): p. 1049-1105.
102. Lei, S., et al., *Bottom-up assembly of high density molecular nanowire cross junctions at a solid/liquid interface*. Chemical Communications, 2008(6): p. 703-705.

103. Akutagawa, T., et al., *Molecularly assembled nanostructures of a redox-active organogelator*. *Angewandte Chemie-International Edition*, 2005. **44**(44): p. 7283-7287.
104. Chandrasekhar, S. and G.S. Ranganath, *Discotic liquid crystals*. *Reports on Progress in Physics*, 1990. **53**(1): p. 57-84.
105. Hudson, S.D., et al., *Direct visualization of individual cylindrical and spherical supramolecular dendrimers*. *Science*, 1997. **278**(5337): p. 449-452.
106. Albrecht, K., et al., *Thin film morphologies of block copolymers complexed with wedge-shaped liquid crystalline amphiphilic molecules*. *Macromolecules*, 2008. **41**(5): p. 1728-1738.
107. Lehn, J.M., J. Malthete, and A.M. Levelut, *Tubular mesophases: liquid crystals consisting of macrocyclic molecules*. *Journal of the Chemical Society-Chemical Communications*, 1985(24): p. 1794-1796.
108. Zhu, X., et al., *Self-Organization of Polybases Neutralized with Mesogenic Wedge-Shaped Sulfonic Acid Molecules: An Approach toward Supramolecular Cylinders*. *Journal of the American Chemical Society*, 2006. **128**(51): p. 16928-16937.
109. Percec, V., et al., *Molecular Recognition Directed Self-assembly of Supramolecular Cylindrical Channel-like Architectures from -Octahydro- pentaoxabenzocyclopentadecen-2-ylmethyl 3,4,5-Tris(p-dodecyloxybenzyl-oxy)benzoate*. *Journal of the Chemical Society-Perkin Transactions 1*, 1993(13): p. 1411-1420.
110. Beginn, U., et al., *Self-organization of a liquid crystalline methacrylate-monofunctionalized crown-ether compound in low-shrinkage acrylate mixtures*. *Macromolecular Chemistry and Physics*, 1997. **198**(9): p. 2839-2852.
111. Gong, H.F., et al., *Self-assembly of amphiphilic hexapyridinium cations at the air/water interface and on HOPG surfaces*. *Chemphyschem*, 2007. **8**: p. 2354-2362.
112. Bleyl, I., et al., *One-dimensional hopping transport in a columnar discotic liquid-crystalline glass*. *Philosophical Magazine B-Physics of Condensed Matter Statistical Mechanics Electronic Optical and Magnetic Properties*, 1999. **79**(3): p. 463-475.
113. Boden, N., R.J. Bushby, and J. Clements, *Discotic Liquid Crystals as Quasi-One-Dimensional Electrical Conductors*. *Journal of Chemical Physics*, 1993. **98**(7): p. 5920-5931.
114. Boden, N., et al., *One-dimensional electronic conductivity in discotic liquid crystals*. *Chemical Physics Letters*, 1988. **152**(1): p. 94-99.
115. Boden, N., et al., *mechanism of charge-transport in discotic liquid-crystals*. *Physical Review B*, 1995. **52**(18): p. 13274-13280.
116. Pfister, G., *Hopping transport in a molecularly doped organic polymer*. *Physical Review B*, 1977. **16**(8): p. 3676-3687.
117. Pfister, G. and H. Scher, *Dispersive (non-Gaussian) transient transport in disordered solids*. *Advances in Physics*, 1978. **27**(5): p. 747-798.
118. Bassler, H., *Charge Transport in Disordered Organic Photoconductors a Monte Carlo Simulation Study*. *Physica Status Solidi B-Basic Research*, 1993. **175**(1): p. 15-56.
119. Bassler, H., et al., *Hopping transport in prototypical organic glasses*. *Physical Review B*, 1982. **26**(6): p. 3105-3113.
120. Nonappa, et al., *Unraveling the packing pattern leading to gelation using SS NMR and X-ray diffraction: direct observation of the evolution of self-assembled fibers*. *Soft Matter*, 2010. **6**(8): p. 1748-1757.
121. Kato, T., et al., *Liquid-crystalline physical gels*. *Chemical Society Reviews*, 2007. **36**: p. 1857-1867.
122. Yang, X.C., et al., *Novel carbazole-based organogels modulated by tert-butyl moieties*. *Chemical Communications*, 2008(4): p. 453-455.
123. Sangeetha, N.M. and U. Maitra, *Supramolecular gels: Functions and uses*. *Chemical Society Reviews*, 2005. **34**(10): p. 821-836.

124. Fuhrhop, J.H., D. Spiroski, and C. Böttcher, *Molecular monolayer rods and tubules made of alpha-(L-Lysine), Omega-(amino) bolaamphiphiles*. Journal of the American Chemical Society, 1993. **115**(4): p. 1600-1601.
125. Ghosh, A. and J. Dey, *pH-responsive and thermoreversible hydrogels of N-(2-hydroxyalkyl)-L-valine amphiphiles*. Langmuir, 2009. **25**(15): p. 8466-72.
126. Horcas, I., et al., *WSXM: a software for scanning probe microscopy and a tool for nanotechnology*. Review of Scientific Instruments, 2007. **78**(1): p. 013705.
127. Thomas, L.K., et al., *Monolayer Structure of Arachidic Acid on Graphite*. The Journal of Physical Chemistry C, 2010. **114**(44): p. 18919-18924.
128. Tour, J.M., *Molecular electronics : commercial insights, chemistry, devices, architecture and programming*. Vol. Umfang: XII, 370 S. : Ill., graph. Darst.: River Edge, NJ [u.a.] : World Scientific, 2003.
129. Aksay, I.A., et al., *Biomimetic pathways for assembling inorganic thin films*. Science, 1996. **273**(5277): p. 892-898.
130. Jacquemain, D., et al., *2-dimensional crystallography of amphiphilic molecules at the air-water interface*. Angewandte Chemie-International Edition in English, 1992. **31**(2): p. 130-152.
131. Perez-Garcia, L. and D.B. Amabilino, *Spontaneous resolution under supramolecular control*. Chemical Society Reviews, 2002. **31**(6): p. 342-356.
132. Hibino, M., A. Sumi, and I. Hatta, *Atomic images of saturated and unsaturated fatty-acids at liquid/graphite interface and difference of tunneling currents between them observed by scanning-tunneling-microscopy*. Japanese Journal of Applied Physics, 1995. **34**(2A): p. 610-614.
133. Rabe, J.P. and S. Buchholz, *Commensurability and mobility in two-dimensional molecular patterns on graphite*. Science (Washington, DC, United States), 1991. **253**(5018): p. 424-7.
134. Hibino, M., A. Sumi, and I. Hatta, *Molecular arrangements of fatty acids and cholesterol at liquid/graphite interface observed by scanning tunneling microscopy*. Japanese Journal of Applied Physics, Part 1: Regular Papers, Short Notes & Review Papers, 1995. **34**(6B): p. 3354-9.
135. Hibino, M., A. Sumi, and I. Hatta, *Molecular motion at domain boundaries in fatty acid monolayers on graphite observed by scanning tunneling microscopy*. Thin Solid Films, 1996. **273**(1-2): p. 272-278.
136. Hibino, M., et al., *Microscopic origin of the odd-even effect in monolayer of fatty acids formed on a graphite surface by scanning tunneling microscopy*. Journal of Physical Chemistry B, 1998. **102**(23): p. 4544-4547.
137. Tao, F. and S.L. Bernasek, *Chirality in supramolecular self-assembled monolayers of achiral molecules on graphite: Formation of enantiomorphous domains from arachidic anhydride*. Journal of Physical Chemistry B, 2005. **109**(13): p. 6233-6238.
138. Tao, F., J. Goswami, and S.L. Bernasek, *Self-assembly and odd-even effects of cis-unsaturated carboxylic acids on highly oriented pyrolytic graphite*. Journal of Physical Chemistry B, 2006. **110**(9): p. 4199-4206.
139. Fang, H.B., L.C. Giancarlo, and G.W. Flynn, *Packing of Br(CH₂)₁₀COOH and Br(CH₂)₁₁COOH on graphite: An odd-even length effect observed by scanning tunneling microscopy*. Journal of Physical Chemistry B, 1998. **102**(38): p. 7421-7424.
140. Kühnle, A., et al., *Chiral recognition in dimerization of adsorbed cysteine observed by scanning tunneling microscopy*. Nature, 2002. **415**(6874): p. 891-893.
141. Chen, J.H., C.L. Brooks, and H.A. Scheraga, *Revisiting the carboxylic acid dimers in aqueous solution: Interplay of hydrogen bonding, hydrophobic interactions, and entropy*. Journal of Physical Chemistry B, 2008. **112**(2): p. 242-249.

142. Findeneg, G.H., *Ordered Layers of Aliphatic Alcohols and Carboxylic-Acids at Pure Liquid-Graphite Interface*. Journal of the Chemical Society-Faraday Transactions I, 1973. **69**: p. 1069-1078.
143. Aquino, A.J.A., et al., *Solvent effects on hydrogen bonds - A theoretical study*. Journal of Physical Chemistry A, 2002. **106**(9): p. 1862-1871.
144. Bures, M. and J. Bezus, *Study of Hydrogen-Bonding in Carboxylic-Acids by the Mndo/M Method*. Collection of Czechoslovak Chemical Communications, 1994. **59**(6): p. 1251-1269.
145. Chocholousova, J., J. Vacek, and P. Hobza, *Acetic acid dimer in the gas phase, nonpolar solvent, microhydrated environment, and dilute and concentrated acetic acid: Ab initio quantum chemical and molecular dynamics simulations*. Journal of Physical Chemistry A, 2003. **107**(17): p. 3086-3092.
146. Lee, K.M., et al., *Focused-ion-beam-assisted selective control of graphene layers: acquisition of clean-cut ultra thin graphitic film*. Nanotechnology, 2010. **21**(20): p. 205303.
147. Tapasztó, L., et al., *Tailoring the atomic structure of graphene nanoribbons by scanning tunnelling microscope lithography*. Nature Nanotechnology, 2008. **3**(7): p. 397-401.
148. Campos, L.C., et al., *Anisotropic Etching and Nanoribbon Formation in Single-Layer Graphene*. Nano Letters, 2009. **9**(7): p. 2600-2604.
149. Giesbers, A.J.M., et al., *Nanolithography and manipulation of graphene using an atomic force microscope*. Solid State Communications, 2008. **147**(9-10): p. 366-369.
150. Arscott, P.G., et al., *scanning tunnelling microscopy of Z-DNA*. Nature, 1989. **339**(6224): p. 484-486.
151. Park, S.I. and C.F. Quate, *Tunneling Microscopy of Graphite in Air*. Applied Physics Letters, 1986. **48**(2): p. 112-114.
152. Soler, J.M., et al., *interatomic forces in scanning tunneling microscopy - giant corrugations of the graphite surface*. Physical Review Letters, 1986. **57**(4): p. 444-447.
153. Atamny, F., O. Spillecke, and R. Schlögl, *On the STM imaging contrast of graphite: towards a \"true\" atomic resolution*. Physical Chemistry Chemical Physics, 1999. **1**(17): p. 4113-4118.
154. Hembacher, S., et al., *Revealing the hidden atom in graphite by low-temperature atomic force microscopy*. Proceedings of the National Academy of Sciences of the United States of America, 2003. **100**(22): p. 12539-12542.
155. Ferro, Y. and A. Allouche, *Interpretation of STM images of graphite with an atomic vacancy via density-functional calculations of electronic structure*. Physical Review B, 2007. **75**(15).
156. Gwo, S. and C.K. Shih, *site-selective imaging in scanning-tunneling-microscopy of graphite - the nature of site asymmetry*. Physical Review B, 1993. **47**(19): p. 13059-13062.
157. Kuwabara, M., D.R. Clarke, and D.A. Smith, *anomalous superperiodicity in scanning tunneling microscope images of graphite*. Applied Physics Letters, 1990. **56**(24): p. 2396-2398.
158. Wang, Y., Y. Ye, and K. Wu, *Simultaneous observation of the triangular and honeycomb structures on highly oriented pyrolytic graphite at room temperature: An STM study*. Surface Science, 2006. **600**(3): p. 729-734.
159. Ruffieux, P., et al., *Hydrogen atoms cause long-range electronic effects on graphite*. Physical Review Letters, 2000. **84**(21): p. 4910-4913.
160. Iijima, S., *Helical Microtubules of Graphitic Carbon*. Nature, 1991. **354**(6348): p. 56-58.
161. Novoselov, K.S., et al., *Two-dimensional atomic crystals*. Proceedings of the National Academy of Sciences of the Proceedings of the National Academy of Science USA, 2005. **102**(30): p. 10451-10453.
162. Novoselov, K.S., et al., *Electric Field Effect in Atomically Thin Carbon Films*. Science (Washington, DC, United States), 2004. **306**(5696): p. 666-669.

163. Novoselov, K.S., et al., *Two-dimensional gas of massless Dirac fermions in graphene*. Nature (London, United Kingdom), 2005. **438**(7065): p. 197-200.
164. Geim, A.K. and K.S. Novoselov, *The rise of graphene*. Nature Materials, 2007. **6**(3): p. 183-191.
165. Geim, A.K., *Graphene: Status and Prospects*. Science, 2009. **324**(5934): p. 1530-1534.
166. Neto, A.H.C., et al., *The electronic properties of graphene*. Reviews of Modern Physics, 2009. **81**(1): p. 109-162.
167. Obeng, Y., et al., *Graphene and Emerging Materials for Post-CMOS Applications*. CS transactions ; Vol. 19 no. 5 : Fullerenes, nanotubes, and carbon nanostructures. Vol. IX, 407 S. : Ill., graph. Darst. 2009: Pennington, NJ : Electrochemical Soc., 2009. 407.
168. Rycerz, A., J. Tworzydło, and C.W.J. Beenakker, *Valley filter and valley valve in graphene*. Nature Physics, 2007. **3**(3): p. 172-175.
169. Müllen, K. and J.P. Rabe, *Nanographenes as active components of single-molecule electronics and how a scanning tunneling microscope puts them to work*. Accounts of Chemical Research, 2008. **41**(4): p. 511-520.
170. Kondo, S., M. Lutwyche, and Y. Wada, *nanofabrication of layered materials with the scanning tunneling microscope*. Applied Surface Science, 1994. **75**: p. 39-44.
171. Barnard, A.S., *Modelling the relative stability of carbon nanotubes exposed to environmental adsorbates and air*. Journal of Physics-Condensed Matter, 2009. **21**(14).
172. Heckl, W.M. and D.P.E. Smith, *Electropolymerization of glutaraldehyde observed by scanning tunneling microscopy and its implications for scanning tunneling microscopy imaging of organic material*. Journal of Vacuum Science & Technology B, 1991. **9**(2): p. 1159-1161.
173. Hiura, H.F., *Tailoring graphite layers by scanning tunneling microscopy*. Applied Surface Science, 2004. **222**(1-4): p. 374-381.
174. Hiura, H., *Generation of circular and hexagonal microholes in a graphite surface*. Journal of Materials Research, 2001. **16**(5): p. 1287-1292.
175. Xhie, J., et al., *giant and supergiant lattices on graphite*. Physical Review B, 1993. **47**(23): p. 15835-15841.
176. Sun, H.L., et al., *Scanning tunneling microscopy study of superlattice domain boundaries on graphite surface*. Surface Science, 2003. **542**(1-2): p. 94-100.
177. Pong, W.T. and C. Durkan, *A review and outlook for an anomaly of scanning tunnelling microscopy (STM): Superlattices on graphite*. Journal of Physics D-Applied Physics, 2005. **38**(21): p. R329-R355.
178. Choudhary, S.K. and A.K. Gupta, *Spatially varying super-lattice structures and linear fringes on graphite surface*. Journal of Physics-Condensed Matter, 2008. **20**(22): p. 225008.
179. Patrick, D.L. and T.P. Beebe, *On the origin of large-scale periodicities observed during scanning-tunneling-microscopy studies of highly ordered pyrolytic-graphite*. Surface Science, 1993. **297**(3): p. L119-L121.
180. Daulan, C., et al., *CDW in FECL₄-graphite-intercalation compounds studied by STM*. Molecular Crystals and Liquid Crystals Science and Technology Section a-Molecular Crystals and Liquid Crystals, 1994. **244**: p. 379-384.
181. Roy, H.V., et al., *Manipulation of graphitic sheets using a tunneling microscope*. Journal of Applied Physics, 1998. **83**(9): p. 4695-4699.
182. Beginn, U., S. Sheiko, and M. Moller, *Self-organization of 3,4,5-tris(octyloxy)benzamide in solution and embedding of the aggregates into methacrylate resins*. Macromolecular Chemistry and Physics, 2000. **201**(10): p. 1008-1015.

183. Li, L., et al., *Tearing, folding and deformation of a carbon-carbon sp²-bonded network*. Carbon, 2006. **44**: p. 1544-1547.
184. Simonis, P., et al., *STM study of a grain boundary in graphite*. Surface Science, 2002. **511**(1-3): p. 319-322.
185. Yatabe, T., et al., *Extended triphenylenes: synthesis, mesomorphic properties and molecularly resolved scanning tunneling microscopy images of hexakis(dialkoxyphenyl)triphenylenes and dodeca(alkoxy)tris(triphenylenylene)s*. Journal of Materials Chemistry, 2000. **10**(7): p. 1519-1525.
186. Thomas, L.K., et al., *Monolayer Structure of Arachidic Acid on Graphite*. Journal of Physical Chemistry C, 2010. **114**(44): p. 18919-18924.
187. Heckl, W.M. and G. Binnig, *Domain-walls on graphite mimic DNA*. Ultramicroscopy, 1992. **42**: p. 1073-1078.
188. Clemmer, C.R. and T.P. Beebe, *Graphite: a mimic for DNA and other biomolecules in scanning tunneling microscope studies*. Science, 1991. **251**(4994): p. 640-642.
189. Pandey, D., *Surface microscopy characterizations of large size graphene films grown by surface segregation on Ni and transferred to Si/SiO₂ substrate*. ECS transactions, 2009. **19**(5): p. 75-80.
190. Lu, X.K., et al., *Tailoring graphite with the goal of achieving single sheets*. Nanotechnology, 1999. **10**(3): p. 269-272.
191. Xu, K., P.G. Cao, and J.R. Heath, *Scanning Tunneling Microscopy Characterization of the Electrical Properties of Wrinkles in Exfoliated Graphene Monolayers*. Nano Letters, 2009. **9**(12): p. 4446-4451.
192. Hong, J.P., et al., *Organic single-nanofiber transistors from organogels*. Chemical Communications, 2009(3): p. 310-312.
193. Scanlon, S. and A. Aggeli, *Self-assembling peptide nanotubes*. Nano Today, 2008. **3**(3-4): p. 22-30.
194. Otsuki, J., et al., *Supramolecular fibers and microbelts from a phthalhydrazide derivative of crown ether with alkyl chains*. Chemistry Letters, 2006. **35**(11): p. 1256-1257.
195. Ward, J.M. and J.I. Schröder, *Roles of ion channels in initiation of signal transduction in higher plants*. Molecular and Cell Biology Updates; Signal transduction in plants, 1997: p. 1-22.
196. Amabilino, D.B. and J. Puigmarti-Luis, *Gels as a soft matter route to conducting nanostructured organic and composite materials*. Soft Matter, 2010. **6**(8): p. 1605-1612.
197. Simpson, C.D., et al., *From graphite molecules to columnar superstructures - an exercise in nanoscience*. Journal of Materials Chemistry, 2004. **14**: p. 494-504.
198. Beginn, U., G. Zipp, and M. Möller, *Synthesis and characterization of tris-methacrylated 3,4,5-tris[(alkoxy)benzyloxy]benzoate derivatives*. Chemistry-a European Journal, 2000. **6**(11): p. 2016-2023.
199. Li, J.L., et al., *Microengineering of Supramolecular Soft Materials by Design of the Crystalline Fiber Networks*. Crystal Growth & Design, 2010. **10**(6): p. 2699-2706.
200. Schmidt-Mende, L., et al., *Self-organized discotic liquid crystals for high-efficiency organic photovoltaics*. Science, 2001. **293**(5532): p. 1119-1122.
201. Bushby, R.J., *Dr Richard J. Bushby*. Journal of the Chemical Society-Perkin Transactions 1, 1999(1): p. V-VI.
202. Leclere, P., et al., *Organic semi-conducting architectures for supramolecular electronics*. European Polymer Journal, 2004. **40**(5): p. 885-892.
203. Petukhov, K., et al., *STM spectroscopy of magnetic molecules*. Coordination Chemistry Reviews, 2009. **253**(19-20): p. 2387-2398.
204. Carroll, D.L., et al., *Anomalous periodic structure of polypropylene chains observed with scanning tunneling microscopy*. Langmuir, 2000. **16**(8): p. 3574-3577.

205. Ma, D.D.D., et al., *Small-diameter silicon nanowire surfaces*. Science, 2003. **299**(5614): p. 1874-1877.
206. Rettig, C., M. Bodecker, and H. Hovel, *Carbon-nanotubes on graphite: Alignment of lattice structure*. Journal of Physics D: Applied Physics, 2003. **36**(7): p. 818-822.
207. Foster, J.S. and J.E. Frommer, *Imaging of Liquid-Crystals Using a Tunnelling Microscope*. Nature, 1988. **333**(6173): p. 542-545.
208. Nakajima, K., et al., *Direct observations of the structure of a main-chain thermotropic liquid-crystalline homopolyester by scanning tunneling microscopy*. Japanese Journal of Applied Physics Part 1-Regular Papers Short Notes & Review Papers, 1996. **35**(12A): p. 6166-6171.
209. Parks, D.C., et al., *Scanning Tunneling Microscopy of Coexisting 2D Crystalline and 1D Stacking-Disordered Phases at the Chiral-Liquid-Crystal-Graphite Interface*. Physical Review Letters, 1993. **70**(5): p. 607-610.
210. Xu, Q.M., et al., *STM studies on adsorbed liquid crystal on HOPG*. Science in China Series B-Chemistry, 1998. **41**(6): p. 640-645.
211. Valiyaveetil, S. and K. Mullen, *Multiphase self-assembly of 5-alkoxyisophthalic acid and its applications*. New Journal of Chemistry, 1998. **22**(2): p. 89-95.
212. Perronet, K. and F. Charra, *Influence of molecular-substrate interaction on the self-assembly of discotic liquid crystals*. Surface Science, 2004. **551**(3): p. 213-218.
213. Jung, H.T., et al., *Surface order in thin films of self-assembled columnar liquid crystals*. Macromolecules, 2002. **35**(9): p. 3717-3721.
214. Percec, V., et al., *Controlling polymer shape through the self-assembly of dendritic side-groups*. Nature, 1998. **391**(6663): p. 161-164.
215. Penfold, B.R. and J.C.B. White, *The crystal and molecular structure of benzamide*. Acta Crystallographica, 1959. **12**(2): p. 130-135.
216. Gawronski, H., et al., *Using a chemical concept for reactivity for the interpretation of STM images of physisorbed molecules*. Applied Surface Science, 2007. **253**: p. 9047-9053.
217. Thomas, L., et al., *Self-assembly of arachidic acid on highly oriented pyrolytic graphite*. 14.01.2010: p. submitted to PCCP.
218. Hermann, B.A., et al., *Self-organized monolayers: A route to conformational switching and read-out of functional supramolecular assemblies by scanning probe methods*. Advanced Functional Materials, 2006. **16**(2): p. 221-235.
219. Mohamadi, F., et al., *Macromodel—an integrated software system for modeling organic and bioorganic molecules using molecular mechanics*. Journal of Computational Chemistry, 1990. **11**(4): p. 440-467.
220. Zhang, Y.J., et al., *Interfacial-dependent morphologies in the self-organization system of chiral molecules observed by atomic force microscopy*. Journal of Physical Chemistry B, 2002. **106**(8): p. 1960-1967.
221. Ozin, G.A.A., André C., *Nanochemistry : a chemical approach to nanomaterials*. 2006: Cambridge, UK : RSC Publ.(Royal Society of Chemistry), XL, 628 S.. : zahlr. Ill., graph. Darst.. ; 24cm.
222. Rai, R., et al., *Programmed hyperhelical supramolecular assembly of nickel phthalocyanine bearing enantiopure 1-(p-tolyl)ethylaminocarbonyl groups*. Langmuir, 2005. **21**(9): p. 3957-3962.
223. Raisanen, M.T., et al., *Alkyl chain length defines 2D architecture of salophen complexes on liquid-graphite interface*. European Journal of Inorganic Chemistry, 2007(25): p. 4028-4034.
224. Keg, P., et al., *Direct observation of alkyl chain interdigitation in conjugated polyquarterthiophene self-organized on graphite surfaces*. Macromolecular Rapid Communications, 2008. **29**(14): p. 1197-1202.

225. Yokoyama, T., et al., *Selective assembly on a surface of supramolecular aggregates with controlled size and shape*. Nature, 2001. **413**: p. 619-621.
226. Henn, G., et al., *Influence of order in thin smectic polymer films on the structure at the surface*. Physica B, 1996. **221**(1-4): p. 174-184.
227. Piot, L., et al., *Hierarchical Self-Assembly of Edge-On Nanocolumnar Superstructures of Large Disc-Like Molecules*. Advanced Materials, 2008. **20**(20): p. 3854.
228. Zhou, Y.S., et al., *Observation of co-existence of 'face-on' and 'edge-on' stacking styles in a porphyrin monolayer*. Chemical Physics Letters, 2005. **403**(1-3): p. 140-145.
229. Langmuir, I., *The constitution and fundamental properties of solids and liquids* . Journal of American Chemical Society, 1917. **39**: p. 1848.
230. Woo, Y., *Large-grained and highly-ordered graphene synthesized by radio frequency plasma-enhanced chemical vapor Deposition*. ECS Transactions, 2009. 19: p.111.

Acknowledgements

It is my great pleasure to thank my doctoral advisor Prof. Michael Reichling of the Nanoscience Center, for his constant guidance and incessant support. I would like to thank my co-advisor Prof. Uwe Beginn from the Chemistry department for allowing me to work on the molecules synthesized in his group and for many fruitful discussions. I am grateful to Prof. Angelika Kühnle (now at Mainz) who had been a co-advisor, for her continuous support and many insightful discussions.

I would like to thank all the present and former members of research groups of Prof. Michael Reichling and Prof. Angelika Kühnle, for their kind cooperation in various ways and for many group excursions and barbecues. Sincere thanks to Prof. Dr. Philipp Maass and Dr. Johann P. Klare, for agreeing to act as referees for my defense. Many thanks to Ms. Frauke Riemann for her help with official formalities. Thanks are also due to members of the research group of Prof. Uwe Beginn, for their kind cooperation whenever I had to visit the chemistry department.

The financial support through the graduate program '*synthesis and characterization of surfaces and interfaces assembled from clusters and molecules*' from the State Government of Lower Saxony (Germany) is gratefully acknowledged. I would also like to thank the chair of the program Prof. Manfred Neumann, Prof. Jürgen Schnack and the coordinator of the program Dr. Heidrun Elfering.

Erklärung

Erklärung über die Eigenständigkeit der erbrachten wissenschaftlichen Leistung

Ich erkläre hiermit, dass ich die vorliegende Arbeit ohne unzulässige Hilfe Dritter und ohne Benutzung anderer als der angegebenen Hilfsmittel angefertigt habe. Die aus anderen Quellen direkt oder indirekt übernommenen Daten und Konzepte sind unter Angaben der Quelle gekennzeichnet.

Osnabrück, 11th April 2011

(Loji K Thomas)

